Investigating the roles of ice dynamics and climate on polar near-surface processes

Annika Noel Horlings

A dissertation
submitted in partial fulfillment of the
requirements for the degree of

Doctor of Philosophy

University of Washington

2023

Reading Committee:
Knut Christianson, Chair
Michelle Koutnik
Nicholas Holschuh

Program Authorized to Offer Degree:
Department of Earth and Space Sciences

University of Washington

Abstract

Investigating the roles of ice dynamics and climate on polar near-surface processes

Annika Noel Horlings

Chair of the Supervisory Committee:
Professor Knut Christianson
Department of Earth and Space Sciences

Understanding processes in the snow and firn are important for studies of ice dynamics, ice-sheet mass balance, glacial hydrology, and ice-core interpretation. In this dissertation, I use a combination of modeling, geophysical methods, and analyses of regional climate model output and reanalysis to study the evolution of firn compaction, firn hydrology, and snow accumulation on alpine glaciers and ice sheets in response to changes in ice dynamics and climate.

The first study is devoted to investigating one process that is neglected in firn-air content estimates derived from firn-compaction models: enhanced layer thinning due to horizontal divergence. In this study, I implemented a new scheme into the Community Firn Model, a modular model framework that can simulate numerous physical processes in firn. Modeling results showed that horizontal divergence can reduce local firn-air content by up to 41% and may contribute to 16% of surface lowering for some dynamic fast-flowing regions in West Antarctica. I find that omitting transient horizontal divergence in estimates of firn-air content leads to an overestimation of ice loss via satellite-altimetry methods in regions of dynamic ice flow.

The second study characterizes the extent of four firn aquifers in the Helheim, Ikertivaq, and Køge Bugt glacier basins of southeast Greenland using airborne ice-penetrating radar data from 1993 to 2018. All four firn aquifers first appear and/or show decadal-scale inland expansion during this time period. A relative energy budget calculation using regional climate model output shows that these aquifer expansions are driven by decreasing cold content in the firn since the late 1990s and a recently increasing number of high-melt years. High-melt years are projected to increase on the Greenland Ice Sheet and may contribute to the continued inland expansion of firn aquifers, impacting the ice sheet's surface mass balance and hydrological controls on ice dynamics.

The third study is devoted to examining the recent snow-accumulation rates at Hercules Dome, Antarctica, a prospective ice-core site. Only one observation of the snow-accumulation rate exists and accuracy of climate models remains limited there, meriting further study. I use ground-based very high frequency ground-penetrating radar collected during the 2019-2020 and 2022-2023 austral summers to construct the first spatially resolved snow-accumulation dataset over Hercules Dome. The 420-year, 326-year, and 225-year time-averaged accumulation rates are similar and range from 0.10 to 0.15 m a^{-1} ice equivalent across the divide, with greater accumulation to the grid north (EPSG:3031) toward the Filchner-Ronne sector. Analyses of regional climate-model output and climate reanalysis show that the snow-accumulation pattern is likely a result of an orographic effect on the regional scale and wind redistribution on the local scale. The snow-accumulation variability across the divide will be important to consider for future ice-core science at Hercules Dome.

This dissertation improves our understanding of a variety of polar near-surface processes that are integral in assessing ice-sheet mass balance in the past, present, and the future.

TABLE OF CONTENTS

LIST OF FIGURES

Figure Number Page

LIST OF TABLES

Table Number Page

ACKNOWLEDGMENTS

I feel very fortunate to have been a part of a community of incredible people during my time in graduate school. This work would not have been possible otherwise.

Firstly, I am deeply grateful to my advisor, Knut Christianson, for his continued guidance and support of my research endeavors during the last seven years. Additionally, I am thankful for his exceptional support of my pursuit of activities outside of research ranging from teaching, volunteering, and DEI-related graduate-student initiatives. I must also thank Knut for letting me discover the research that most resonated with me and for his patience and support during the inevitable times when I couldn't quite find my way.

I will forever be thankful to Ed Waddington, who is a significant reason why I was able to first attend the University of Washington and whose kind mentorship was especially invaluable during the first few years of my PhD.

I would also like to express deep appreciation to Nick Holschuh, for being an important mentor to me from the beginning of my graduate studies. His ability to take a big-picture approach to science and life I can only regard highly and consider wise.

A multitude of thanks to Michelle Koutnik for serving on my committee, for initiating our "Glaciology Women's" group, and for her keen advice and insightful discussions on science, graduate school, careers, and life.

I would also like to thank Twit Conway, who I spent the 2022-2023 Antarctic field season with. His scientific expertise, perseverance, soft-spoken leadership, and humor I can only hold in high esteem. In addition, his whole-hearted trust in my own leadership during the field season was quite invaluable to building my own confidence as a scientist and leader.

I am also grateful for the people who made fieldwork fun by their stories, spontaneous ski adventures, and camaraderie: the 2019-2020 Hercules Dome field team; the 2022-2023 Allan Hills field team; the USGS glaciologists; and the JIRP community.

I am deeply grateful for my community of lifelong friends within and outside of the University of Washington, who have offered countless unforgettable experiences, invaluable camraderie, and many much-needed excursions to the mountains to help me create a balanced and joy-filled life during graduate school: Jessica Badgeley, Devon Geary, Will Greene, Michelle Hansmann, Ayla Heinz-Fry, Gemma O'Connor, and Addien Wray.

My family has been incredibly supportive of me through this process and I am thankful to them. I am especially grateful to my sister, Ilyse Horlings, who has been a tremendous support, and my mother, Laurie Chinn, who first inspired my love of nature and the earth.

DEDICATION

To the many strong women who have influenced me on my journey.

Chapter 1

INTRODUCTION

My journey as an earth scientist informally began during the early years of my youth. On many family hikes into the Cascade Range of the U.S. Pacific Northwest, I often would sit for hours in awe of the glaciers and surrounding geology. “The mountains are calling and I must go and I will work on while I can, studying incessantly.” I often recalled and was inspired by these famous words by naturalist and conservationalist John Muir. They evoked the lure of the mountains and natural world, and reminded me of our responsibility to understand our interconnectedness with nature. Aptly, many years later, I ended up formally studying glaciers at the University of Washington, with a specific focus on the part of them that is perhaps most obviously interconnected with the changing climate: the snow and firn.

In this dissertation, I investigate polar near-surface processes that are important in assessing ice-sheet mass change through an integration of modeling, geophysical observations, and analysis of regional climate model output and reanalysis. In this first chapter, I will provide motivation for and an outline of the dissertation. I start by providing an introduction of near-surface processes of glaciers and ice sheets; the ice and climate dynamics that can affect these; and why we care to study these processes. I then outline the structure of the dissertation and topics that are discussed in Chapters 2-4, which are written as stand-alone manuscripts. Finally, I provide some concluding remarks derived from this dissertation. It is my hope that this body of work provides a little more insight into the interconnectedness of the snow and firn and climate, which are evermore important to understand amidst our currently evolving and greatly complex world.

1.1 Motivation

The world's ice sheets and alpine glaciers are integral parts of Earth's hydrologic cycle and are inextricably connected to the oceans and atmosphere. Due to anthropogenic climate change, the ice sheets and many of the world's alpine glaciers are declining primarily due to surface melting and dynamic thinning (Fox-Kemper et al., 2021). The most wide-reaching affect of these changes is global mean sea-level rise, with impacts on the world's coastal populations and infrastructure, coastal populations' ability to respond to extreme events, global economy, and ecological systems. Glacier decline also has a multitude of other significant regional impacts on water resources, hydroelectric power generation, agriculture, forestry, tourism and downstream ecosystems. It is therefore imperative that we understand the changes that are occurring in the cryosphere.

Currently, the world's ice sheets and glaciers are overall losing mass, but sometimes the processes contributing to mass loss and the regional differences in these processes are complex. The Greenland Ice Sheet is losing mass at an overall accelerating rate and while there is strong interannual variability, the principal processes governing the mass loss are surface melt (which is increasing in dominance) and dynamic thinning (which is decreasing in dominance) (Fox-Kemper et al., 2021). Although recent studies suggest that net mass loss of the Antarctic Ice Sheet has not increased since 2016 because of some regional mass gains in Dronning Maud Land, mass loss in West Antarctica has otherwise dominated the entire ice sheet's mass balance since the 1970s (Fox-Kemper et al., 2021). The decadal-scale mass loss of the Antarctic Ice Sheet has generally increased since the 1990s, and is primarily driven by dynamic thinning of outlet glaciers (Fox-Kemper et al., 2021). Finally, during 2010-2019, the world's alpine glaciers lost more mass than any other decade since the beginning of the observational record (Fox-Kemper et al., 2021).

The future is unclear; however, with continued observations, analysis, and modeling, the outlook of the world's ice sheets and glaciers can be increasingly understood. For the Greenland Ice Sheet, it is virtually certain that continued mass loss through 2100 will occur under all greenhouse-gas emissions scenarios (Fox-Kemper et al., 2021). There is also high confidence that mass loss from the Greenland Ice Sheet will become increasingly dominated by surface melt since the response of outlet glaciers from warm ocean waters will diminish as the outlet glaciers retreat to higher ground (Fox-Kemper et al., 2021). For the Antarctic Ice Sheet, it is likely that mass loss will continue through 2100 as well under all greenhouse-gas emissions scenarios, where dynamic losses driven by ocean warming and ice-shelf disintegration will exceed some regionally increasing snowfall rates (Fox-Kemper et al., 2021). However, the upper end of projections is not well constrained, due to different assumptions about the future sensitivity of ice-shelf basal melting to ocean warming and recently proposed concepts of mass loss such as marine ice-cliff instability triggered by ice-shelf disintegration (Fox-Kemper et al., 2021). For the world's alpine glaciers, mass loss will continue, with as much as a 18-36% decline from 2015 to 2100 (Fox-Kemper et al., 2021).

1.2 Mass Balance of Glaciers and Ice Sheets

The connection between climate change and the ice sheets can be understood via the concept of mass balance, where the net balance of inputs and outputs determines the ice sheet's net change in mass. The total mass of a glacier changes only through processes that transfer mass between the glacier and its environment, including the atmosphere, ocean, land, and groundwater (Cuffey and Paterson, 2010). In addition, redistribution of mass within the glacier can occur via compaction, ice flow, or hydrological processes. Another important component of the glacier-climate connection is the relation between mass balance and glacier dynamics. For example, thickening and steepening of the glacier due to increased accumulation will increase flow. In addition, the elevation of the glacier surface may rise or fall through time depending on the ice flow, which may change the surface climate (Cuffey and Paterson, 2010).

The mass balance can generally be subdivided based on where the mass exchange occurs within the glacier, along the vertical axis (Cuffey and Paterson, 2010):

$$\frac{dM}{dt} = \int_A [\dot{b}_s + \dot{b}_e + \dot{b}_b] dA - \dot{B}_c, \tag{1.1}$$

where $\frac{dM}{dt}$ is the derivative of the mass with respect to time, $\dot{b}_s$ is the surface mass balance, $\dot{b}_e$ is the englacial mass balance, $\dot{b}_b$ is the basal mass balance, A is the plan-view area, M is the mass of the ice sheet, and $\dot{B}_c$ is the mass lost through calving per unit time. This equation can be integrated over a given time interval to give the glacier's mass balance ΔM.

To consider ice flow into and out of a zone or sector of a glacier or ice sheet within the mass-balance equation, Equation 1.1 is then equivalent to the Equation 1.2, where S is the elevation of the surface, Q_{in} is the flux entering the zone, and Q_{out} is the flux exiting the zone, which is equivalent to $\dot{B}_c$ if the region includes the glacier's margin:

$$\int_A [\dot{b}_s + \dot{b}_e + \dot{b}_b] dS + Q_{in} - Q_{out}. \tag{1.2}$$

The mass at any coordinate within the glacial system is the product of the vertically averaged density ($\bar{\rho}$) and the ice thickness. Therefore, the density of firn (the material transitioning from freshly fallen snow to glacial ice) must be considered when estimating the balance (see Chapter 2).

The surface mass balance $\dot{b}_s$ dominates the net mass balance for many glaciers and ice sheets, though calving and dynamic thinning are critical for some that are marine-terminating. The surface mass balance $\dot{b}_s$ can be expressed as:

$$\dot{b}_s = \dot{a}_s + \dot{a}_a - \dot{m}_s + \dot{a}_r - \dot{s} + \dot{a}_w \tag{1.3}$$

where $\dot{a}_s$ is the snowfall rate, $\dot{a}_a$ is deposition via avalanches, $\dot{m}_s$ is surface melt, $\dot{a}_r$ is refreezing of water, $\dot{s}$ is sublimation, and $\dot{a}_w$ is deposition of snow via the wind (Cuffey and Paterson, 2010). The surface mass balance rate $\dot{b}_s$ is integral in mass balance studies as well as ice-core interpretation and context (see Chapter 4).

The englacial mass balance in temperate alpine glaciers and some regions of the ice sheets is largely determined by the redistribution of liquid water from the surface of the glacier to the interior of the glacier (Cuffey and Paterson, 2010). Internal accumulation can occur through refreezing of surface melwater that has percolated into the firn, in crevasses or moulins, or fractures at the base of the glacier; in addition to liquid water persisting as firn aquifers (see Chapter 3). Internal ablation can also be due to melting caused by flowing water, deforming ice, or solar radiation near the surface. All of these englacial processes remain a large source of uncertainty in mass-balance measurements and models due to the heterogeneity of most of these hydrological processes.

1.3 Organization of This Thesis

Chapter 2 investigates one process that is neglected in firn-air content estimates derived from firn-compaction models: enhanced layer thinning due to horizontal divergence. This chapter was published in the *Journal of Glaciology* as **Effect of horizontal divergence on estimates of firn-air content** (Horlings et al., 2021). I incorporated a layer-thinning scheme into the Community Firn Model where, at every time step, the firn layers first densify according to a firn-compaction model and then thin further due to an imposed horizontal diverence rate without additional density changes. I assess the effects of spatial and temporal variability of changing horizontal divergence on firn-air content on the rapidly changing Thwaites and Pine Island Glaciers, Antarctica.

Chapter 3 characterizes the evolution of firn aquifers in southeast Greenland using airborne ice-penetrating radar data and uses climate reanalysis to link this to changing climate conditions. This chapter was published in *Journal of Geophysical Research: Earth Surface* as **Expansion of firn aquifers in southhast Greenland** (Horlings et al., 2022). I used airborne ice-penetrating radar data from the Center for Remote Sensing of Ice Sheets (CReSIS) to document the extent of four firn aquifers in the Helheim, Ikertivaq, and Køge Bugt glacier basins with more than six repeat radar flight lines from 1993 to 2018. Then, through an idealized energy-balance calculation utilizing reanalysis data from the Modèle Atmosphéique Régionale (MAR) regional climate model, I link the observed firn-aquifer changes to changes in the cold content of the firn and comment on the future of firn aquifers.

Chapter 4 presents recent snow-accumulation rates derived from a ground-based shallow radar survey at Hercules Dome, Antarctica, a prospective ice-core site, where only one observation of the snow-accumulation rate exists and accuracy of climate models remains limited there. I use ground-based very high frequency ground-penetrating radar data collected during the 2019-2020 and 2022-2023 austral summers to construct the first spatially resolved snow-accumulation dataset over Hercules Dome and characterize the accumulation-rate pattern in terms of spatial distribution, temporal variations, and related accumulation processes. This chapter will soon be submitted to *Geophysical Research Letters*.

Chapter 5 contains a summary and general conclusions from this work.

Chapter 2

EFFECT OF HORIZONTAL DIVERGENCE ON ESTIMATES OF FIRN-AIR CONTENT

Chapter 2, in full, is a reprint of “Effect of horizontal divergence on estimates of firn-air content" authored by A.N. Horlings, K. Christianson, N. Holschuh, C.M. Stevens, and E.D. Waddington, as it appears in *Journal of Glaciology* 2020. The supplement for this paper can be found in Appendix A. The dissertation author was the primariy investigator and author of this paper.

2.1 Abstract

Ice-sheet mass-balance estimates derived from repeat satellite-altimetry observations require accurate calculation of spatiotemporal variability in firn-air content (FAC). However, firn-compaction models remain a large source of uncertainty within mass-balance estimates. In this study, we investigate one process that is neglected in FAC estimates derived from firn-compaction models: enhanced layer thinning due to horizontal divergence. We incorporate a layer-thinning scheme into the Community Firn Model. At every time step, firn layers first densify according to a firn-compaction model and then thin further due to an imposed horizontal divergence rate without additional density changes. We find that horizontal divergence on Thwaites (THW) and Pine Island Glaciers can reduce local FAC by up to 41% and 18%, respectively. We also assess the impact of temporal variability of horizontal divergence on FAC. We find a 15% decrease in FAC between 2007 and 2016 due to horizontal divergence at a location that is characteristic of lower THW. This decrease accounts for 16% of the observed surface lowering, whereas climate variability alone causes negligible changes in FAC at this location. Omitting transient horizontal divergence in estimates of FAC leads

to an overestimation of ice loss via satellite-altimetry methods in regions of dynamic ice flow.

2.2 Introduction

Many outlet glaciers of the polar ice sheets have accelerated and thinned markedly in the last 25 years (Joughin et al., 2012; Mouginot et al., 2014; Smith et al., 2020). While horizontal divergence is low in the ice-sheet interior, outlet glaciers often have substantial spatially and temporally evolving horizontal divergence rates. Investigating many fundamental glaciological problems depends on accurately estimating changes in firn-air content (FAC; the volume of air in a firn column of unit cross-sectional area), including the determination of mass loss from thinning due to marine ice-sheet instability, an important component of the land-ice contribution to sea-level rise (Depoorter et al., 2013; Shepherd et al., 2012, 2019; Smith et al., 2020). Despite its importance, most firn-compaction models lack a method to account for horizontal divergence in estimates of FAC in regions of fast flow. Here, we formulate a simple model scheme - an accessible and easily applicable alternative to a material-specific constitutive relation (Gagliardini and Meyssonnier, 1997; Lüthi and Funk, 2000) - that accounts for horizontal divergence within the firn to show the importance of the effect of horizontal divergence on FAC estimates in regions of the ice sheet with high and rapidly changing horizontal divergence rates.

2.2.1 Background

Firn compaction occurs through a variety of microphysical mechanisms, such as grain-boundary sliding, sintering, and bubble compression. These mechanisms respond to overburden stresses and temperature gradients (Burr et al., 2019; Maeno and Ebinuma, 1983), to processes related to melting and refreezing (Reeh et al., 2005), and to ice-flow stresses (Alley and Bentley, 1988). These processes vary spatially and temporally, resulting in variable firn-density profiles. Model estimates of firn-column thickness, FAC, and the rate at which these evolve often have substantial uncertainty, partly because not all physical processes are included or accurately captured within the current generation of firn-compaction models.

For example, thinning in the firn column due to horizontal divergence in the underlying ice is often assumed to be negligible even in regions with high horizontal divergence rates (Kuipers Munneke et al., 2015), despite observational evidence of its impact on firn-density structure (Christianson et al., 2014; Morris et al., 2017; Riverman et al., 2019).

2.2.2 Firn-air content

Estimating mass change of the ice sheets with repeat satellite-altimetry observations requires model-derived estimates of changes in FAC (Depoorter et al., 2013; Shepherd et al., 2012, 2019). FAC, also known as depth-integrated porosity or DIP, is defined as the porosity integrated over depth z, from the surface to the depth z_i where ice density ρ_i is attained:

$$FAC = \int_0^{z_i} \left(\frac{\rho_i - \rho(z)}{\rho_i} \right) dz. \tag{2.1}$$

The change in mass of the ice sheet Δm can be calculated in terms of the observed surface height change Δh, the change in FAC ΔFAC, ice density ρ_i, and area A:

$$\Delta m = \left(\Delta h - \Delta FAC\right) \rho_i A. \tag{2.2}$$

Improving firn-compaction models, and specifically producing more accurate estimates of FAC, is an essential step in reducing uncertainty in altimetry-derived mass-balance products. Currently, model estimates of FAC can have large uncertainty partly because firn-compaction models have been calibrated only to, and therefore are appropriate only for, a limited range of climate and ice-dynamic settings (Lundin et al., 2017). Most firn-compaction models also are compatible with the suggestions by Robin (1958) under steady-state conditions. Robin (1958) suggested that, in steady-state conditions, the change in density with depth $\frac{d\rho(z)}{dz}$ (and thus FAC) is proportional to the change in overburden stress. This requires that no horizontal divergence occurs within the firn column (Morris et al., 2017):

$$\frac{d\rho(z)}{dz} = \rho(z) \left(\rho_i - \rho(z)\right). \tag{2.3}$$

However, observations collected over the last 60 years indicate that large deviatoric stresses in the underlying solid ice affect the firn by increasing the rate of firn-density change with depth (Alley and Bentley, 1988; Christianson et al., 2014; Crary and Charles, 1961; Gow, 1968; Kirchner et al., 1979; Morris et al., 2017; Riverman et al., 2019; Vallelonga et al., 2014; Zumberge, 1960).

2.2.3 Previous observations and modeling work

Active-source seismic and radar surveys across the Northeast Greenland Ice Stream show that the firn column is 30 m thinner in the shear margins than outside the margins (Christianson et al., 2014; Riverman et al., 2019; Vallelonga et al., 2014). Riverman et al. (2019) inferred that this spatial variability of firn density is due to both horizontal divergence and strain softening (i.e., an increased firn-compaction rate due to the acceleration of time-dependent microphysical processes from increased ice-flow stresses). Morris et al. (2017) accounted for horizontal divergence in the firn along the iSTAR traverse on Pine Island Glacier by using a layer-thinning scheme similar to the one we propose here (see Section 2 of the Supplementary Material). Morris et al. (2017) showed that the negative ratio of the vertical densification rate to the density-corrected volumetric strain rate is not equal to the mean-annual accumulation rate in some cases; they attributed this to a non-negligible horizontal divergence, and illustrated that the steady-state suggestion by Robin (1958) does not hold in those cases.

Some modeling studies have attempted to incorporate the impact of horizontal ice-flow stresses on firn within a constitutive formulation using a generalized form of Glen's Law (Gagliardini and Meyssonnier, 1997; Lüthi and Funk, 2000). This approach has not been widely adopted by the firn community, because it is difficult to integrate into commonly used firn-compaction models. To our knowledge, no current firn-compaction model used for inferring ice-sheet mass balance from repeat-altimetry observations (e.g., Li and Zwally, 2015; Ligtenberg et al., 2011, etc.) accounts for horizontal divergence.

In this study, we incorporate a layer-thinning scheme to account for horizontal divergence in the Community Firn Model (CFM) (Stevens et al., 2020), and systematically investigate the effects of horizontal divergence on FAC. We first describe the specifics of our implementation of the layer-thinning scheme in the CFM. Then, we test the scheme through a series of idealized conceptual runs for climate conditions representative of West Antarctica. We subsequently apply the layer-thinning scheme to a firn column along two flowlines on Thwaites Glacier and Pine Island Glacier, Antarctica, where dynamic ice-sheet thinning due to accelerating ice flow from marine ice-sheet instability is occurring (Joughin et al., 2014; Rignot et al., 2014). We then quantify how much of recent observed thinning results from FAC changes due to horizontal divergence for lower Thwaites Glacier. Finally, we map where horizontal divergence should be considered in FAC estimates across the entire Antarctic Ice Sheet

2.3 Methods

2.3.1 Horizontal divergence in the Community Firn Model

The Community Firn Model (CFM) is an open-source, modular model framework that is designed to simulate evolution of firn properties, including density, compaction rate, and temperature (Stevens et al., 2020). It utilizes a suite of thirteen published snow- and firn-compaction models. The CFM uses a one-dimensional Lagrangian framework to track the properties of firn parcels as they advect from the surface into the underlying ice sheet. Users stipulate the surface-boundary conditions, including accumulation rate, surface temperature, surface-snow density, and other parameters necessary for the chosen firn- or snow-compaction model.

To simulate layer-thickness changes within the CFM due to horizontal divergence, we adopt a kinematic two-part layer-thinning scheme for firn compaction (Figure 2.1). During each time step, the firn first densifies via the equations of the user-specified firn-compaction model:

$$\lambda_{part1} = \lambda_{old}(1 + \dot{\epsilon}_{zz}\Delta t). \tag{2.4}$$

where λ_{old} is the firn-parcel thickness at the previous time step, λ_{part1} is the firn-parcel thickness after densification from the firn-compaction model, λ_{part2} is the firn-parcel thickness after thinning from horizontal divergence, and Δt is the time step. $\dot{\epsilon}_{zz}$ is the vertical strain rate due to densification of the firn, provided by the chosen model physics, and commonly implemented in models as:

$$\dot{\epsilon}_{zz} = \frac{1}{\rho(z)} \frac{d\rho(z)}{dt}. \tag{2.5}$$

Equation 2.4 (part one) is identical to the procedure in a conventional firn-compaction model that neglects horizontal divergence.

When the firn parcels thin due to horizontal divergence (Equation 2.6; part two), during the same time step as densification due to Equation 2.4, the firn is horizontally stretched using a prescribed horizontal divergence rate $\dot{\epsilon}_h$:

$$\lambda_{part2} = \lambda_{part1}(1 - \dot{\epsilon}_h \Delta t). \tag{2.6}$$

Individual firn parcels stretch horizontally as a result of thinning due to horizontal divergence. Density and FAC calculations of the individual firn parcels in the CFM are produced per unit cross-sectional area of the firn parcels. Equation 2.6 does not consider density changes of individual firn parcels. This is because the scheme is solely kinematic, and it is assumed that the material properties of a given parcel of firn do not change with horizontal stretching. However, Equation 2.6 reduces the depth at which any density appears in the firn column.

2.3.2 Choice of firn-compaction models

In this study, we run the CFM using the firn-compaction equations from the Herron and Langway (1980) model (HL) and the Ligtenberg et al. (2011) model (LIG). Multiple firn-compaction models have been developed in the last 40 years. We use HL because it is still seen as a benchmark firn-compaction model, and most models of polar firn compaction are based on its general framework and assumptions (Li and Zwally, 2011; Ligtenberg et al., 2011; Morris and Wingham, 2014). HL used Antarctic and Greenlandic firn depth-density profiles to derive empirical equations describing the firn-compaction rate in stage one and stage two of the firn column. Stage one is where density $\rho < 550$ kg m^{-3}, and represents the shallowest portion of the firn column. Stage two occurs deeper and extends to bubble close-off, where densities range from 550 kg $\mathrm{m}^{-3} < \rho <$ 830 kg m^{-3}. Robin (1958) assumed that the change in firn-pore volume is proportional to the change in the overburden pressure, a steady-state assumption. This assumption allows HL to parametrize the overburden pressure using mean annual snow accumulation. In addition, the HL densification rate includes an Arrhenius-type temperature dependence, which represents densification via temperature-dependent microphysical mechanisms, such as grain growth (Gow, 1969).

We also use LIG because it is the firn-compaction model included in subsurface processes of the regional climate model RACMO (Van Wessem et al., 2018), one of the most common reanalysis products used in Antarctic mass-balance calculations. In addition, LIG has been used to estimate FAC changes in multiple ice-sheet mass-balance studies (Gardner et al., 2013; McMillan et al., 2016; Shepherd et al., 2012, 2019). LIG used forty-eight depth-density profiles from Antarctica to tune the firn-compaction model by Arthern et al. (2010) for general applicability in Antarctica. Arthern et al. (2010) measured vertical strain rates in the firn at four sites in Antarctica and used those data to derive a semi-empirical compaction model based on rate equations of Nabarro-Herring creep and grain growth (Coble, 1970; Gow, 1969), with a form similar to that of HL.

2.3.3 Model Inputs

Total horizontal divergence rates from ice velocities

We use the Mouginot et al. (2019a) Antarctic ice-velocity map to compute mean horizontal divergence rates from 1996 to 2018 at a spatial resolution of 450 m. We also use the Mouginot et al. (2017) ice-velocity time series to compute the annual horizontal divergence rates from 2007 to 2016 in the Amundsen Sea Embayment with a spatial resolution of 1 km. To compute the total horizontal divergence rate from the ice velocities, we implement the logarithmic strain-rate formulation from Alley et al. (2018) to produce continent-wide horizontal divergence rates. Designating u and v as the x and y components of the velocity field, respectively, in a polar stereographic coordinate system (EPSG: 3031), the two-dimensional strain-rate tensor is:

$$\dot{\epsilon} = \begin{bmatrix} \frac{\partial u}{\partial x} & \frac{1}{2}\left(\frac{\partial v}{\partial x} + \frac{\partial u}{\partial y}\right) \\ \frac{1}{2}\left(\frac{\partial v}{\partial x} + \frac{\partial u}{\partial y}\right) & \frac{\partial v}{\partial y} \end{bmatrix}. \tag{2.7}$$

If the strain-rate tensor is rotated with the local ice-flow direction, the total horizontal divergence rate, $\dot{\epsilon}_h$, can be computed as the trace of $\dot{\epsilon}$, or the sum of the longitudinal and transverse strain rates, respectively:

$$\dot{\epsilon}_h = \frac{\partial u}{\partial x} + \frac{\partial v}{\partial y}. \tag{2.8}$$

If the strain-rate tensor is not with the local ice-flow direction, the longitudinal and transverse strain rates can be reoriented to calculate the horizontal divergence rate $\dot{\epsilon}_h$ (see Alley et al., 2018). Errors can arise when generating the strain-rate tensor from a satellite-derived velocity field in areas of high strain when a nominal strain formulation is used (Alley et al., 2018). Therefore, we apply the logarithmic formulation from Alley et al. (2018), which compares the change in length with the previous length, and not the original length, to account for the history of strain that is experienced by that region of the ice sheet.

We specify the accumulation rate, surface temperature, and surface-snow density as the boundary conditions of the CFM. We force the CFM with a modified MERRA-2 climate reanalysis product (Smith et al., 2020, Brooke Medley, personal communication, 3 March 2020) at 5-day temporal resolution and 12.5 km spatial resolution. All accumulation rates we use in the model runs are in ice-equivalent units. Additionally, for all runs, we prescribe a constant surface-snow density of 400 kg m^{-3}. Fausto et al. (2018) discuss uncertainty arising from surface-snow density for firn-density calculations. While variable surface-snow density affects FAC estimates, we suspect it does not affect the relative change in FAC estimates from different horizontal divergence rates enough to alter our conclusions.

Table 2.1: Steps in horizontal divergence rates used in the layer-thinning scheme. These encompass the range of horizontal divergence rates commonly observed on the ice sheets. The model was forced with an accumulation rate of 0.30 m ice eq. yr^{-1}, surface temperature of -20°C, and surface-snow density of 400 kg m^{-3}. Percent decrease values are shown using LIG; values from HL are shown in parentheses.

Run	Step in horizontal divergence (yr^{-1})	% decrease in FAC
1	0 to 1×10^{-4}	0.4 (0.5)
2	0 to 1×10^{-3}	4.0 (6.1)
3	0 to 2.5×10^{-3}	9.6 (12.8)
4	0 to 5×10^{-3}	17.9 (22.3)
5	0 to 7.5×10^{-3}	25.0 (30.0)
6	0 to 1×10^{-2}	31.1 (36.3)

2.4 Results

2.4.1 Idealized Runs

To provide quantitative insight into the impact of horizontal divergence on FAC, we conduct idealized simulations using the HL and LIG models with constant climate forcing under six horizontal-divergence-rate scenarios that span the range of horizontal divergence rates observed on the ice sheets (Experiment 1; Table 2.1 and Figure 2.2). We choose surface-boundary conditions representative of central West Antarctica: a constant accumulation rate of 0.30 m yr^{-1}, and a constant temperature of -20° C (Fudge et al., 2016; Kaspari et al., 2004; Medley et al., 2013; Steig et al., 2005).

We spin the model up for 600 years to steady state under this constant climate with no horizontal divergence rate. Then, we run the model for 600 additional years, starting at time $t = 0$ years, using the same constant climate. We apply a step-change in horizontal divergence rate to the steady-state firn column at $t = 100$ years and track how the simulated

FAC evolves for the next 500 years. We run this routine using HL and LIG for six horizontal-divergence-rate scenarios (Table 2.1 and Figure 2.2).

Figure 2.2 shows the evolution of FAC through time predicted by LIG, including the evolution of the depth-density profile and bubble close-off (BCO) depth (i.e., density horizon of 830 kg m^{-3}). After an initial adjustment period, the simulated firn column reaches a new steady state approximately 500 years following the onset of the horizontal divergence rate for all runs. In this new steady state, the firn parcels have thinned, and the FAC has correspondingly decreased (Figure 2.3 and Table 2.1).

Adding a horizontal divergence rate of 10^{-3} yr^{-1} with the LIG (HL) model results in a FAC that is 4% (6%) less than for a model with no horizontal divergence (Experiment 1; Table 2.1 and Figure 2.3). Imposing a horizontal divergence rate of 10^{-2} yr^{-1} reduces the FAC by 31% (36%) compared to the no-horizontal-divergence scenario. HL estimates larger decreases in FAC than LIG for all idealized runs, and the difference between the models is larger for higher horizontal divergence rates (Figure 2.3).

2.4.2 Spatial Variability: Flowline Runs

To determine the impact of horizontal divergence on FAC in realistic climate and ice-flow conditions, we apply the layer-thinning scheme to two flowlines on Thwaites (THW - Experiment 2) and Pine Island (PIG - Experiment 3) Glaciers, West Antarctica (Figure 2.4). We choose these flowlines because ice-surface speeds have been monotonically increasing in this area during the satellite record (since 1992; Mouginot et al., 2014; Wingham et al., 1998), and the region is thinning rapidly (Schröder et al., 2019). This makes mass-balance estimates from the region sensitive to the treatment of horizontal divergence in firn-compaction models. The surface temperature and accumulation rate increase non-linearly along both flowlines, as they approach the lower-elevation coast. Along the THW flowline, the surface temperature increases from -27 °C to -18 °C, and the accumulation rate increases from 0.5 m i.e. yr^{-1} to 0.9 m i.e. yr^{-1}. Along the PIG flowline, the surface temperature increases from -26 °C to -17 °C, and the accumulation rate increases from 0.4 m yr^{-1} to 0.9 m yr^{-1}. The ice speed along each flowline increases as the ice enters streaming flow, from speeds less than 10 m yr^{-1} to speeds greater than 1000 m yr^{-1}, with corresponding increases in along-flow horizontal divergence rates (from 0 to $> 10^{-3}$ yr^{-1}).

The starting points of the flowlines were chosen so that the flowlines would extend through the main trunks of the glaciers. We again spin up the CFM for 600 years with the mean 1980 to 2019 climate (accumulation rate and temperature) for the head of the flowline, and no horizontal divergence rate. We run the model twice for each flowline, with and without an imposed horizontal divergence rate. The firn column advects through the flowline based on the temporally static, but spatially variable 1996 to 2018 mean ice velocities from Mouginot et al. (2019a). We map the temporally evolving firn column to its position along-flow, and plot the associated FAC for each position along the flowline in Figure 2.5 and Figure 2.6.

Figure 2.5 shows model results with and without including horizontal divergence using LIG for the THW flowline. Horizontal divergence along the THW flowline results in a mean 3.7 % (4.0%) difference for the entire flowline between the no-divergence and divergence runs using LIG (HL). However, the effect of horizontal divergence on modeled FAC increases towards the terminus of the glacier and influences FAC most within the last 150 to 200 km. At the end of the flowline, horizontal divergence causes the FAC to be up to 9.6 m (9.2 m) less than with a method that does not account for horizontal divergence (41% (40%) difference). For the PIG flowline (Figure 2.6), horizontal divergence results in an average 0.68% (0.81%) percent difference over the entire flowline. Like THW, horizontal divergence has the greatest impact on FAC estimates for the last 150 to 200 km of the flowline, where the FAC is 4.4 m (4.8 m) less while using a model with horizontal divergence compared to a conventional firn-compaction model (18% (19%) difference).

Experiments 2 and 3 indicate that horizontal divergence becomes most important to consider in estimating the FAC in the most coastal 150 to 200 km of THW and PIG. Horizontal divergence rates increase at approximately 150 to 200 km before the end of the THW and PIG flowlines, and the firn column begins to thin there (Experiments 2 and 3; Figures 2.5 and 2.6). The thickness of the entire firn layer along the flowline can be seen in Figures 2.5B and 2.6B, where the black line shows the 830 kg m^{-3} density horizon (BCO depth). The firn thins non-uniformly along the flowline as a result of the variability of the horizontal divergence rates, and thinning or thickening induced by the spatially variable accumulation rate and temperature. Note that higher accumulation rates increase the FAC, whereas higher temperatures decrease the FAC. Thus, higher accumulation rates will offset the effect of horizontal divergence on the FAC, whereas higher temperatures will reinforce the net thinning effect. Results from using HL for both flowlines on THW and PIG show qualitatively similar results and therefore are shown in Section 5 of the Supplementary Material.

2.4.3 Temporal Variability: Static Location on Lower Thwaites Glacier

To investigate the effect of temporal variability of horizontal divergence on FAC estimates during the satellite record, we next consider the time evolution of FAC (ΔFAC) from 2007 to 2016 for a fixed location on lower THW (Experiment 4; black star in Figure 2.4). We choose this location because the time series of ice speed is annually continuous, and mean thinning rates here are characteristic of a large portion of lower THW and of PIG. For spin up of the CFM, we use a constant horizontal divergence rate of 0.015 yr^{-1}, based on observations from the beginning of the time series. We spin up the CFM for 600 years using a climate forcing randomly generated from the normal distribution of the 1980 to 2007 mean climate.

We perform four model runs, all of which use the 2007 to 2016 temperature and accumulation-rate fields from MERRA-2, with annual time steps (Smith et al., 2020, Medley, personal communication, 3 March 2020). The accumulation rate, temperature, and divergence-rate boundary conditions are shown in Figure 2.7. Descriptions of each run are as follows:

(1) A baseline conventional firn-compaction-model run, which entails running the CFM with the evolving temperature and surface-accumulation rate but no horizontal divergence rate.

(2) A run with climate from (1), and a constant horizontal divergence rate of 0.015 yr^{-1} through the entire spin up and model run.

(3) A run with climate from (1); constant horizontal divergence rate of 0.015 yr^{-1} through

Table 2.2: Summary of results from temporally varying the horizontal divergence rate for the location on Thwaites Glacier from 2007 to 2016. Results using the LIG firn-compaction model in the layer-thinning scheme are shown, with results using the HL firn-compaction model in parentheses.

Run	ΔFAC (m)	% decrease in FAC	% of observed thinning
1	0.20 (0.17)	0.77 (0.66)	-1.18 (-1.04)
2	0.08 (0.12)	0.42 (0.68)	-0.46 (-0.73)
3	-2.66 (-2.71)	-15.30 (-15.55)	16.12 (16.50)
4	-1.83 (-1.91)	-11.66 (-12.08)	11.12 (11.57)

the spin up until 2007; then the horizontal divergence rate evolves based on the 2007 to 2016 ice-velocity time series.

(4) Run with climate from (1); constant horizontal divergence rate of 0.015 yr^{-1} through the spin up until 1997; linear ramp up to a horizontal divergence rate of 0.04 yr^{-1} at 2007; then the horizontal divergence rate evolves based on the 2007 to 2016 ice-velocity time series.

We choose these runs to demonstrate (a) the impact of horizontal divergence on FAC estimates through time, and (b) the effects of initializing the runs using firn columns with different initial conditions, which will result in different FACs due to the initial-state dependence of the firn-compaction rate (Figure 2.7). The lower panel in Figure 2.7 shows the model-predicted FAC for the four runs. Horizontal divergence applied over longer histories has higher influence on the FAC. Run 1 (no imposed horizontal divergence rate) consistently predicts a FAC that is 7 to 8 m greater than the other runs. Runs 3 and 4 address the influence of temporal variability of horizontal divergence on FAC estimates, which is important for assessing ice-sheet mass balance from repeat satellite-altimetry observations. These runs indicate a marked decrease in FAC associated with greater horizontal divergence rates.

Temporally increasing horizontal divergence rates reduce the FAC substantially (Table 2.2 and Figure 2.7). In Run 1, the FAC slightly increases by 0.20 m (0.17 m), or 0.77% (0.66%), almost a negligible change, from 2007 to 2016. In Run 2, the FAC also slightly increases by

0.08 m (0.12 m) or 0.42% (0.68%). In contrast, in Run 3, the FAC is reduced by 2.66 m (2.71 m), or 15.30% (15.55%). In Run 4, the FAC is reduced by 1.83 m (1.91 m), or 11.66% (12.08%). Even the short-term application of greater and time-variable horizontal divergence rates initialized in 2007 (Runs 3 and 4) produces a substantial difference in predicted FAC compared to the constant horizontal-divergence case (Run 2). FAC in 2016 is estimated to be 3.04 m (3.14 m) less in Run 3 than in Run 2 (18.75% (19.29%) difference) and is 3.86 m (4.00 m) less in Run 4 than in Run 2 (24.38% (25.21%) difference). FAC estimated in Run 3 and Run 4 begin to differ when the Run-4 horizontal divergence rate ramps up in 1997, ultimately resulting in a slightly lower FAC in 2016 (0.81 m (0.86 m); 5.70% (6.0%) difference) because the FAC in 1997 is already less in Run 4 than Run 3.

2.5 Discussion

In the following sections, we address the central questions motivating this study:

1) What is the importance of horizontal divergence in controlling FAC?

2) How do estimates of the time-evolution of FAC (ΔFAC) estimates change by including horizontal divergence in the calculations?

3) Where does horizontal divergence matter for estimating FAC on the Antarctic Ice Sheet?

Through investigating these questions, we find that, firstly, neglecting horizontal divergence where divergence rates exceed 10^{-4} yr^{-1} will lead to an overestimate in FAC. This is because a firn column in regions with horizontal divergence is stretched horizontally and is thinner, and thus has less air content per unit volume than a firn column in regions without horizontal divergence. Secondly, accounting for horizontal divergence in FAC estimates results in a smaller calculated mass loss for regions of increasing horizontal divergence through time. This is because, for a given change in surface elevation Δh, the time-evolution of FAC (ΔFAC) is greater for regions with increasing horizontal divergence through time, which implies that the interpreted Δm is less than estimates that neglect horizontal divergence (Equation 2.2). Lastly, we find that horizontal divergence should be included in FAC estimates in regions entering and within the outlet glaciers and ice shelves of the Antarctic Ice Sheet. Horizontal divergence should be accounted for in estimates of the time-evolution of FAC in these regions, as speeds and thinning rates are currently increasing (Joughin et al., 2012; Mouginot et al., 2014; Smith et al., 2020).

2.5.1 How do FAC estimates needed for altimetry studies change by including time-evolving horizontal divergence?

Results from our transient runs suggest that including horizontal divergence makes a substantial difference in the calculated ΔFAC. Decadal-scale climate variability (run 1) from 2007 to 2016 results in 0.20 m (0.17 m), a 0.77% (0.66%) increase. By comparison, ΔFAC for Run 2 is 0.08 m (0.12 m), a 0.42% (0.68%) increase. The only difference between Runs 1 and 2 is that Run 2 includes a constant horizontal divergence rate, which (1) makes the total FAC of Run 2 lower than that of Run 1; and (2) means that FAC changes for these two runs are solely a result of the variable climate. Runs 1 and 2 contrast Runs 3 and 4, which include the time-variable horizontal divergence and show substantial decreases in FAC through time (Table 2.2). These changes in FAC for Runs 3 and 4 constitute 16% and 11% of the observed thinning (27 m; Schröder et al., 2019), respectively, for this location on lower THW from 2007 to 2016. Surface lowering on a glacier is due to both mass loss and firn thinning or thickening; for a given observed elevation change Δh, if there is more firn thinning and thus higher ΔFAC, then there is less mass loss Δm.

2.5.2 Where do horizontal divergence rates matter for estimates of firn-air content on the Antarctic Ice Sheet?

To identify where horizontal divergence is important to consider in estimates of FAC, we first determine where the horizontal divergence-rate magnitude is comparable to the vertical strain-rate magnitude. We consider horizontal divergence negligible when the ratio of the magnitude of horizontal divergence rate to vertical strain rate is less than 0.1.

Figure 2.8 shows the Antarctic-wide ratio R of the depth-averaged vertical strain rate $\bar{\dot{\epsilon}}_{zz}$, within the firn column as calculated by the analytic model from Herron and Langway (1980), and the total horizontal divergence rate $\dot{\epsilon}_h$, as calculated from velocity data from Rignot and others (2017) following Alley et al. (2018):

$$R = \frac{\dot{\epsilon}_h}{\dot{\epsilon}_{zz}}. \tag{2.9}$$

Not unexpectedly, $R \geq 0.1$ occurs dominantly (1) in regions where ice enters the outlet glaciers along the margins of the Antarctic Ice Sheet, such as Pine Island Glacier, Thwaites Glacier, and other glaciers in the Amundsen Sea sector, and (2) in regions entering the ice shelves. Regions in the interior of the ice sheet have relatively low values of R. Based on this analysis, horizontal divergence can be neglected in broad interior regions of the ice sheet. Some high horizontal divergence rates on ice shelves are associated with ongoing rifting, and may not reflect changes in horizontal divergence rates that are of interest in this study.

2.5.3 Future work

We show, with a simple kinematic layer-thinning scheme in the CFM, that horizontal divergence must be accounted for in estimates of firn-air content in regions of dynamic ice flow. However, the effects of several additional processes not included in our model require further study: (1) the role of compressive strain in firn-thickness change, (2) densification during horizontal stretching, and (3) the role of brittle failure in reducing the effect of ductile thinning. To include compressive strain rates in our treatment of layer thinning, either better theoretical treatment of effects of compressional ice-flow stresses on firn compaction or intentional model calibration including high ice-flow-stress sites is needed. Most of the horizontal divergence rates in Experiment 2 and 3 are not compressive because these glaciers are not confined outlet glaciers and do not experience significant lateral compression associated with downstream narrowing of glacier extent. For these reasons, we chose to set any compressional strain rates in our runs to zero. We suspect that compressional stresses would not offset reduction in the FAC due to horizontal divergence, but would have an additive effect to increase firn density and lower FAC, because some microphysical mechanisms (e.g., power-law creep) are dependent on the square of the effective stress (Alley and Bentley, 1988; Maeno and Ebinuma, 1983). A dynamic treatment of horizontal extensional stresses in the firn would also contribute to densification during thinning and result in a further decrease in firn-air content for similar reasons. Previous studies refer to this effect as strain softening, and identify this process as having a greater impact on the firn-density profile than horizontal divergence in some locations (Riverman et al., 2019). Additionally, theoretical and observational evidence suggests that a decrease in the porosity will occur with an increase in the stress state due to increased damage and strain around bubbles (Alley and Fitzpatrick, 1999; Chawla and Deng, 2005). Finally, we ignore the effects of brittle failure in near-surface crevassing, which must accommodate some of the horizontal divergence in especially high strain-rate areas (Duddu and Waisman, 2012). Including a constitutive relation for density changes in response to horizontal stresses is an obvious next development. However, a dynamic treatment of horizontal stresses should be created along with a dynamic treatment of the vertical forces and vertical compression in firn. Additional experimental and field data is necessary for formulating such a model, and therefore is clearly beyond the scope of this paper.

Future work should therefore 1) collect more field measurements in regions of high horizontal ice-flow stresses; 2) intentionally calibrate models to high ice-flow-stress sites in an empirical framework; and/or 3) perform lab work investigating how density, viscosity, and microstructures change under horizontal ice-flow stresses. Firn-compaction models have been developed using depth-density profiles that are assumed to have negligible thinning due to horizontal ice-flow stresses. This is true for many of those profiles, but the model development processes have not necessarily checked the validity of this assumption for each core; nor have data from high-stress regions been sought out. As a result, firn-compaction models assume there is no dependence on ice-flow stresses due to their functional form. In regions that may indeed have ice-flow stresses, calibrating the models using data from firn density there could lead to error in the calibrated coefficient estimates. However, calibrating additional coefficients in existing models using firn data from identified high ice-flow-stress regions could accommodate some of the impacts of horizontal ice-flow stresses on FAC. Also, new geophysical techniques for measuring time series of firn thickness and density, such as GNSS interferometric reflectometry (Gutmann et al., 2012; Larson et al., 2009) and autonomous phase sensitive radio echo sounding (Corr et al., 2002; Jenkins et al., 2006; Nicholls et al., 2015) are promising low-cost methods for gathering additional firn depth-density data in regions of dynamic ice flow. Work is ongoing to formulate a dynamic, time-dependent expression encompassing the effects of horizontal ice-flow stresses on firn-compaction processes, and new measurements (e.g., micro-CT scans) may provide the necessary data on firn-grain evolution to construct a model based on microstructure evolution. Micro-CT technology is starting to be applied to measure firn properties (Adolph and Albert, 2014; Gregory et al., 2014; Keegan et al., 2019). Further work to characterize the relative roles of ductile and brittle behavior of the firn will also allow for better characterization of firn in high-stress environments.

2.6 Conclusions

Estimates of spatially and temporally variable firn-air content (FAC) are needed in calculations of ice-sheet mass balance derived from repeat-altimetry observations. Here, we introduced a method that accounts for firn-layer thinning from horizontal divergence into the Community Firn Model (Stevens et al., 2020). This scheme consists of 1) densification via an existing firn-compaction model, and 2) thinning of the firn via horizontal stretching due to horizontal divergence.

We assessed the spatial and temporal variability of changes in FAC due to horizontal divergence separately. Horizontal divergence becomes most impactful on FAC estimates in the last 100 to 150 km of the flowlines on Thwaites and Pine Island Glaciers, where horizontal divergence rates can reach 10^{-2} yr^{-1} and higher. At the end of the Thwaites flowline, horizontal divergence causes the FAC to be 41% less than FAC estimates from a conventional firn-compaction model with no horizontal divergence. At the end of the PIG flowline, horizontal divergence leads to a 18% less FAC compared to results from a conventional firn-compaction model. For a representative location on lower Thwaites Glacier, a 15% decrease in FAC occurs from 2007 to 2016 due to horizontal divergence, which corresponds to 16% of the observed surface-elevation change. This contrasts output from a conventional firn-compaction model with no horizontal divergence, which estimates a 0.77% increase in FAC, due to climate variability alone. Horizontal divergence is most important to include in FAC estimates in outlet glaciers in the Amundsen Sea Embayment, and in regions entering and within the ice shelves of Antarctica.

We find that horizontal divergence is important for both (1) estimates of the steady-state FAC and (2) estimates of FAC variability in time. Neglecting horizontal divergence in FAC estimates where horizontal divergence rates exceed 10^{-4} yr^{-1} will lead to an overestimate in the steady-state and time-evolving FAC. Improved FAC estimates will produce better estimates of mass-change from repeat surface-elevation observations, as well as more accurate estimates of basal-melt rates that depend on a hydrostatic assumption. Including horizontal divergence in FAC estimates will become more important as regions of the Antarctic Ice Sheet, such as the Amundsen Sea Embayment, continue to experience substantial increases in ice speed (Mouginot et al., 2014). Neglecting horizontal divergence within FAC estimates used in altimetry-derived mass-change calculations in these areas will lead to an overestimate in mass loss. Our work highlights the importance of accounting for horizontal divergence in estimates of FAC, and is a first step towards improving firn products that may consider adding the effects of strain thinning to produce better FAC outputs.

2.7 Code and data availability

The CFM code is publicly available at https://github.com/UWGlaciology/CommunityFirnModel. Documentation for the CFM is online at https://communityfirnmodel.readthedocs.io/TS5. Model output and scripts used to make the figures will be available on the University of Washington ResearchWorks Archive.

2.8 Author contribution

ANH, KC, EDW, and CMS designed the study. ANH implemented the layer-thinning procedure, ran the model experiments, and led writing of the paper. CMS aided implementation of the layer-thinning scheme in the CFM and performed some model runs. NH and KC contributed to analysis of ice-velocity data. All authors contributed to paper writing and editing.

2.9 Acknowledgements

We thank Brooke Medley for her modified MERRA-2 climate reanalysis data. We also express gratitude to Tyler J. Fudge and Michelle Koutnik for their comments on earlier versions of the manuscript. This work was supported by NASA grant NNX16AM01G and NSF grant 0968391.

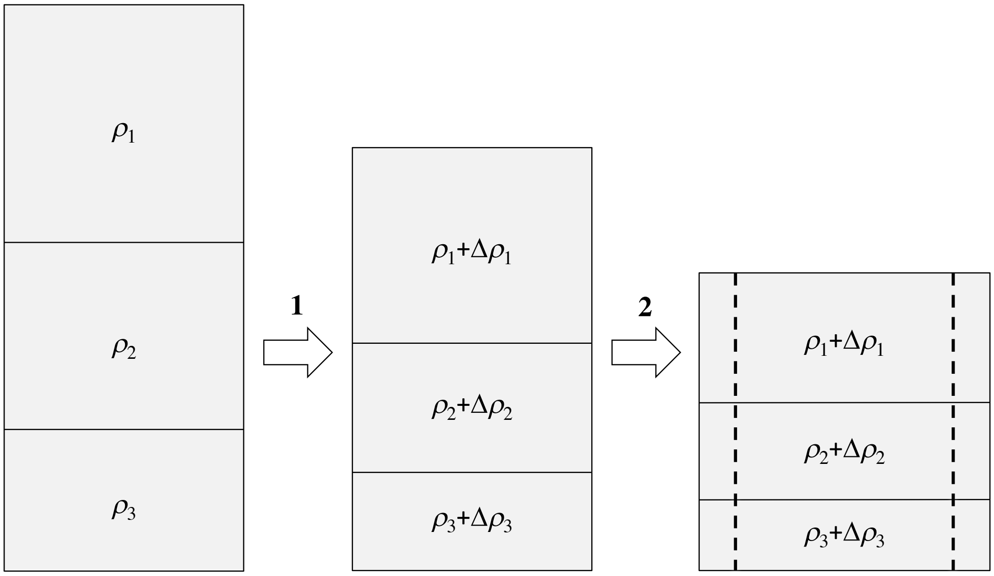

Figure 2.1: Our layer-thinning scheme that accounts for horizontal divergence in the CFM. At each time step, the firn first compresses vertically and densifies (Equation 2.4) following the equations of the user-specified firn-compaction model (part one). Then the firn stretches horizontally without further density change, as determined by the prescribed horizontal divergence rate $\dot{\epsilon}_h$ in Equation 2.6 (part two).

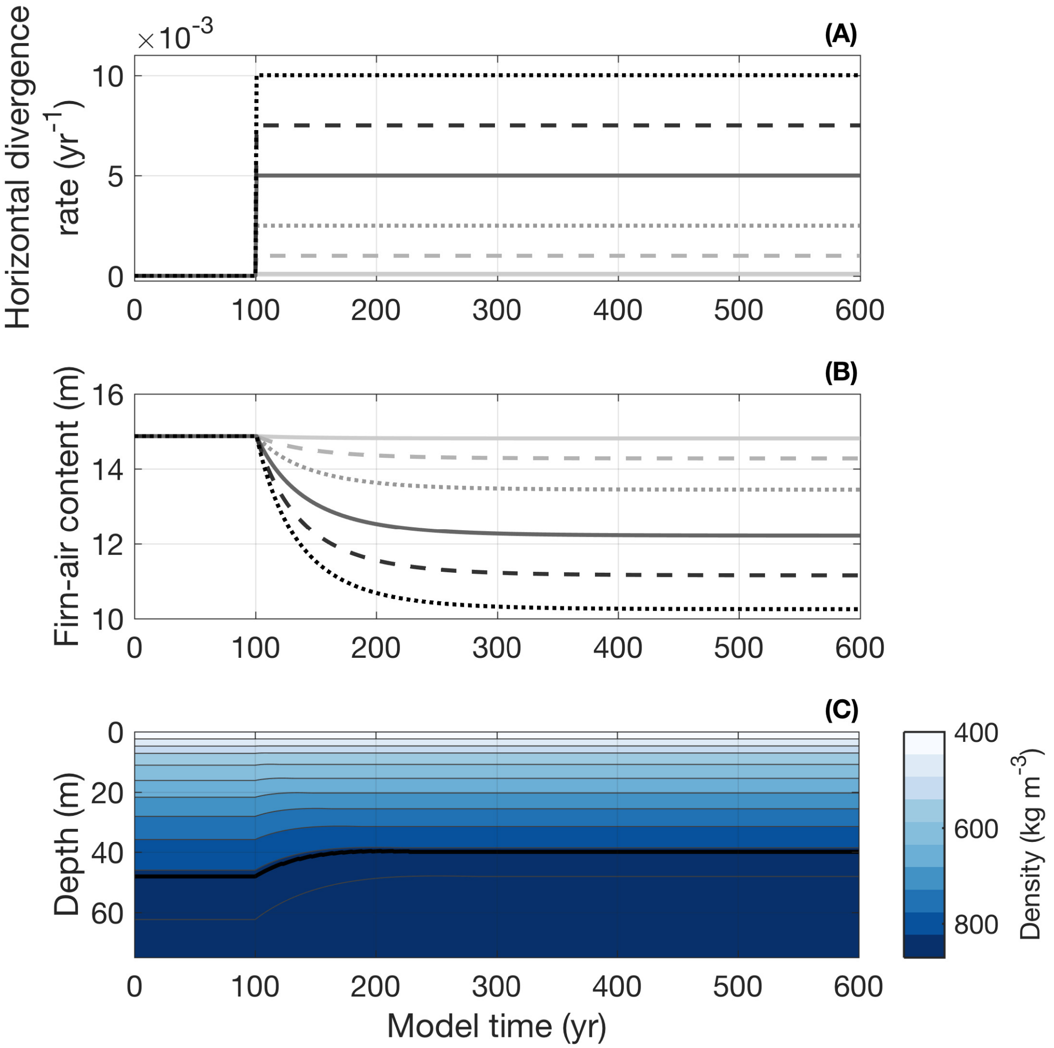

Figure 2.2: Model response of FAC (B) to a step change in the horizontal divergence rate (A) from 0 to 1×10^{-4} yr^{-1} (solid light gray line), to 0 to 1×10^{-2} yr^{-1} (dotted black line), using the LIG firn-compaction model. The model was forced with an accumulation rate of 0.30 m ice eq. yr^{-1}, surface temperature of -20°C, and surface-snow density of 400 kg m^{-3}. Evolution of the depth-density profile for a step-change in horizontal divergence rate of 5×10^{-3} is shown in (C) as an example. Black line indicates the BCO depth. Contour interval is 50 kg m^{-3}.

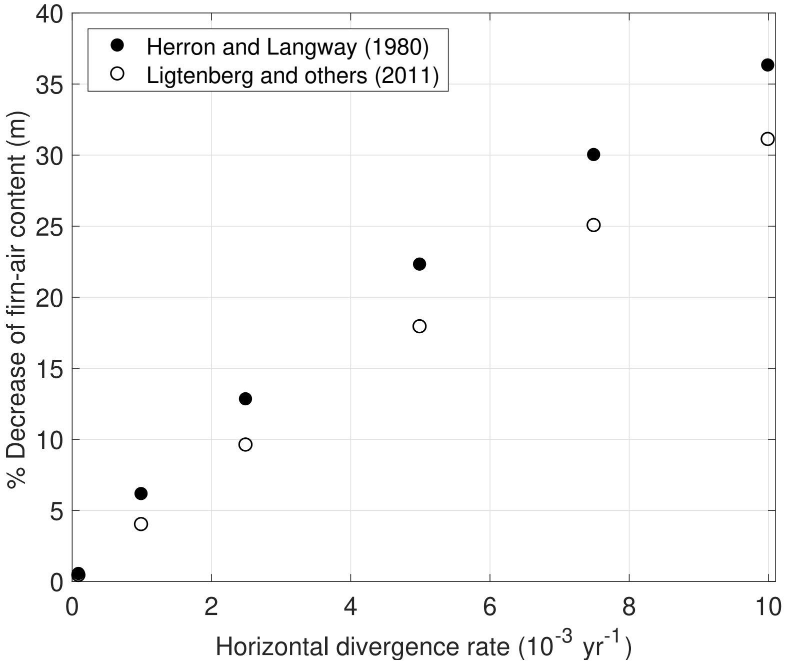

Figure 2.3: Estimated firn-air content (FAC) using the layer-thinning scheme to account for horizontal divergence with the HL and LIG firn-compaction models. The greater the step-change in horizontal divergence rate, the greater the decrease in the FAC after the step change.

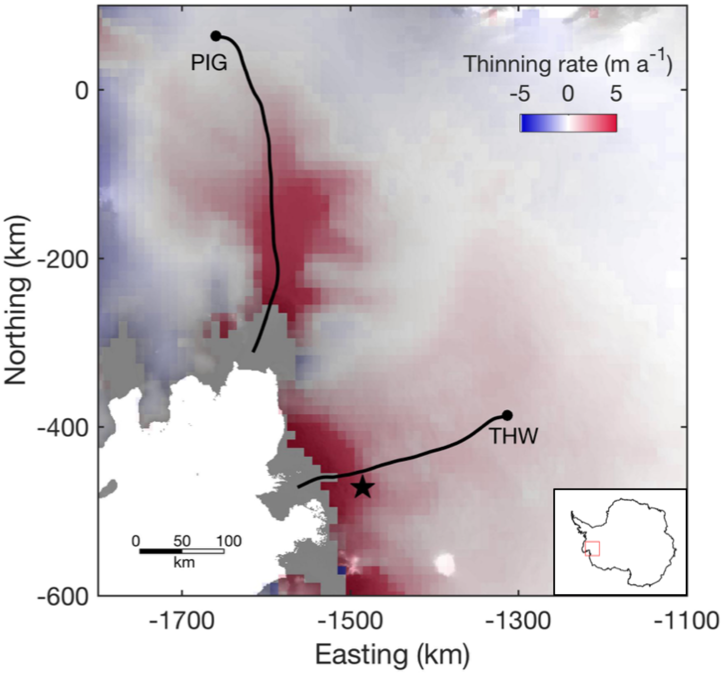

Figure 2.4: Location of Experiment 2 (THW) and Experiment 3 (PIG) on a map of mean thinning rate for 1978 to 2018 (Schröder et al., 2019). The black star represents the location on lower Thwaites used in Experiment 4. Map is superimposed on Reference Elevation Model of Antarctica (REMA) ice-sheet surface elevation (Howat et al., 2019). Inset shows location of figure domain in Antarctica. The projection is polar stereographic (EPSG: 3031).

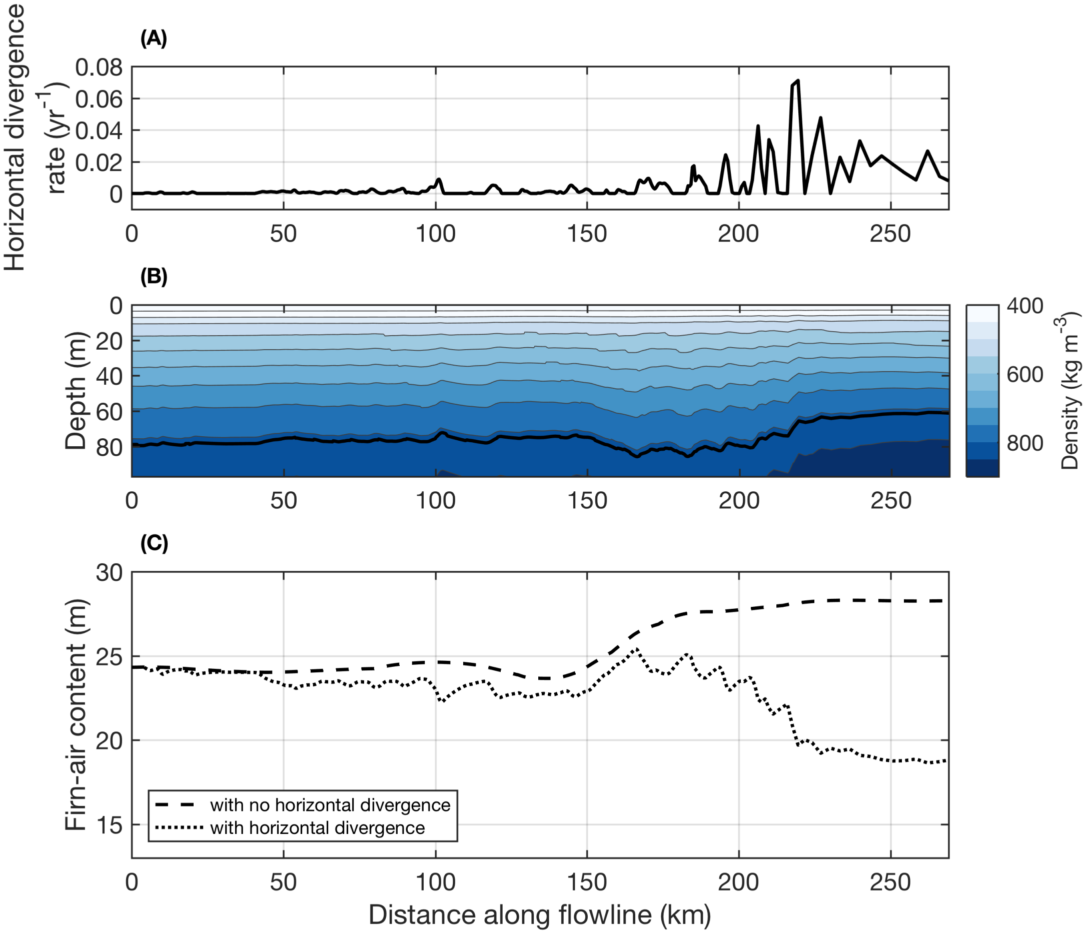

Figure 2.5: Results from the layer-thinning scheme for the flowline on Thwaites Glacier using the LIG firn-compaction model (Experiment 2). (A) Horizontal divergence rates for the flowline. Horizontal divergence rates were derived from Mouginot et al. (2019a) following the approach of Alley et al. (2018), and exclude compression. (B) The firn depth-density profiles along the flowline for the model that accounts for horizontal divergence. Black line indicates the BCO depth. Contour interval is 50 kg m^{-3}. (C) FAC results from model runs including the horizontal divergence rates shown in (A) (dotted line) and from a model without the horizontal divergence rates (dashed line).

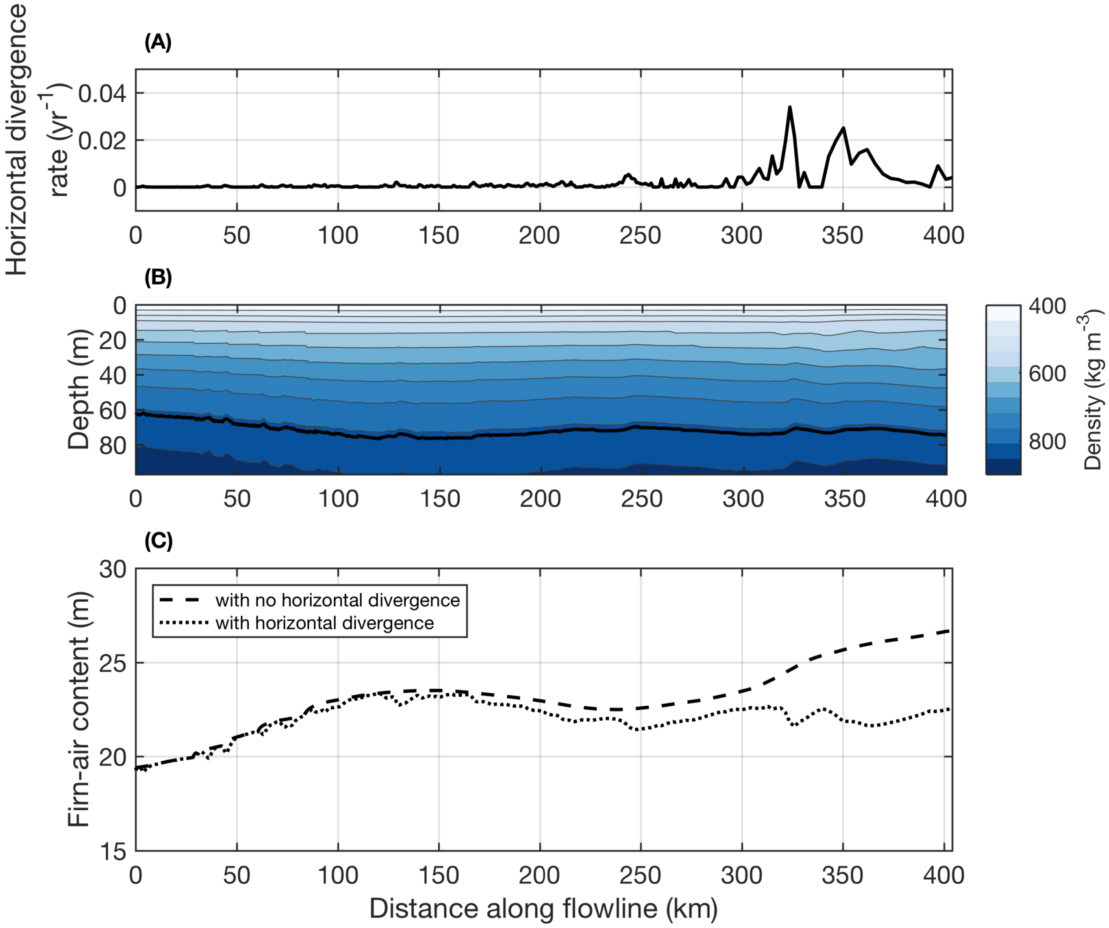

Figure 2.6: Results from the layer-thinning scheme for a flowline on Pine Island Glacier using the Ligtenberg et al. (2011) firn-compaction model (Experiment 3). (A) Horizontal divergence rates for the flowline. Horizontal divergence rates were derived from Mouginot et al. (2019a) following the approach of Alley et al. (2018), and exclude compression. (B) The firn depth-density profiles along the flowline for the model that accounts for horizontal divergence. Black line indicates the BCO depth. Contour interval is 50 kg m^{-3}. (C) FAC results from model runs with the horizontal divergence rates shown in (A) (dotted line) and from a model without horizontal divergence rates (dashed line).

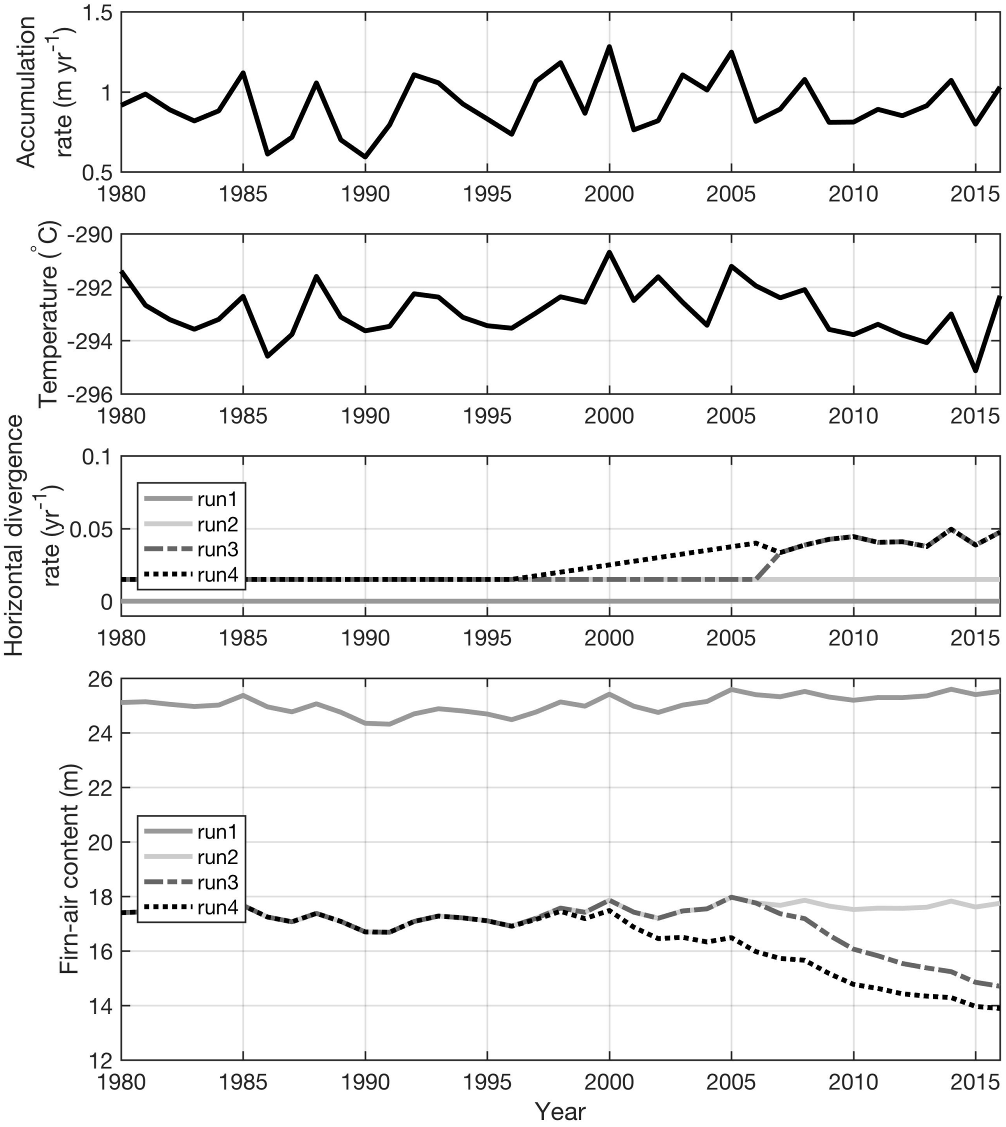

Figure 2.7: Surface boundary conditions, horizontal divergence rates, and estimated FAC using the layer-thinning scheme with the LIG firn-compaction model for a location on lower Thwaites Glacier (Experiment 4). The model spin up from 1980-2007 is shown. Run 1 represents a conventional firn-compaction model run with no horizontal divergence. A constant horizontal divergence rate of 0.015 yr^{-1} is used in run 2. For runs 3 and 4, after spin up with a constant divergence rate of 0.015 yr^{-1}, the model is run from 2007 to 2016 with temporally variable horizontal divergence rates derived from the Mouginot et al., 2017 velocity time series. Run 4 also includes a linear ramp between horizontal divergence rates from the 1997 to 2007 values.

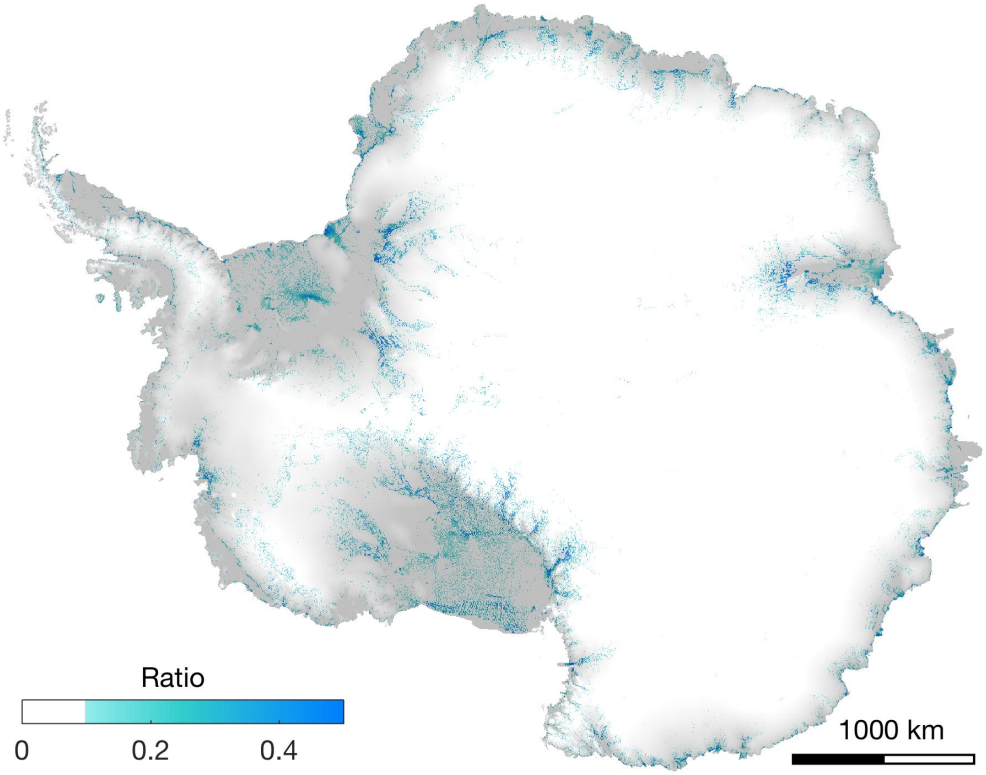

Figure 2.8: Ratio (R) of the vertical and horizontal divergence rates across the Antarctic Ice Sheet. Higher values of R show where horizontal divergence rates are more important to consider in calculations of firn-air content.

Chapter 3

EXPANSION OF FIRN AQUIFERS IN SOUTHEAST GREENLAND

Chapter 3, in full, is a reprint of “Expansion of Firn Aquifers in Southeast Greenland" authored by A.N. Horlings, K. Christianson, and C. Miège, as it appears in *Journal of Geophysical Research* 2022. The supplement for this paper can be found in Appendix B. The dissertation author was the primary investigator and author of this paper.

3.1 Abstract

Surface melt produces more mass loss than any other process on the Greenland Ice Sheet. In some regions of Greenland with high summer surface melt and high winter snow accumulation, the warm porous firn of the percolation zone can retain liquid meltwater through the winter. These regions of water-saturated firn, which may persist for longer than one year, are known as firn aquifers, commonly referred to as perennial firn aquifers. Here, we use airborne ice-penetrating radar data from the Center for Remote Sensing of Ice Sheets (CReSIS) to document the extent of four firn aquifers in the Helheim, Ikertivaq, and Køge Bugt glacier basins with more than six repeat radar flight lines from 1993 to 2018. All four firn aquifers first appear and/or show decadal-scale inland expansion during this time period. Through an idealized energy-balance calculation utilizing reanalysis data from Modèle Atmosphérique Régionale (MAR) regional climate model, we find that these aquifer expansions are driven by decreasing cold content in the firn since the late 1990s and recently increasing high-melt years, which has reduced the firn's ability for refreezing local meltwater. High-melt years are projected to increase on the Greenland Ice Sheet and may contribute to the continued inland expansion of firn aquifers, impacting the ice sheet's surface mass balance and hydrological

controls on ice dynamics.

3.2 Plain Language Summary

Warm atmospheric temperatures over the Greenland Ice Sheet can melt snow at the surface, producing liquid meltwater that can infiltrate downward into denser and older snow known as firn. The firn can retain this liquid meltwater continuously for more than one year in certain regions of the ice sheet that have high snow accumulation and high surface melt. These water-saturated regions of firn are called firn aquifers, which are important in understanding the ice sheet's mass loss to the oceans. To determine the evolution of firn aquifers in Greenland and what factors primarily influence their behavior, we examine airborne ice-penetrating radar data that were collected from 1993 to 2018. From the repeat detections of four firn aquifers in southeast Greenland, we find that the aquifers first appear and/or expand inland during this time period. Regional historical climate data and an idealized energy budget calculation suggest that aquifer expansions are driven by warming firn since the 1990s: the firn is not cold enough to refreeze increasingly large amounts of surface melt, and therefore the meltwater remains in a liquid state. More extreme warm summers are expected for Greenland, which may contribute to the formation and continued expansion of firn aquifers.

3.3 Introduction

Currently, the Greenland Ice Sheet is the single largest cryospheric contributor to sea-level rise and, in recent decades, has lost mass at an increasing rate (Broeke et al., 2016; Mouginot et al., 2019b; Shepherd et al., 2020). Of the Greenland Ice Sheet's mass loss since 2000, surface melt constitutes approximately 55% (Shepherd et al., 2020). However, processes involved in meltwater transit through the supraglacial, englacial, and subglacial hydrological systems of the ice sheet are not well understood, especially within the context of a warming climate. In some regions of the ice sheet with high summer surface melt combined with high winter snow accumulation, the warm porous firn of the percolation zone can retain surface meltwater without refreezing during winter; these water-saturated regions of firn are known as firn aquifers (Forster et al., 2014). Firn aquifers can influence ice-sheet flow and surface mass balance (Montgomery et al., 2020; Poinar et al., 2019, 2017), yet remain a relatively understudied piece of the ice sheet's hydrological system.

In this study, we focus on firn aquifers which retain liquid meltwater for more than one year (commonly known as perennial firn aquifers; we shorten this terminology to firn aquifers). While recent studies found that firn aquifers do not contribute to long-term water storage that could substantially buffer sea level (Miller et al., 2020), quantifying the evolution of firn aquifers in the present and future is important because they affect ice-sheet dynamics and thermodynamics by: (1) changing the seasonal behavior of the hydrological system and potentially moderating seasonal downstream ice velocities, through creation of englacial and subglacial channels that persist over the winter (Poinar et al., 2019); (2) influencing firn-compaction processes, meltwater flow and meltwater retention in the firn (Miller et al., 2020; Munneke et al., 2014; Munneke et al., 2015); (3) impacting the thermal regime of the ice sheet, as they represent large reservoirs of latent heat (Munneke et al., 2015); and (4) contributing to structural loading of ice shelves, especially on the Antarctic Peninsula, which may enhance hydrofracturing and lead to their eventual breakup (Montgomery et al., 2020).

The first well-studied seasonal firn aquifers were documented beginning in the 1980s in the high-accumulation and high-melt regions of temperate alpine glaciers; for example, the late summer/early autumn aquifers of the Oetztal Alps in Austria, Storglaciären in Sweden, and South Cascade Glacier in the United States (Fountain, 1989; Fountain and Walder, 1998; Jansson et al., 2003; Oerter and Rauert, 1982; Schneider, 1999). During the Arctic Circle Traverse expedition in 2011, firn aquifers were first observed in southeast Greenland from firn cores (Forster et al., 2014). Subsequently, several field studies conducted extensive in-situ and geophysical measurements at a firn aquifer located in upstream Helheim Glacier in southeast Greenland (summarized in Miller et al. (2020)). Other recent studies have further assessed firn aquifers there and elsewhere, including along the perimeter of the Greenland Ice Sheet, on the Holtedahlfonna Ice Field in Svalbard, in the St. Elias Mountains of Canada and Alaska, and on the Wilkins Ice Shelf in Antarctica, and have focused on characterizing aquifer extent, monitoring aquifer changes, and understanding the physical principles guiding aquifer formation and behavior (Christianson et al., 2015; Chu et al., 2018; Forster et al., 2014; Humphrey et al., 2021; Koenig et al., 2014; Miège et al., 2016; Miller et al., 2020; Montgomery et al., 2020; Ochwat et al., 2021; Shang et al., 2022).

Despite this, little is known about how changes in atmospheric forcing influence firn-aquifer extent, water flow, timescale of formation, evolution, and the role of firn aquifers in ice-sheet hydrology (Miller et al., 2021), motivating further study. It is generally accepted that the formation of firn aquifers requires high summer surface melt (approximately >0.24-0.65 m yr^{-1} w.e.) and high snow accumulation (approximately >0.8 m w.e. yr^{-1}) (Forster et al., 2014; Miller et al., 2020). These conditions are pervasive especially in the percolation zone of the southeastern periphery of the Greenland Ice Sheet. There, firn aquifers may occupy roughly 54,800 km^2, as estimated through Sentinel-1 radar data (Brangers et al., 2020).

For the southeast Greenland Ice Sheet, Miége et al. (2016) documented the widespread existence of firn aquifers using ice-penetrating radar data and showed that the firn aquifer detected at Helheim Glacier expanded toward the ice-sheet interior from 2010 to 2014. Miller et al. (2020) highlighted continued expansion of the Helheim firn aquifer until 2017 and hypothesized its formation between 1963 and 2006. Firn aquifers have likely existed undetected for over 40 years in the deep firn of the Greenland Ice Sheet's percolation zone, as suggested by the congruence of recent mapped extent of firn aquifers (Forster et al., 2014) and observations from historical 1978 Ku-band radar backscatter imagery (Miller et al., 2020). Longer and more continuous time-series analysis of firn aquifers using ice-penetrating radar data (the most direct remote-sensing method for imaging firn aquifers) has, however, not yet been conducted. In addition, the recent expansion of the Helheim firn aquifer (Miège et al., 2016; Miller et al., 2020) has been attributed to increased surface melt rates from warming atmospheric temperatures (Miller et al., 2020). While aquifer recharge has been observed in response to high melt (Christianson et al., 2015), the link between changes in atmospheric forcing, especially more frequent and more intense melt seasons, and multi-decadal aquifer response has not been thoroughly investigated. Modeling studies (Ochwat et al., 2021; Steger et al., 2017; Vandecrux et al., 2020) have begun to evaluate or apply firn model simulations at aquifer sites; however, firn meltwater models in general still misrepresent firn aquifers due to, for example, the difficulty in simulating lateral subsurface water flow, saturated conditions, and aquifer drainage (Vandecrux et al., 2020).

We motivate our study through the following questions: Has the spatial extent of firn aquifers across southeast Greenland changed in recent decades? Are years with high meltwater production impacting the expansion of these firn aquifers? We hypothesize that upstream expansion of firn aquifers (toward the ice-sheet interior) in southeast Greenland will occur in response to high-melt years if the firn has insufficient cold content for refreezing. Alternatively, firn aquifers may intermittently drain into downstream crevasses and the aquifer water table may deepen, hindering expansion (if lateral discharge exceeds surface-melt recharge). We use a subset of mapped firn aquifers to test our hypothesis: four locations in southeast Greenland with more than six usable repeat radar flight lines. We extend the firn aquifer time series to as far back as 1993 by identifying the presence of the aquifers in airborne ice-penetrating radar data.

Our study is the first to extend the firn aquifer time series to earlier than 2010. It is also the first to consider regions beyond Helheim Glacier to evaluate trends in expansion of firn aquifers on regional scales across southeast Greenland. Finally, it is also the first to use regional climate reanalysis data to evaluate climate controls on the expansion of firn aquifers in Greenland.

3.4 Materials and Methods

3.4.1 Sites

We assess four firn aquifers in southeast Greenland (Figure 3.1). H1 is located in upper Helheim Glacier, approximately between 1450 m and 1800 m elevation; H4 is located south of H1, approximately between 1400 and 1800 m elevation; IN1 is located in upper Ikertivaq

Glacier approximately between 1300 and 1750 m elevation; and KBS1 is located inland of Køge Bay, and lies approximately between 1300 and 1700 m elevation. We focus on these sites because they have multiple repeat Center for the Remote Sensing of Ice Sheets (CReSIS) radar flight lines equal to or exceeding six individual years that are roughly oriented interior-seaward (i.e., along the surface-elevation gradient of the ice sheet).

3.4.2 CReSIS Airborne Radar Sounding Observations

We use data from two airborne ice-penetrating radar systems designed and operated by CReSIS at the University of Kansas: the Accumulation Radar (AR) and the Multichannel Coherent Radar Depth Sounder (RDS) systems (Leuschen et al., 2014; Rodriguez-Morales et al., 2013). Both the AR and RDS radar systems were operated by NASA's Operation IceBridge (OIB) aerogeophysical surveying campaigns aboard P-3 aircrafts (2010 - 2018). The RDS system was also operated on a C-130 Hercules aircraft in 2015; however, the AR system was omitted due to non-optimal wing configuration for mounting antennas. Earlier versions of the RDS system were operated by the Radar Systems and Remote Sensing Laboratory at the University of Kansas on earlier aerogeophysical missions dating back to 1993 aboard P-3, DC8, C-130, TO, and Basler (DC3) aircrafts.

The AR system is an ultra-high-frequency radar generally operated with a center frequency of 750 MHz and bandwidth of 300 MHz. It images the upper portion of the ice sheet, penetrating up to 500 m in depth for smooth, spectral targets (Leuschen et al., 2014; Miège et al., 2016). AR radar profiles are generally available Greenland-wide from 2010 - 2014 and 2017 - 2019. The AR system directly images the water table of a firn aquifer as a high-amplitude reflector, due to the high dielectric contrast between dry and water-saturated firn (Chu et al., 2018; Miège et al., 2016).

The RDS system operated at many different bandwidths over time during different surveys, primarily between 140 and 210 MHz for the data used in this study, and is designed to image the ice-sheet bed. RDS data are available Greenland-wide from 1993, 1995 - 1999, and 2001- 2019. We use a novel technique to determine the presence of a firn aquifer from

RDS data, first pioneered by Miége et al. (2016): within the RDS radar profiles, the firn aquifer can be identified via its interference with subsequent reflections. The disappearance of the reflection from the ice-sheet bed (and disappearance of internal layers) indicates the presence of water, as water within the firn increases the attenuation and scattering of the radar wave. Comparison of AR and RDS datasets during overlapping years corroborates this interpretation (Figure 3.2; Supporting Information).

3.4.3 Radar Interpretation

We use ImpDAR, an open-source radar processing and interpretation toolbox (Lilien et al., 2020), to interpret radar signals and map the firn aquifers from the CReSIS radar-sounding data. Through visual interpretation with some user input for control, we use a semi-automatic picking routine in ImpDAR to digitize the bright firn water-table reflector in the AR radar profiles and to map the inferred extent of a firn aquifer by the absence of internal layers and bed reflector in the RDS radar profiles, as suggested in Miége et al. (2016). We categorize extent as the interior-seaward linear distance spanned by the aquifer along chosen flight lines. We project extents from flight lines that are slightly oblique to the coast onto an interior-seaward direction so that different radar profiles can be compared.

The firn aquifers appear in both AR and RDS radar profiles when the data are contemporaneous. Agreement between AR and RDS firn-aquifer detections for each basin is high (Figure 3.2; Supporting Information), where the bright reflector in the AR radar profiles of the water table (illustrating water-saturated firn) correlates with the disappearance of the bed reflector in contemporaneous RDS radar profiles at the same location. Miége et al. (2016) also noticed good agreement when identifying the firn-aquifer locations on the two airborne radar systems. Additionally, water-volume data from magnetic resonance soundings (Legchenko et al., 2018) has shown good agreement between high water volumes at a firn-aquifer site and disappearance of the bed reflector in the RDS data (Supporting Information). These results allow us to confidently extend the time series of firn-aquifer extent before 2010 (the beginning of the AR data) to the start of the RDS observations in 1993, when only RDS data are available.

The RDS and AR systems differ through time due to system improvements, including hardware, which result in changing transmit power, bandwidth, range resolution, and dynamic range. These variables are documented in detail in the Supporting Information. The range resolution varies from 2.5 m in recent RDS systems to 4.2 m in earlier systems, while the AR systems vary from 0.58 m to 0.62 m. Along-track resolution is dependent on processing, as well as along-track, cross-track, and aircraft height characteristics. The differences in the systems do not substantially impact the results of this study, as we are interpreting relative changes in the bedrock reflector and water-table reflector within individual years to infer the horizontal extent of the aquifer. While earlier RDS systems were operated with less power (e.g., in 1993) than more recent years (e.g., 2006), the bed reflector appears more continuous in earlier years (e.g., 1993) and disappears in recent years (e.g., 2001 onward) in correlation with the appearance of the water table of the firn aquifer in the AR data.

In addition, because picking the aquifer extent in the radar profiles was not a fully automated process and is subject to human bias, there is some uncertainty in the identified aquifer extent. These uncertainties are described further in Miège et al. (2016). Disagreement in aquifer detections between the two radar systems occurs primarily where the intensity of internal reflectors weaken at the edges of the water table or at the edges of the disappearing bed reflector.

We define aquifer "expansion" as the progression of aquifer detections toward the ice-sheet interior as determined by changes in linear extent. In contrast, we use the concept of aquifer "migration" as the progression of both upstream and downstream linear extent of the aquifer toward the ice-sheet interior. Also, we define a single "firn aquifer" as a near-continuous detection (no detection gaps >10 km) of the water table and/or associated disappearance of the bed along the chosen repeat flight lines, following Miège et al. (2016). We acknowledge that the aquifers that we identify may be interconnected in a larger aquifer system; however, with the limited flight extent, we cannot verify that they are connected and therefore assume that the identified aquifers in this study operate largely independently from each other.

3.4.4 Regional Climate Model

To assess the climatic factors contributing to aquifer evolution, we use reanalysis data from the Modèle Atmosphérique Régional MAR 3.5.2 (Fettweis and Rennermalm, 2020a), a regional atmospheric model designed to simulate kilometer-scale to continental-scale processes over multi-decadal timescales in the polar regions. Firn-aquifer formation is governed by the balance of generated surface meltwater infiltrating downward into the firn and the ability of the firn to refreeze this meltwater. We therefore analyze the annual melt, snow accumulation, the melt-to-surface-mass-balance ratio, wintertime (December to February) temperature, number of days above a defined melt threshold (0.5 mm per day), and annual rainfall. We take the mean of these climate parameters for the closest cell to the aquifer locations because MAR's resolution is relatively coarse (20 km) for application to a single aquifer. In addition, we determine the long-term trend, decadal mean and standard deviation. We also calculate the change points of the time series for each climate parameter, defined as the time instant at which the mean of the time series changes abruptly, through a parametric global method (Killick et al., 2012; Lavielle, 2005) (Supporting Information).

3.5 Results

3.5.1 Multidecadal Airborne Radar Sounding Observations

We present evidence of multidecadal firn-aquifer expansion from ice-penetrating radar profiles in southeast Greenland from 1993-2018. The firn aquifers are first detected on all four repeat flight lines between 1998 and 2013 and three with recent data show subsequent expansion toward the ice-sheet interior (Figure 3.3). Other sites are not investigated as few repeat flight lines exist there. We describe each of the four sites in this study in further detail.

Helheim Firn Aquifer (H1)

The most repeat flight-line coverage is over H1 with a combination of RDS and AR data available in 1993, 1998, 2001, 2003, 2005, 2006, 2010-2014 and 2017-2018. Both AR and

RDS radar imagery individually and collectively show the expansion upstream toward the ice-sheet interior (Figure 3.3). The aquifer is first detected within our data at this site in 1998; it subsequently expanded 0.3 km from 1998-2001; 1.8 km from 2001-2003; did not expand from 2003-2005; then an upstream, more isolated extension of the aquifer (5.9 km upstream) appears between 2005 and 2006. Following this, a substantial expansion of the main firn aquifer occurred between 2006 and 2010, where the firn aquifer expanded upstream by 8.1 km inland. This was followed by a further 3.3-km expansion until 2012. An upstream, more isolated extension of the aquifer (3.6 km upstream) appears to persist in 2017 and disappears in 2018, while the upstream extent of the main aquifer appears to remain approximately similar from 2012-2018 (Figure 3.3).

Increases in the depth of the water table (i.e., water discharge) of the Helheim aquifer in 2012 have been attributed to drainage through downstream crevasses (Miège et al., 2016; Miller et al., 2020). This drainage may have a delayed effect on suppressing inland expansion, as the inland portion of the water table is slower to respond to the drainage compared to the downstream end nearest to the crevasses. However, observations show recharge (decrease of water-table depth) from 2013-2016, which is also associated with the appearance of the upstream extension of the firn aquifer in 2017.

Helheim 4 Firn Aquifer (H4)

A combination of RDS and AR data are available for H4 in 1993, 1998, 2001, 2002, 2006, 2010, 2014, 2017, and 2018. The first detection of H4 is in 2001. While the aquifer decreased in upstream extent by 1.2 km from 2001 and 2002, the aquifer subsequently expanded by 0.5 km from 2002 to 2006. Then, between 2006 and 2010, the aquifer expanded by 25.9 km upstream; between 2010 and 2014, the aquifer expanded by 6.3 km; and between 2014 and 2017, the aquifer expanded by 8.2 km upstream. Finally, the aquifer decreased in extent by 7.35 km between 2017 and 2018.

Ikertivaq North Firn Aquifer (IN1)

For IN1, a combination of RDS and AR data are available for 1993, 1998, 2001, 2002, 2006, 2011, 2012, 2014, and 2017. The first detection of the aquifer at IN1 is in 1998. From 1998 to 2001, the aquifer slightly decreased in upstream extent by 0.6 km. From 2001 to 2002, the aquifer expanded upstream 2.9 km and subsequently expanded 3.2 km upstream from 2002 to 2006. From 2006 to 2011, the aquifer expanded 5.5 km upstream; from 2011-2012, it expanded 2 km; and between 2012-2014, the aquifer expanded 4.7 km, and finally decreased in upstream extent from 2014 to 2017 by 4.8 km.

Koge Bugt South Firn Aquifer (KBS1)

RDS data are available for KGBS1 for 1993, 1998, 2001, 2002, 2005, and 2013. AR data are available in 2013. The main aquifer is first detected in 2013; however, we do not have any subsequent data along the repeat flight line, so cannot present any results on its further evolution.

Altogether, our analysis of repeat ice-penetrating radar profiles at the four sites suggests that firn aquifers in southeast Greenland are forming in regions at higher elevations and are expanding upstream toward the ice-sheet interior during most years. However, we do not observe that the downstream extents of the firn aquifers are migrating toward the ice-sheet interior.

3.5.2 Climate Forcing on Firn Aquifers in Southeast Greenland

Cumulative annual melt generally increases from 1948 to 2017, though the trend is not statistically significant ($R = 0.337$). Cumulative annual melt exceeding one standard deviation from the long-term mean occurs during the years 1957, 1998, 2004, 2005, 2007, 2010, 2012, 2014, and 2016. The most substantial high-melt year over the aquifer sites was in 2012, which is also known to be a significant melt year Greenland-wide (Nghiem et al., 2012). Winter snow accumulation (defined here as cumulative snow accumulation from December to February) is highly variable and shows a slight increase over the time period that is not statistically significant ($R = 0.130$). The melt-to-surface mass balance ratio is dominated by the annual melt signal. Annual winter surface temperatures show a slight long-term warming trend ($R = 0.120$). Extreme annual rainfall occurred in 2010, while the number of days above the defined melt threshold (> 0.5 mm per year) increases slightly beginning in the mid 1990s. However, for some high-melt years such as 2007 and 2012, the number of days occurring above this melt threshold are below or within one standard deviation of the long-term mean despite a high total annual melt, respectively. This suggests that a few very intense melt events dominated those summer seasons, which is in line with satellite observations showing that the 2012 summer season was governed by intense short-lived melt events (Nghiem et al., 2012).

Of the climate parameters analyzed from 1948 to 2016, we find most substantial recent changes in the surface melt and winter temperature (Figure 3.4). We calculated decadal averages and determined change points, which determine the time at which the mean of the time series changes abruptly. These analyses show that the surface melt increase is most marked beginning in 2004 (increase in the mean by 0.19 mWE) and the winter temperature increased substantially after 1997 (increase in the mean by 2.54 °C). In addition, we find a relation between upstream firn-aquifer extent and high-melt years (Figure 3.3e); maximum extent for H1, H4, and IN1 and the first detection of KBS1 follows 2012 high-melt year, while H1, H4, and IN1 appear to increase in extent following other high-melt years (e.g., 2007 and 2010). All other analyses of melt, snowfall, temperature, and rainfall variables from MAR for 1948-2016 are presented in the Supporting Information.

3.5.3 Linking Aquifer Expansion to Climate through Firn Cold Content

To link the observed firn-aquifer expansion to changes in climate, we investigate the energy balance that permits aquifer formation. Following Culberg et al. (2021) and Humphrey et al. (2021), we relate the cold content (CC) of the firn with the latent heat content from surface melt (LH_{melt}). While firn models can calculate cold content, meltwater schemes and their ability to simulate firn aquifers are not consistent across models (Vandecrux et al., 2020). Therefore, we use idealized calculations to characterize this complex thermodynamic system. We define the cold content and latent heat for the upper 20 m of the firn column following Culberg et al. (2021) as:

$$CC = 20c\rho_f T_f. \tag{3.1}$$

$$LH_{melt} = L_h M \rho_w. \tag{3.2}$$

Here, c is the heat capacity of ice, ρ_f is the volume-weighted mean annual density of the firn, T_f is the absolute value of the mass-weighted mean annual firn temperature in degrees Celsius, L_h is the latent heat of fusion for water, M is the total annual melt in m w.e.q., and ρ_w is the density of water. Firn density and temperature values are derived from the MAR model output. We apply the calculations to 20 m in depth because this is the depth to which MAR defines its domain (Fettweis and Rennermalm, 2020a). The shallow firn is also most relevant to the energy redistribution in the firn column due to heat conduction and meltwater refreezing (Vandecrux et al., 2020). We can then quantify the relative capacity of the upper firn column to refreeze surface meltwater as the ratio between latent heat and cold content (γ).

$$\gamma = \frac{L_h M \rho_w}{20c\rho_f T_f}. \tag{3.3}$$

When γ increases, the firn loses some of its ability to refreeze meltwater and when γ is small, the firn has sufficient cold content for refreezing. We choose to not define the specific quantity of meltwater that infiltrates into the firn, as this depends on a number of variables that firn models still struggle to properly simulate (Vandecrux et al., 2020); therefore, γ remains a relative assessment of the energy balance in the firn, which we use to monitor relative values between regions and to measure temporal trends. Further, we define potential firn-aquifer conditions as regions with warm firn and a plentiful meltwater supply. These conditions are necessary but may be insufficient for firn-aquifer formation, as surface topography, crevasse proximity, and the hydraulic gradient also influence location and evolution of firn aquifers.

We calculate the CC, LH_{melt}, and γ at six different sites in southeast Greenland representing different regions (Figure 3.5). We delineate these six regions to generally exemplify the state of the firn at and adjacent to the firn-aquifer sites that are a focus of this study (regions 1-4) and at higher and lower latitude sites at the upstream extent of other detected aquifers (regions 5-6, respectively). For each of these general regions, we take the climate conditions described by the MAR cells that are closest to: (1) low-elevation aquifer sites, at the downstream edges of the aquifers of this study; (2) upstream aquifer sites, at the most upstream edges of the aquifers of this study; (3) site adjacent to the upstream aquifer edge and the ice-layer region, where the aquifers are expanding; (4) interior sites, inland and at higher elevations to the aquifers of this study and within the ice-layer region; (5) higher-latitude upstream aquifer sites, at the most upstream edges of detected aquifers in eastern Greenland; and (6) lower-latitude upstream aquifer sites, at the most upstream edges of detected aquifers in southern Greenland.

Our calculations show that the firn cold content is decreasing at and to the interior of the upstream edges of the aquifers of this study (2, 3 and 4) starting in the late 1990s and early 2000s, as well as other aquifers farther north (5) and south (6) in latitude. The latent heat to cold content ratios (γ) at the northern-latitude sites (5) and adjacent to the upstream edge of the aquifers of this study (3) increase during this time but are generally lower than at the upstream site (2) and and southern site (6). The value of γ at the interior site (4) generally remains lowest of all sites at less than one, though reached this value in 2012. The firn cold content at the higher-elevation sites directly upstream of the four aquifers (3 and 4) have higher cold content than within the aquifer sites (1 and 2). The lowest-elevation site at the downstream portion of the aquifers (1) shows the lowest cold content that does not show a trend, and also has the highest value of γ.

3.6 Discussion

All four firn aquifers that we assessed through ice-penetrating radar develop during the analysis period. Three of the firn aquifers with recent data (H1, H4, and IN1) appear to non-monotonically expand toward the ice-sheet interior and reach maximum upstream extent following the high-melt year in 2012 (Figure 3.3e). We also observe substantial interannual variability in aquifer extent that may be due to drainages or changes in local meltwater availability.

The generally accepted paradigm is that firn-aquifer formation occurs under high-melt conditions, which allow surface meltwater to infiltrate deep within the firn, and under high-accumulation conditions, which insulate the liquid meltwater from the winter cold (Munneke et al., 2014). Liquid meltwater exists within the firn when top-down refreezing (from the winter cold) and bottom-boundary refreezing (from the cold deep firn, as a result of loss of heat from diffusion ahead of the infiltrating water front) are unable to refreeze the infiltrating meltwater (Humphrey et al., 2021). The downward percolation of water will be halted if the cold content of the firn is greater than the latent heat of the infiltrating meltwater. While diffusion ahead of the water front can be theoretically large and prevent meltwater from accessing the full firn pore space, aquifers at locations with high meltwater availability will more likely be influenced by top-down refreezing (Humphrey et al., 2021). The relative energy balance of firn in high-melt regions illustrated in Equation 3.3 shows that the link between firn-aquifer conditions and atmospheric forcing is mainly through the availability of snow melt (supply of liquid water and latent heat), the snow accumulation (for the pore space and for the buffer from winter temperatures), and surface-air temperature (which controls the cold content of the firn).

Our observations indicate a decrease in the firn's capacity for refreezing meltwater in southeastern Greenland beginning in the late 1990s and early 2000s. Specifically, the firn cold content adjacent to the upstream edge of H1, H4, IN1, and KBS1 aquifers (regions 2 and 3) began consistently losing some capacity to refreeze the increasing volume of meltwater beginning in 1997. We observe the highest γ value is attained in 2007, 2010, and 2012, which correspond to notable high-melt years. Our radar detections of the firn aquifers show formation during the late 1990s, followed by a non-monotonic expansion that continues until the most recent detections documented in this study in 2018 (excluding KBS1, where the last usable radar profile is in 2013). While drainages and connections to other aquifers may add complexity, which can be difficult to assess with existing radar profiles, our results suggest that the firn aquifers in southeast Greenland are expanding inland in response to the firn's decreased capacity for refreezing and an increase in surface meltwater availability. This confirms our hypothesis: that upstream expansion of firn aquifers in southeast Greenland will occur in response to high-melt years if the firn warms and the cold content is insufficient for refreezing. Recent coupled firn-thermodynamic and hydrology modeling of meltwater infiltration at DYE-2 show that the firn is strongly impacted by high-melt years such as those in 2012 and 2019 through the increase of firn temperature, ice content, and firn density (Samimi et al., 2021), which supports our results.

Ice layers, which occur when percolating meltwater is refrozen following high-melt years, occur directly upstream of firn-aquifer locations on the ice sheet (Figure 3.5) (Culberg et al., 2021). The change in the energy balance at higher elevations above the firn aquifers is reflected in our calculations of the ratio of cold content and latent heat from meltwater. This switch in firn characteristics is important to understand because the presence of extensive ice layers complicates water percolation (Miège et al., 2016). Ice layers can isolate deep firn pore space to force meltwater to discharge into efficient surface runoff systems ("firn runoff regime"; Machguth et al., 2016), or to create perched water tables (Christianson et al., 2015; Miège et al., 2016). While we do not observe any melt layers in the ice-penetrating radar datasets for the chosen flight-line segments, it is suspected that melt-layer formation may promote firn-aquifer expansion by "priming" the firn through the release of latent heat into the surrounding cold firn during refreezing, by amplifying meltwater input downstream through migration of the meltwater laterally along the low-permeability ice layers under low hydraulic gradients, and/or by reducing vertical percolation (Culberg et al., 2021; Killingbeck et al., 2020; Miège et al., 2016). Thus, melt layers may introduce an additional local hydrological process that influences aquifer formation and behavior. For example, the intense melt year in 2012 initiated ice-layer formation upstream of the firn aquifer at Helheim Glacier, which may have formed a perched firn aquifer and may have increased meltwater input into the aquifer region (Culberg et al., 2021; Miège et al., 2016).

We also observe that there are multiple timescales of firn-aquifer behavior. Decadal-scale aquifer behavior is driven by a decrease in cold content, increase in atmospheric warming, and increase in frequency of high-melt years. In contrast, lower amplitude interannual variability may be controlled by aquifer drainages, while seasonal expansion and retreat of the aquifer is due to fluctuating meltwater availability through the year. While there is temporal variability between firn aquifers, our results suggest that warming firn conditions generally facilitate inland expansion in tandem with increasingly high meltwater availability. Ultimately, upstream and inland migration of glaciological facies (e.g., superimposed-ice zone, wet-snow zone, and the percolation zone), as seen in similar climate regimes to the Greenland Ice Sheet, such as the Devon Ice Cap (Gascon et al., 2013), will likely influence future firn-aquifer and ice-layer formation on the Greenland Ice Sheet; however, we did not detect the migration of the lower limit of firn aquifers in this study.

With the projected increase in the frequency and duration of high summer surface melt due to warming conditions over the Greenland Ice Sheet during the 21st century (Field et al., 2012), firn aquifers likely will expand to higher elevations and affect ice-sheet hydrology and mass balance over larger areas. It remains unknown whether firn aquifers drain continuously or episodically. However, drainage of firn-aquifer water overall has the potential to create persistent subglacial channels through the winter due to continued high-water pressure and to facilitate fast downstream channel growth during the summer melt season; this can ultimately dampen downglacier seasonal ice-velocity fluctuations (Poinar et al., 2019). In addition, firn aquifers have been predicted near the grounding lines of many ice shelves of the rapidly changing Antarctic Peninsula (AP), including the former Prince Gustav, Wilkins and Wordie ice shelves (Wessem et al., 2021) and have been directly observed on the Wilkins ice shelf

(Montgomery et al., 2020). Climate on the AP is similar to southeast Greenland, with high snow accumulation and high surface melt during the summer (Van Wessem et al., 2016; Wessem et al., 2021) and even föhn-induced melt in the winter season (Munneke et al., 2014). With increasing precipitation rates (Thomas et al., 2008) and increasing atmospheric warming and surface melt (Abram et al., 2013; Turner et al., 2014), firn aquifers will be increasingly important to understand on the AP, as they may potentially accelerate the disintegration of ice shelves that buttress outlet glacier discharge to the oceans.

3.7 Conclusion

We assessed the extent of four firn aquifers in southeast Greenland through the last three decades using airborne ice-penetrating radar products. The accumulation radar (AR) data can detect the firn-aquifer water table and the radar depth-sounder (RDS) data can detect disappearance of the bed reflector due to the presence of the firn aquifer. We find that all four firn aquifers were initially identified along the flight lines and/or show inland expansion during the observational period of 1993 to 2018. We find that this multi-decadal firn-aquifer expansion is mainly driven by decreasing cold content and increasing surface melt, which has decreased the firn's capacity for refreezing since the late 1990s. Specifically, recent warm, high-melt years such as 2007, 2010, and 2012 have decreased the firn's ability for refreezing adjacent to the upstream edge and at higher elevations to the firn-aquifer sites. Continued warming over the Greenland Ice Sheet (e.g., 2010 and 2012; Nghiem et al., 2012), increasing melt, and more frequent and intense high-melt years will likely contribute to a continued reduction in the firn's ability to refreeze meltwater through reducing the firn cold content and hindering top-down and lower-boundary refreezing of infiltrating meltwater, as well as introducing increased availability of meltwater. We may expect firn aquifers to continue to form and expand upstream in these regions of warming firn and to occupy greater areas of the Greenland Ice Sheet. Because of this, our understanding of how firn aquifers contribute to the Greenland Ice Sheet's mass balance, hydrology, and ice dynamics is vital. Future work should investigate broader-scale trends in aquifer behavior across Greenland and the

Antarctic Peninsula; constrain in-situ meltwater flow and discharge measurements to refine firn physics and to improve self-consistency of meltwater firn models; and downsize climate reanalysis data to finer grids to capture climate forcing on smaller scales at which firn-aquifer evolution occurs.

3.8 Code and Data Availability

All ice-penetrating radar data used in this study are available from the CReSIS public FTP pages: `ftp://data.cresis.ku.edu/data/accum/` (CRESIS, 2021a) and `https://data.cresis.ku.edu/data/rds/` (CRESIS, 2021b). Aquifer detections from the accumulation radar (Miège, 2018) are also available at the NSF Arctic Data Center at: `https://arcticdata.io/catalog/view/doi\%3A10.18739\%2FA2TM72225`. MARv3.5.2 climate model simulation outputs and metadata are available from the NSF Arctic Data Center at: `https://arcticdata.io/catalog/view/doi\%3A10.18739\%2FA2H12V80V` (Fettweis and Rennermalm, 2020b). The DEM for Greenland is available on the NSIDC website at: `https://nsidc.org/data/NSIDC-0645/versions/1` (Howat and Smith, 2015). Outputs from this study are also available from the authors without conditions.

3.9 Acknowledgements

ANH, KC, and CM designed the study. ANH interpreted the CReSIS radar data and MAR output data with input from KC. All authors contributed to writing the manuscript. We are grateful to Sean O'Neil, who contributed to radar interpretation during the early part of this project. We also thank Nick Holschuh, Michelle Koutnik, and T.J. Fudge for comments on the manuscript draft. We acknowledge the use of data from CReSIS and the University of Kansas generated with support from NSF OPP 0424589 and NASA Operation IceBridge grant NNX16AH54G. We acknowledge Xavier Fettweis at the University of Liège for the availability of MAR output data. We thank Editor Olga Sergienko and Associate Editor Paul Winberry for the handling of the manuscript, as well as the two anonymous reviewers. We acknowledge NSF Grant OPP-0909499, NSF Grant EAGER-1311655, and the

NASA ESS Fellowship program (NNX11AL64H), which helped to support ANH and CM. Finally, we acknowledge the University of Washington Innovation Award that supported KC.

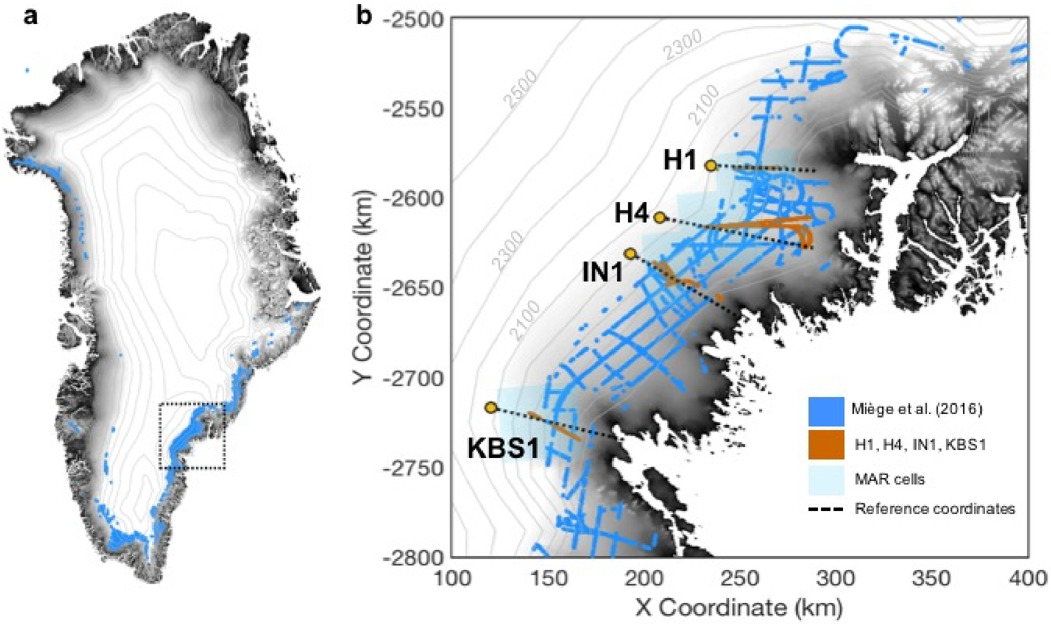

Figure 3.1: a) Map of southeast Greenland showing aquifer detections from Miège et al. (2016). The dashed box shows our focus region. b) The four firn-aquifer sites that are the focus of this study, as shown in reference to the aquifer detections from Miège et al. (2016). The aquifer sites are labeled: Helheim 1 (H1), Helheim 4 (H4), Ikertivaq N1 (IN1), and Køge Bugt S1 (KBS1). Dashed lines show the location of the reference coordinates on which our aquifer detections along the four repeat flight line segments (brown) were projected onto, roughly in the direction of the surface-elevation gradient. Blue boxes denote the MAR cells used for Section 4.2. Elevation contours (relative to the WGS84 Ellipsoid) are derived from MEaSUREs Greenland Ice Mapping Project (GIMP) Digital Elevation Model, Version 1, gridded to a polar stereographic projection (EPSG:3413).

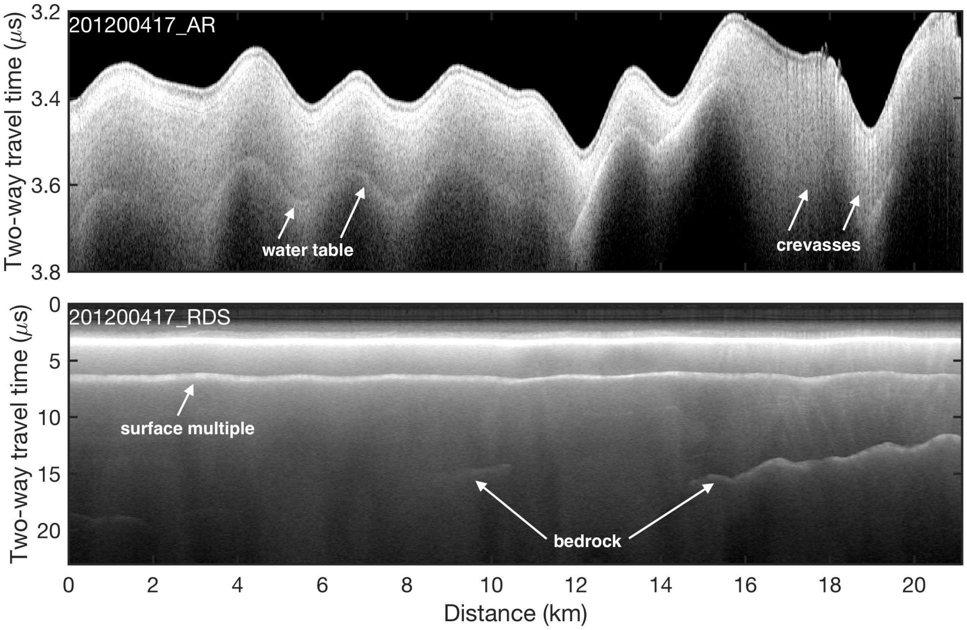

Figure 3.2: a) Accumulation radar (AR) and b) MCoRDS (RDS) profiles showing the firn aquifer at upper Helheim Glacier (H1 in Figure 1), which were collected on April 17, 2012. The firn water table is the bright continuous reflector in the upper firn in the AR profiles. The absence of the bed reflector in the RDS data correlates with the presence of the water table reflector in the accumulation radar profile. Left-hand side of the figure is toward the ice-sheet interior.

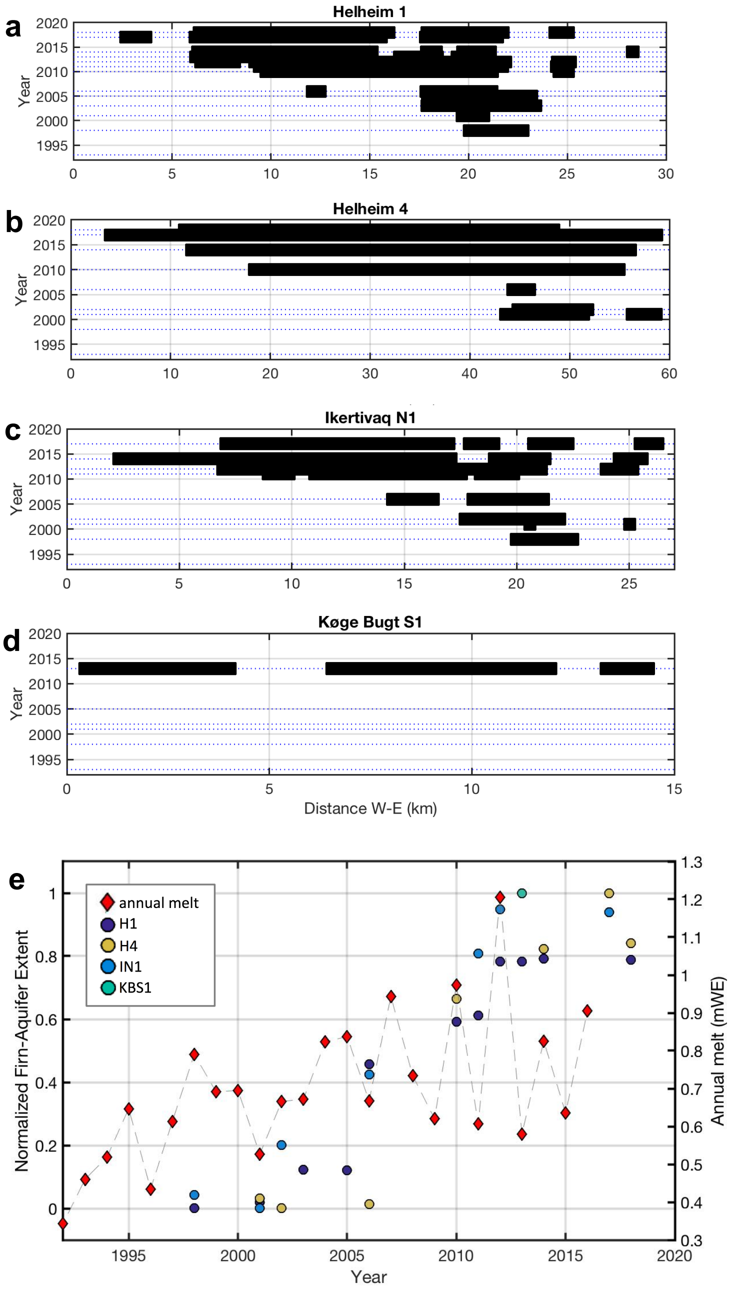

Figure 3.3: Firn-aquifer detections (black markers) along each repeat flight line using both the AR and RDS radar profiles: a) H1, b) H4, c) IN1, and d) KBS1. Blue dotted lines indicate years that data is present. We assume that each aquifer incorporates the detections along the repeated flight line as long as there are no gaps greater than 10 km. e) shows the maximum inland extent for all of the aquifer and the annual melt.

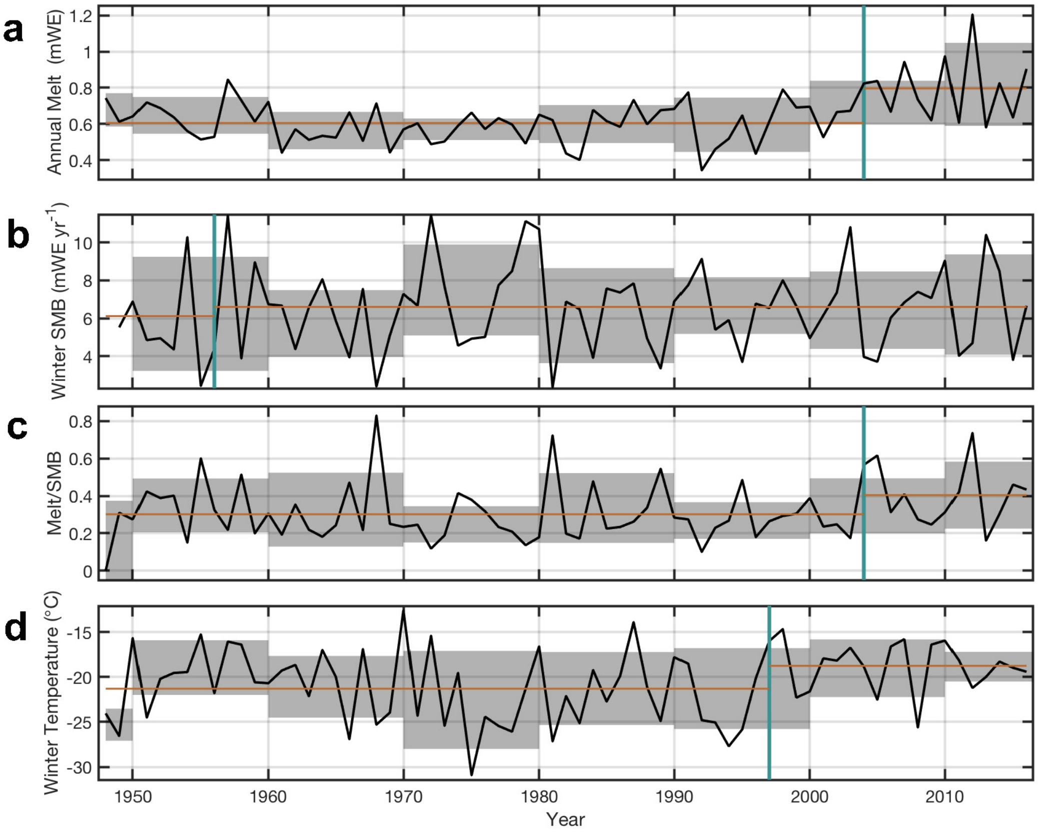

Figure 3.4: MAR reanalysis for the upstream portion of the aquifers. We choose to show these variables because firn-aquifer formation is governed by the balance of generated surface meltwater infiltrating downward into the firn and the ability of the firn to refreeze this meltwater. (a) Map showing aquifer detections from Miège et al. (2016) (blue) and from this study (brown). MAR cells closest to the aquifer sites (brown diamonds) have a resolution of 20 km. (b) Total annual melt. (c) Previous winter's surface mass balance. (d) Ratio of melt and the previous winter's surface mass balance. (e) Mean winter temperature. Decadal mean with decadal standard deviation is represented in gray. Blue vertical lines denote the change point for the time series mean. Brown horizontal lines denote the mean for the time period before and after the detected change point. The location of MAR cell extent nearest to the aquifers over which the climate output was averaged shown in map.

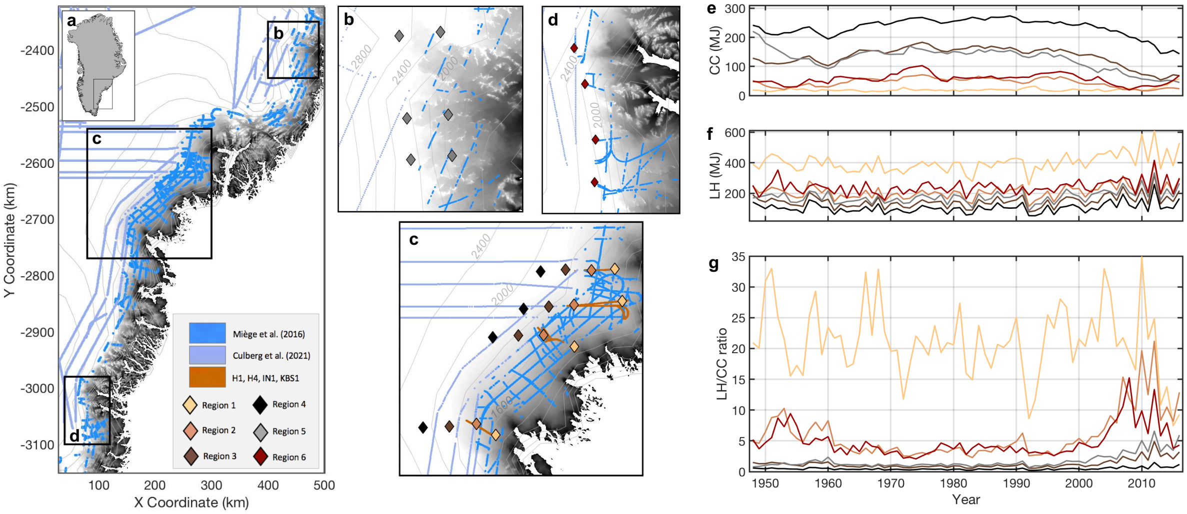

Figure 3.5: (a-d) Maps showing the subset of regions over which the MAR output was averaged, queried as approximately 15 km from the center of target region 1-6, denoted as diamonds. Aquifer detections from Miege et al. (2016) in royal blue are shown. The ice layers from Culberg et al. (2016) in light blue are inland and adjacent to the aquifers. Aquifer detections from this study are shown in brown. (e) Cold content averaged over each region, colors corresponding locations of cells shown on the map. (f) Latent heat content from meltwater. (g) The ratio of latent heat to cold content.

Chapter 4

SNOW ACCUMULATION AT HERCULES DOME, ANTARCTICA

Chapter 4, in full, will be submitted to *Geophysical Research Letters* authored by A.N. Horlings et al. The supplement for this paper can be found in Appendix C. The dissertation author was the primary investigator and author of this paper.

4.1 Abstract

Observed and modeled snow-accumulation patterns in the interior of the Antarctic Ice Sheet remain limited in spatial resolution. At Hercules Dome, Antarctica, a prospective ice-core site, only one observation of the snow-accumulation rate exists and the accuracy of climate models remains limited there. We use ground-based very high frequency ground-penetrating radar data collected during the 2019-2020 and 2022-2023 austral summers to construct the first spatially resolved snow-accumulation dataset over Hercules Dome. The radar data reveal three promininent reflectors, which we assume are isochronal. The three isochrones can be assigned dates of 225, 326, and 420 years from a 70-m firn-core record obtained during the International TransAntarctic Scientific Expedition traverse in 2002. We find that the 420-year, 326-year, and 225-year time-averaged accumulation rates are similar and range from 0.10 to 0.15 m a^{-1} ice equivalent across the divide, with greater accumulation to the grid north (EPSG:3031) toward the Filchner-Ronne sector. The grid south to grid north snow-accumulation rates increase as much as 35% in as little as a 20-km profile across the divide. We suggest that the snow-accumulation pattern results from a combination of regional orographic precipitation and local snow redistribution from prevailing storms and winds originating from the grid north.

4.2 Plain Language Summary

Hercules Dome is the site of a prospective ice core designed to capture the state of the West Antarctic Ice Sheet during Earth's previous warm period. Characterizing the distribution of snow accumulation is key for ice-core site selection and, eventually, ice-core interpretation. Here, we use spatial patterns in firn thickness (where firn is simply compacted snow) together with firn ages measured from a shallow core to map the snow-accumulation variability across Hercules Dome, Antarctica. We find a 35% increase in the snow-accumulation rates across Hercules Dome toward the Filchner-Ronne sector in as little as a 20-km transect, and also find that the snow-accumulation rates and spatial pattern have been relatively stable over the last 420 years. We suggest that the spatial variability is linked to the prevailing wind direction of storms and to local snow redistribution.

4.3 Introduction

On the Antarctic Ice Sheet, snow-accumulation rates vary spatially due to moisture-source proximity, synoptic conditions in coastal areas, orography, wind scour and redeposition, sublimation, and clear-sky precipitation (Bromwich et al., 2004; Das et al., 2013; Roe, 2005). Further, variations in temperature and atmospheric circulation (due to both multi-millenial global climate change and internal variability) can drive changes in both the magnitude and spatial pattern of snow accumulation through time. However, knowledge of snow accumulation in the interior of the Antarctic Ice Sheet remains limited by the spatiotemporal resolution of observations. Here, we characterize the snow-accumulation rates in detail at Hercules Dome, Antarctica from a ground-based very high frequency ground-penetrating radar survey conducted in the 2019-2020 and 2022-2023 austral summers.

Hercules Dome (86° S, 105° W) is a prospective ice-core site located in East Antarctica between the Horlick and Thiel ranges of the Transantarctic Mountains and approximately 400 km from the South Pole. The region is a triple divide characterized by two local surface rises and two ridges (Figure 4.1). Atmospheric circulation at Hercules Dome is sensitive to thinning of the West Antarctic Ice Sheet (WAIS) during the last interglacial period (∼130 ka) (Dütsch et al., 2023; Steig et al., 2015), yet ice flow and surface elevation at the dome likely changed very little (Fudge et al., 2022; Jacobel et al., 2005). The dome summit at the grid-westernmost part of Hercules Dome, called “Summit" (previously known as “West Dome") has been identified as a promising location for a prospective deep ice core with a climate record that would reflect the extent of the WAIS during the last interglacial (Fudge et al., 2022).

While satellite observations and regional and global climate models may determine snow accumulation with a horizontal resolution of tens to several kilometers, they struggle to capture local features and variability even in topographically smooth locations in interior Antarctica (Das et al., 2013). More highly resolved characterization of the surface accumulation is integral for the Hercules Dome Ice Core Project for a number of reasons: (1) providing regional context for the prospective ice core and determining how representative the ice core is spatially; (2) potentially explaining high-frequency variability in the highly temporally resolved ice-core record induced, as changes in the small-scale snow-accumulation pattern may produce variability in the snow-isotope composition at a single point; (3) providing necessary input to modeling the gas age-ice age difference because the accumulation rate is the primary control on the vertical velocity of the firn/ice column in regions of slow flow.

Ground-penetrating radar data is an effective tool for characterizing past and present spatial variability in snow-accumulation rates, which cannot be inferred from ice-core records alone. Radar images capture the englacial stratigraphy and can be used to map internal layer depths. Spatial variability in layer thickness can be related to the patterns of snow-accumulation, firn-densification, and longitudinal strain (Dahl-Jensen et al., 1997; Karlsson et al., 2020; Medley et al., 2013; Miege et al., 2013; Richardson et al., 1997). In slow-flowing regions such as Hercules Dome, an ice divide, divergence plays a small role in the layer depth and affects all layers nearly equally; thus, our data primarily capture snow accumulation and densification processes carried out in the near surface.

Here, we present the first spatially resolved measurements of snow-accumulation rates at Hercules Dome and evaluate their temporal variability over the last 420 years. Many studies have shown that the surface slope strongly influences snow deposition and the spatial distribution of the accumulation rate at other Antarctic ice domes and ice rises (e.g., at Siple Dome: Hamilton, 2002; at Talos Dome and Dome C: Urbini et al., 2008 at ice rises in the Princess Ranhild Coast: Cavitte et al., 2022) and along longer traverses (e.g., the Syowa-South Pole traverse: Yasoichi et al., 1973; the Dome Fuji-Syowa route: Fujita et al., 2002; the DML-South Pole traverse: Anschütz et al., 2011; Müller et al., 2010). Following these studies, we motivate our work through the following questions: (1) What is the spatial accumulation pattern over Hercules Dome? (2) Has the pattern changed over the past 420 years? (3) What processes influence snow deposition at Hercules Dome? We discuss the main results in terms of spatial distribution of and temporal variations in the snow-accumulation rates, and related local and regional snow-accumulation processes.

4.4 Data and Methodology

We conducted a ground-based very high frequency ground-penetrating radar survey at Hercules Dome in the 2019-2020 and 2022-2023 austral summers. We used a commercial PulseEkko ground-penetrating radar system with 100 MHz antennas at a fixed separation (∼1 m) on a Nansen sled and towed by a snowmobile moving at a speed of ∼5-10 km hr^{-1}. Processing of the data included bandpass filtering, correction for antenna separation, geolocation from contemporaneous kinematic precision GNSS data, interpolation to standard trace spacing, and an exponential range gain to increase the relative amplitude of deeper reflections.

Radar profiles were collected roughly parallel (grid west to grid east) and orthogonal (grid north to grid south) to the primary ice-divide ridge (Figure 4.1). Grid directions refer to polar stereographic coordinates (EPSG: 3031), where grid north is toward the Filchner-Ronne sector and grid south is toward the Ross Sea sector. The main concentration of profiles is near the grid eastern portion of the dome (“East Dome”), where the 2019-2020 camp was located. A short shallow-radar survey was conducted at Hercules Dome Summit in the 2019-2020 season, and a more extensive radial survey was completed during the 2022-2023 season. A total of 320-line kilometers of shallow radar profiles were collected across both field seasons. We track the surface and three distinct internal layers within the data, which were selected for their relatively high continuity across all radar profiles. We traced the internal layers using a semi-automatic layer digitization routine available in ImpDAR, an open-source impulse radar processing and interpretation toolbox (Lilien et al., 2020).

To calculate snow-accumulation rates, we must first calculate the depth and age of the internal layers. The two-way travel time (TWTT) recorded by the radar receiver must first be converted to depth. Because the velocity of radar waves is dependent on the firn density, we use the Looyenga dielectric mixing relation (Looyenga, 1965) with a modeled firn-density profile (Herron and Langway, 1980) to calculate the depth of the internal layers. In reality, the depth-density profiles will spatially vary; however, we calculate that the error caused by this is a few % at most here (Supporting Information). For the depth-age relation, we use the depth-age scale from the 70-m ITASE-2002-03 core (Dixon et al., 2004; Steig et al., 2005), which was collected during the ITASE traverse at 86.5025°S, 107.99°E and extends from 1592 to 2003. The easternmost part of the 2019-2020 VHF radar survey is located about 1 km grid west of the firn-core site. The internal layers are then dated by transferring the established depth-age relationship from the firn core to the closest radar profile (Figure 4.2), as layer slopes are low. We assume a steady-state depth-age profile over the period from 2003 to 2019 and correct for the 17-year difference between the radar and firn-core collection.

Using the calculated depth and age, the time-averaged snow-accumulation rate is then derived as the integrated mass from the surface to the three reflectors divided by their ages; we hereafter refer to these resulting time periods as T1 (1599-2019; 420 years old), T2 (1693-2019; 326 years old), and T3 (1794-2019; 225 years old). T1 is based on a distinctly bright reflector that is present in all radargrams. We note that due to the lack of a direct radar link between East Dome and Summit, the continuity of other reflectors between East and West Dome cannot be verified; thus, we only report T1 for Summit. Ice thicknesses range from 1500 to 2800 m in the region, which suggests that all englacial reflectors tracked in this study are less than 3-5% of the ice thickness from the surface and that these internal layers are therefore primarily dependent on the surface snow-accumulation rate.

We use surface slopes, bed topography, and climate-model output to analyze conditions that influence the variability of the snow-accumulation rates. Surface slopes are calculated as the derivative of along-track surface elevations from the GNSS measurements recorded contemporaneous to the radar profiling. GNSS measurements provide higher resolution information on surface topography than gridded regional digital elevation models, so we choose to rely on these to calculate local slopes despite only capturing information along-track. Bed topography is derived through digitization of the bed reflector from the deep high-frequency ground-penetrating radar data collected at Hercules Dome during the 2018-2019, 2019-2020, and 2022-2023 field seasons (Fudge et al., 2022; Hoffman et al., in review). Daily snowfall rates, sublimation rates, 10-m wind direction, and 10-m wind speed are derived from ERA5 land daily reanalysis product for 2018-2020 (Muñoz-Sabater, 2019a), ERA5 land monthly reanalysis product for 1950-2023 (Muñoz-Sabater, 2019b), and CMIP6 GFDL-ESM4 historical product for 1850-2014 (Zhang et al., 2019).

4.5 Results

4.5.1 Accumulation rates derived from ground-penetrating radar

Both the observed spatial pattern for snow-accumulation rates and the spatially averaged snow-accumulation rates for the three time periods T1 (1599-2019), T2 (1693-2019), and T3 (1794-2019) demonstrate low time-variability with mean values of 12.1, 11.8, and 11.8 cm a^{-1} (Supporting Information); this is supported by snow-accumulation rates derived from the firn core for each time period (12 cm a^{-1}, +/- 0.05 cm a^{-1}). We subsequently report values solely from the T1 period. Accumulation rates range from 10 to 15 cm a^{-1}, with a mean of 12.1 cm a^{-1} and a standard deviation of 1.3 cm a^{-1}. The snow-accumulation rates show two distinct spatial trends: (1) a regionally increasing grid north gradient, especially evident at Summit; and (2) significant variability on the kilometer-scale, especially evident at at East Dome. Snow-accumulation rates increase up to nearly 35% grid northward across the divide in as little as a 20-km profile. The total mean snow-accumulation rate for the region is in agreement with the total mean snow-accumulation rate of 12 cm a^{-1} derived from the ITASE-2002-04 firn core (Dixon et al., 2004; Jacobel et al., 2005)

Our accumulation results and those derived from the firn core differ in magnitude and variability from model-derived accumulation products at Hercules Dome. For example, output from ERA5 and the Antarctic Mesoscale Prediction System (AMPS) (which utilizes the Weather Research and Forecasting (WRF) and the Model for Prediction Across Scales (MPAS)) captures the grid north to grid south gradient, yet even the fine resolution (spatial resolution of 9 km and 2.67 km, respectively) does not capture the kilometer-scale variability recorded in the radar-derived accumulation rates. Accumulation rates from AMPS are particularly higher than observations in the Summit region (> 25 cm a^{-1}) and show a wider range of magnitudes, while ERA5 generally overestimates snow-accumulation rates by 3-4 cm a^{-1}. We suspect that our model/data disagreement arises from the coarse model resolution, which cannot capture the small-scale effects of surface topography on precipitation and snow redistribution.

Figure 4.3 shows snow-accumulation rates and surface slope along four shallow radar profiles. At East Dome, surface slopes are generally low over the dome, while reaching a maximum of 0.8 degrees, and show the highest variability. Topographic profiles at East Dome indicate that the largest surface slopes occur along the grid northwest of the shallow radar survey near a distinct surface depression. At Summit, surface slopes are generally less than 0.4 degrees, with a slight depression on the grid-northwest side. The snow-accumulation rate has a notable correlation with the along-track slope, with a cross-correlation coefficient of 0.78. Orientation of the profiles does not have an impact on the significance of the cross-correlation. Some grid north to grid south profiles show increased accumulation on the grid south side of topographic highs in topographic depressions, whereas some grid west-east profiles show increased accumulation on the western side of topographic highs (Figure 4.3).

4.5.2 Accumulation rates from climate data

We examine the 10-m wind fields to evaluate the influence of storm direction and wind redistribution on the snow-accumulation rate pattern. Analysis of the 10-m wind fields from ERA5 and CMIP6 across Hercules Dome shows that the region is characterized by a prevailing wind flow from the grid north-northeast, typically with speeds ranging from < 5 to 17 m a^{-1}. Wind speed and direction of the 10-m wind field, and the snow-accumulation rate is plotted in Figure 4.4. Daily averaged values are shown from ERA5 from 2018-2020 in the upper panels of Figure 4.4. Monthly averaged values are shown from CMIP6 from 1850-2014 in the lower panels of Figure 4.4. Wind directions are described as the direction the wind is moving toward, in degrees east of true north. If we define a "storm" as an event with non-zero precipitation, then the mean storm wind direction is from -30° east of true north with a standard deviation of 54°, and a mean magnitude of 7 km hr^{-1} with a standard deviation of 3 km hr^{-1}. More generally, wind speeds above 10 km hr^{-1} were observed for 13% of all cases (storm or no storm), with an average direction of -60° east of true north (with standard deviation of 35°) for daily observations in 2019 and 2020. Wind speeds from 5-10 km hr^{-1} were observed in 63% of cases with an average wind direction of -32° east of true north (with a standard deviation of 54°) for daily observations between 2018-2020; and 28% of cases, with an average direction of -46° for monthly averaged observations from 1850-2014. The total mean wind direction calculated from 1850-2014 from CMIP6 was -45° east of true north. Wind direction does not appear to change with time, at least since 1850 (Supporting Information).

4.6 Discussion

Our study determines the geospatial pattern of snow-accumulation rates across Hercules Dome, with values increasing from grid south to grid north and ranging from 10 to 15 cm a^{-1}. We also observe kilometer-scale variability, most evident at East Dome. The highest detected snow-accumulation rates appear linked to surface depressions on the grid-northwest of the Summit region.

Snow deposition on the Antarctic plateau is strongly influenced by surface topographical slope and curvature, where small changes can lead to high spatial variability of snow accumulation over distances as short as a few kilometers. At large, air masses lose water vapor to precipitation by orographic effects as they travel over the continent (Fujita et al., 2011). On a regional scale, ice divides, domes, and rises tend to cause regional orographic effects: uplift of atmospheric water vapor leads to precipitation on the windward side of the regional surface topographical high, where the high acts as a topographic barrier for transport of moisture and the leeward side essentially becomes a rain shadow. On a local scale, a combination of differences in water-vapor flux and snow redistribution by wind can lead to high spatial variability in the snow-accumulation rate, where snow accumulation is higher on relatively flat surfaces and in relative topographic depressions (Fujita et al., 2011; Miege et al., 2013).

We suggest that snow accumulation at Hercules Dome is dependent on the prevailing storms and winds originating from the Filchner-Ronne side of the divide. On a regional scale, Hercules Dome appears to be influenced by an orographic effect due to the surface topography of the divide: storm directions are primarily -30° from true north (with a standard deviation of 54°) (Figure 4.4), which is in line with the higher snow-accumulation rates on the Filchner-Ronne side of the divide, revealed by the results of this study. On a local scale, snow-accumulation rates are likely impacted by snow redistribution resulting from wind interactions with the local surface topographic variations. The region at East Dome appears to have high kilometer-scale variability compared to Summit and maps of along-track slope and accumulation for profiles in the grid north to grid south direction show increased accumulation in relative topographic depressions. Specifically, across all radar profiles, we observe the highest snow-accumulation rates (1) in a surface depression in the grid-northwest region of East Dome, a multi-kilometer wide feature, and (2) in the grid-northwest region of Summit at a local depression that is likely associated with a trough in the bed topography which originates at Summit and extends grid northwestward.

Local snow-accumulation patterns can be naturally maintained over time because surface slope is correlated with bedrock topography (e.g., Fujita et al., 2011), especially when the prevailing winds remain unchanged. At Hercules Dome, the result of this effect on a centuries-scale is confirmed by the similarity in local variability shown in all time-averaged accumulation rates (T1, T2, T3) at Summit, East Dome and South Ridge, while the mean prevailing wind direction remained steady since 1850 (Supporting Information). The divide at Summit overlies a bedrock high, but overall shows little bedrock and surface topographical variations and less spatial variability in snow accumulation. Surface morphology at East Dome is irregular and appears to be a result of the interplay between flow over a distinct bedrock trough and peaks that were formed by ice flow hundreds of thousands to millions of years ago (Hoffman et al., in review). The steadiness in recent snow-accumulation rates at Hercules Dome is consistent with other Antarctic sites during recent decades to the last few centuries (e.g., northern Victoria Land: Stenni et al., 1999; Dome Fuji: Van Liefferinge et al., 2021), while some other regions in East Antarctica have experienced an increase in accumulation rates (e.g., Talos Dome: Stenni et al., 2002; Dronning Maud Land: Fujita et al., 2011). Based on our study and available data, we cannot state whether the snow-accumulation pattern at Hercules Dome has remained steady beyond 420 years ago.

Ice-divide stability is a primary concern for drilling an ice core at Hercules Dome. Ice-divide position is dependent on the snow-accumulation distribution, as well as ice dynamics, such as draw-down away from the divide/spatial conditions at the ice-sheet boundary, and bedrock topography, which routes ice flow from the divide to the ocean (e.g., Hindmarsh, 1996). While internal layers at Summit suggest some instability preceding the mid-Holocene (Fudge et al., 2022), the question of divide stability still remains. Previous studies on ice-divide sensitivity (e.g., Hindmarsh, 1996) show that steady divide position is most sensitive to anti-symmetric accumulation-rate patterns near the divide. While margin draw-down can impact the divide position much greater than any other factor, short-term reversals in divide-migration direction due to high-frequency forcing from accumulation-rate variations may be more disruptive to the climate record of an ice core, where even small standard deviations with time in the accumulation pattern can produce stochastic divide variation (Hindmarsh, 1996).

The snow-accumulation dataset presented here should be useful for determining possible influence of climate changes on the ice core, inform recent variations in the ice-divide position, and provide a basis of comparison to long-term variations in ice-divide position. At Hercules Dome, the snow-accumulation pattern over the region is asymmetrical in relation to the dome morphology, and has not appeared to change over the last 420 years. Little change of accumulation rates during the recent past suggests that the dynamics of the dome have not changed much during this time period. Models of the depth-age scale for deep ice cores are sensitive to ice-divide migration (Anandakrishnan et al., 1994) and determining whether high-frequency variability in the core's climate record results from actual temporal variations in the climate history or spatial variations in the accumulation pattern and divide position is important. Further, the gas-age ice-age difference (i.e., the lock-in age at the bubble close-off depth minus the age of the enclosed gas; where the gas age is usually small, generally tens of years) is sensitive to changes in snow-accumulation rate (e.g., Lundin et al., 2016). Therefore, interpretation of the prospective deep ice core at Hercules Dome should consider the impacts of local spatial variability of the snow-accumulation rates on isotope diffusion and firn-densification processes.

4.7 Conclusions

Snow accumulation over the past 420 years was mapped with shallow ice-penetrating radar at Hercules Dome, Antarctica. Our dense survey grid enabled us to derive the first spatially distributed accumulation-rate dataset at the site and to document small-scale variations in snow-accumulation rates. We find that the 420-year, 330-year, and 225-year time-averaged accumulation rates are similar and spatially range from 0.10 m a^{-1} to 0.15 m a^{-1} ice equivalent. Greater accumulation rates exist to the grid north with as high as a 35% difference in as short as a 20-km profile. The regional mean radar-derived snow-accumulation rate agrees with mean snow-accumulation rates from the ITASE-02-04 firn core. We suggest that the snow accumulation results from an interaction of the grid north originating storms, orography from the regional surface topography of the divide, and variations in local surface topography that is likely linked to variability in the bed topography. Interpretation of the prospective deep ice core at Hercules Dome should consider the impacts of local spatial variability of snow accumulation on isotope diffusion and firn-densification processes.

4.8 Data Availability Statement

Radar data are archived at https://www.usap-dc.org/view/project/p0010359. The snow-accumulation dataset, slopes, and associated climate output will also be archived.

4.9 Acknowledgements

ANH designed the study, analyzed the radar data, computed the snow-accumulation rates, and analyzed the climate data with input from KC, AH, BH, LD, EJS, and TJF. EE, BH, ANH, and KC processed the data. LD, AH, and TJF contributed to preliminary analysis of the radar data. DR contributed to climate-model analysis. ANH, EE, BH, AH, NH, LK, TJF, EJS, and KC collected the radar data. All authors contributed to writing the manuscript. We graciously thank Kenn Borek Air and the US Antarctic Support Contract for logistical support; the 2019-2020 field guides Shannon Wilson and Vito Cicola; field managers Jenny Cunningham, Jennifer Blum, and Bija Sass. This research was supported by NSF grant #1744649. We also acknowledge the World Climate Research Programme, which, through its Working Group on Coupled Modelling, coordinated and promoted CMIP6. We thank the climate modeling groups for producing and making available their model output, the Earth System Grid Federation (ESGF) for archiving the data and providing access, and the multiple funding agencies who support CMIP6 and ESGF.

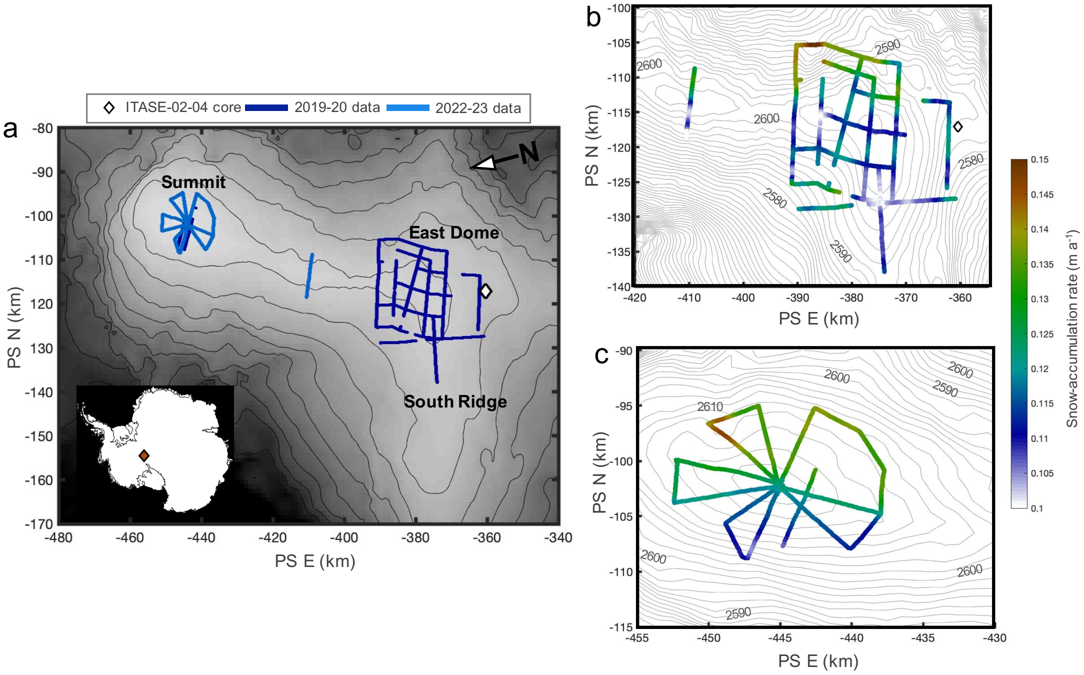

Figure 4.1: Profiles of snow-accumulation rates from T1 time period. a) Map showing the shallow radar survey at Hercules Dome, Antarctica. Dark blue designates data collected in the 2019-2020 field season. Light blue designates data collected in the 2022-2023 field season. Star is the location of the ITASE-02-04 firn core. Elevation contours are from Reference Elevation Model of Antarctica (REMA) ice-sheet surface elevation (Howat et al., 2019). The projection is EPSG: 3031. Inset shows location of figure domain in Antarctica. b) The Summit snow-accumulation rates derived from both the 2019-2020 and 2022-23 radar data. c) Hydra Rise snow-accumulation rates derived from the 2019-2020 radar data. Star represents the location of the ITASE-02-04 firn core.

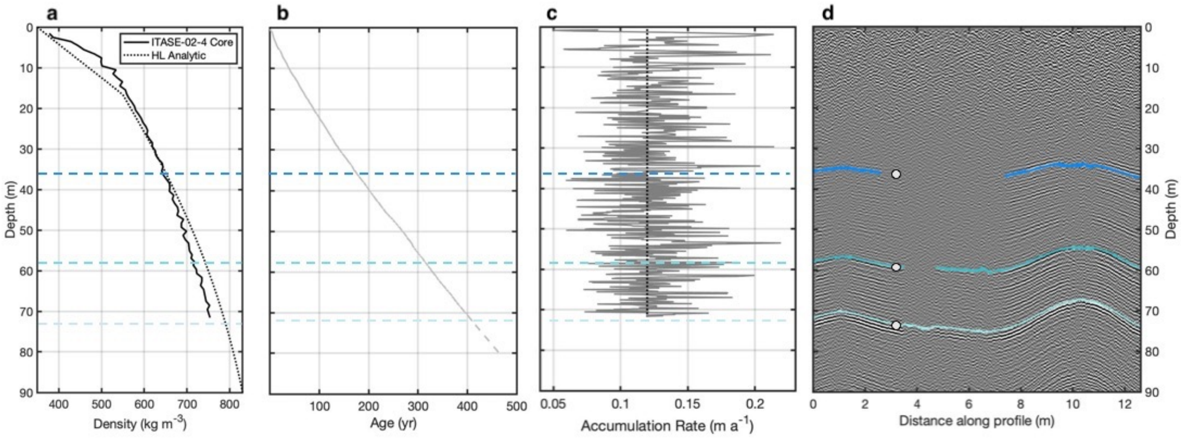

Figure 4.2: a) Bulk density data from the ITASE-2002-04 firn core, which was drilled to 72 m (Dixon et al., 2004; Steig et al., 2005). Black line denotes the Herron and Langway (1980) steady-state density profile used in the calculation of the accumulation rates. Only minor differences exist between the data and the model. b) Depth-age scale from the firn core. Note that dashed line indicates extrapolation for the deepest tracked englacial reflector. c) Inferred snow-accumulation rates inferred from the firn core. d) Radargram closest to the firn core with the three tracked reflectors highlighted. The depth-age scale was used to infer layer ages using the depths associated with the white points in panel d.

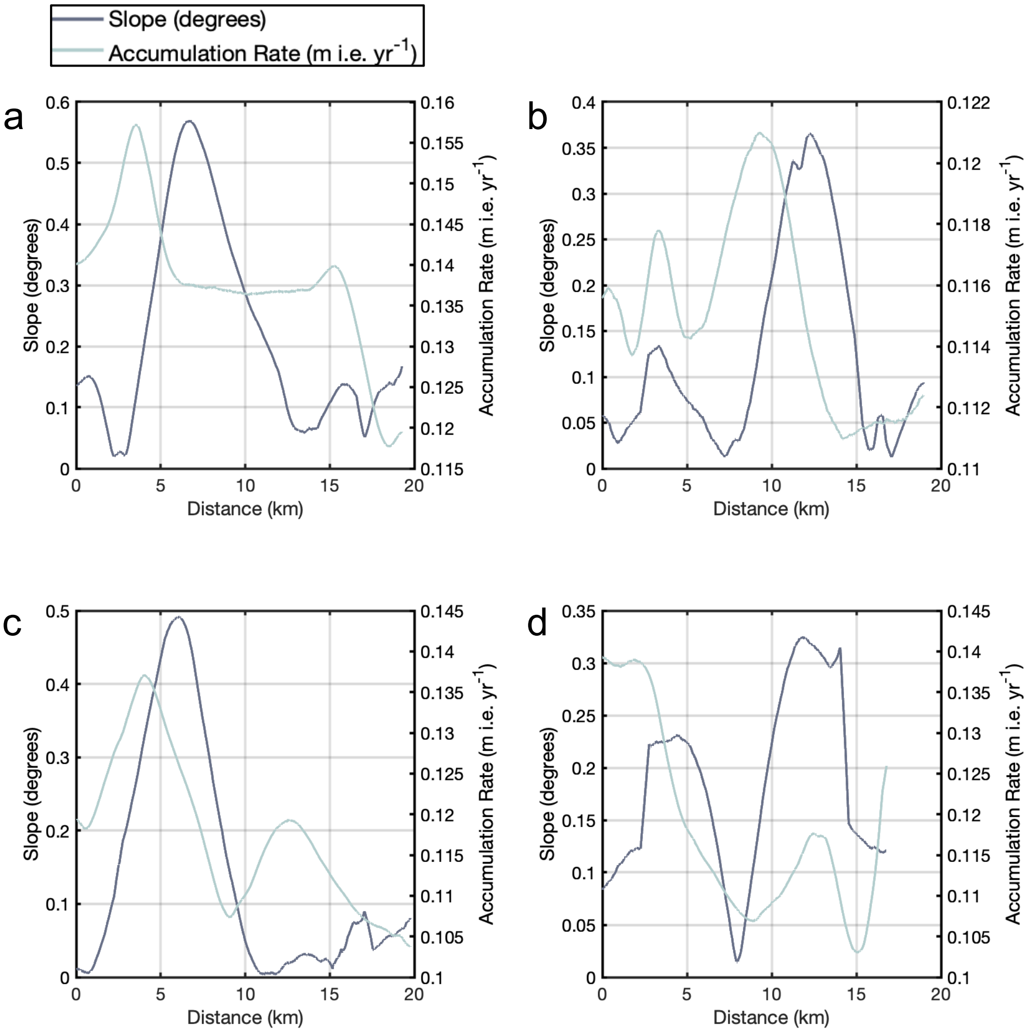

Figure 4.3: Snow accumulation rates and surface slopes along some of the shallow radar profiles. a) and b) are oriented grid north to grid south. c) and d) are oriented grid west to grid east.

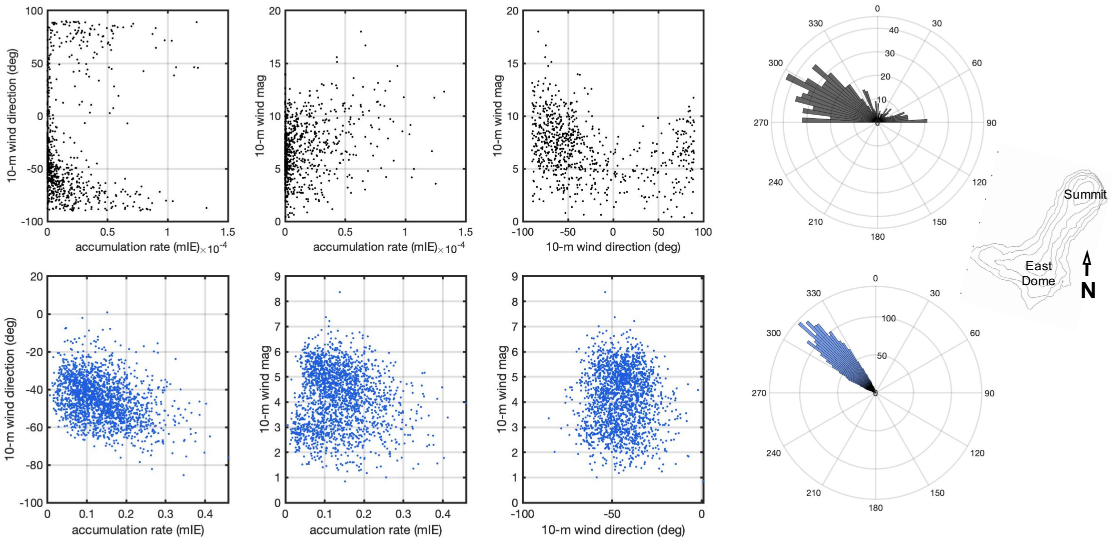

Figure 4.4: Relation between snow-accumulation, 10-m wind magnitude, and 10-m wind direction. The angle is the direction the wind is moving toward, measured in degrees East of North. For example, -50° therefore represents winds coming from the east of true north. Rose diagrams show direction of the 10-m winds relative to the orientation of Hercules Dome (map). Upper panels are from ERA5 at daily intervals from 2018-2020. Lower panels are from CMIP6 at monthly intervals from 1850-2014.

Chapter 5

SYNTHESIS AND CONCLUSIONS

5.1 Summary

The work presented in this thesis has addressed several topics regarding polar near-surface processes, including firn compaction, firn aquifers, and snow accumulation. This collection of works has important conclusions relevant to the field of glaciology, including the ice-core and ice-sheet mass balance communities.

In Chapter 2, I introduced a novel method into the Community Firn Model. Specifically, I incorporated a layer-thinning scheme into the Community Firn Model to account for horizontal divergence, the first study to account for this process in firn models. I showed that horizontal divergence can reduce air content in the firn (a metric used in ice-sheet mass balance estimates) significantly and account for as much as 16% of the observed surface lowering in some fast-flowing region in West Antarctica. My results show that omitting transient horizontal divergence in estimates of the air content in the firn leads to an overestimation of ice loss in regions of dynamic ice flow, as calculated via altimetry-based methods.

In Chapter 3, I continue research originally began in 2011 on Greenland's perennial firn aquifers. My study was the first to utilize a relatively new method using deep-sounding radar to identify firn aquifers; was the first study to evaluate trends in firn-aquifer extent beyond Helheim Glacier, Greenland; was the first to extend the perennial firn aquifer time series to earlier than 2010; and was the first to assess regional climate model output to quantitatively evaluate climatic effects on the expansion of perennial firn aquifers. My results show that firn aquifers in southeast Greenland show decadal-scale expansion and are driven by decreasing cold content in the firn since the late 1990s and recently increasing high-melt years, which has reduced the firn's ability for refreezing local meltwater. This research informs more understanding of the hydrology and mass balance of the Greenland Ice Sheet, which is integral for assessing the ice sheet's contribution to sea-level rise.

In Chapter 4, I constructed the first spatially resolved snow-accumulation dataset over Hercules Dome using ground-based shallow ice-penetrating radar data collected in the 2019-2020 and 2022-2023 Antarctic field seasons. My main results show significant spatial variability in the snow-accumulation rates across the ice divide at Hercules Dome and show low recent temporal variability. My results suggest that snow-accumulation rates at Hercules Dome are influenced by regional orography and local snow redistribution, and indicate ice-divide stability over the last 420 years.

5.2 Contributions

The work presented in this dissertation provides several contributions to the glaciological community, as I will outline in the follow section.

5.2.1 Layer-thinning in firn-compaction models

I added a layer-thinning scheme to the Community Firn Model (CFM) as part of Chapter 2. My results show that omitting transient horizontal divergence in estimates of the air content in the firn leads to an overestimation of ice loss in regions of dynamic ice flow, as calculated via altimetry-based methods. This has implications for the altimetry community when assessing mass changes in areas of dynamic ice flow, such as at Thwaites and Pine Island Glaciers in West Antarctica. In addition, the CFM has been applied in numerous research groups worldwide, and the layer-thinning component of the model can be useful especially to groups investigating firn compaction in regions of dynamic ice flow.

5.2.2 Decadal-scale firn-aquifer expansion

Chapter 3 is the first study to characterize decadal-scale firn-aquifer expansion, to use depth-sounder data to analyze firn-aquifer extent, and to extend the firn-aquifer time series further back from 2010. My results indicate that firn aquifers in southeast Greenland show decadal-scale expansion and are driven by decreasing cold content in the firn since the late 1990s and recently increasing high-melt years, which has reduced the firn's ability for refreezing local meltwater. As atmospheric warming over Greenland continues, my study suggests that firn-aquifer expansion may continue and that firn aquifers may play an increasing role in the hydrology of the Greenland Ice Sheet.

5.2.3 Snow accumulation variability at Hercules Dome

I derived variability of the snow-accumulation rates at Hercules Dome, Antarctica, the site of a prospective deep ice core that would provide a climate record that would reflect the extent of the West Antarctic Ice Sheet during the last interglacial period 130,000 years ago. My results show significant spatial variability in the snow-accumulation rates across the divide and that snow accumulation is impacted by regional orographic effects and local wind redistribution from storms and prevailing winds that come from the Filchner-Ronne toward the Ross side of Hercules Dome. My results suggest that interpretation of the prospective deep ice core at Hercules Dome should consider the impacts of local spatial variability of snow accumulation on isotope diffusion and firn-densification processes in the region.

BIBLIOGRAPHY

Abram, Nerilie J et al. (2013). “Acceleration of snow melt in an Antarctic Peninsula ice core during the twentieth century”. In: *Nature Geoscience* 6.5, pp. 404–411.

Adolph, AC and MR Albert (2014). “Gas diffusivity and permeability through the firn column at Summit, Greenland: measurements and comparison to microstructural properties”. In: *The Cryosphere.*

Alley, Karen E et al. (2018). “Continent-wide estimates of Antarctic strain rates from Landsat 8-derived velocity grids”. In: *Journal of Glaciology* 64.244, pp. 321–332.

Alley, Richard B and Charles R Bentley (1988). “Ice-core analysis on the Siple Coast of West Antarctica”. In: *Annals of Glaciology* 11, pp. 1–7.

Alley, Richard B and Joan J Fitzpatrick (1999). “Conditions for bubble elongation in cold ice-sheet ice”. In: *Journal of Glaciology* 45.149, pp. 147–153.

Anandakrishnan, Sridhar, Richard B Alley, and ED Waddington (1994). “Sensitivity of the ice-divide position in Greenland to climate change”. In: *Geophysical research letters* 21.6, pp. 441–444.

Anschütz, H et al. (2011). “Variation of accumulation rates over the last eight centuries on the East Antarctic Plateau derived from volcanic signals in ice cores”. In: *Journal of Geophysical Research: Atmospheres* 116.D20.

Arthern, Robert J et al. (2010). “In situ measurements of Antarctic snow compaction compared with predictions of models”. In: *Journal of Geophysical Research: Earth Surface* 115.F3.

Brangers, Isis et al. (2020). “Sentinel-1 detects firn aquifers in the Greenland Ice Sheet”. In: *Geophysical Research Letters* 47.3, e2019GL085192.

Broeke, Michiel R Van den et al. (2016). “On the recent contribution of the Greenland ice sheet to sea level change”. In: *The Cryosphere* 10.5, pp. 1933–1946.

Bromwich, David H et al. (2004). “Modeled Antarctic precipitation. Part I: Spatial and temporal variability”. In: *Journal of Climate* 17.3, pp. 427–447.

Burr, Alexis et al. (2019). “In situ X-ray tomography densification of firn: The role of mechanics and diffusion processes”. In: *Acta Materialia* 167, pp. 210–220.

Cavitte, Marie GP et al. (2022). “From ice core to ground-penetrating radar: representativeness of SMB at three ice rises along the Princess Ragnhild Coast, East Antarctica”. In: *Journal of Glaciology* 68.272, pp. 1221–1233.

Chawla, Nikhilesh and X Deng (2005). “Microstructure and mechanical behavior of porous sintered steels”. In: *Materials Science and Engineering: A* 390.1-2, pp. 98–112.

Christianson, Knut et al. (2014). “Dilatant till facilitates ice-stream flow in northeast Greenland”. In: *Earth and Planetary Science Letters* 401, pp. 57–69.

Christianson, Knut et al. (2015). “Dynamic perennial firn aquifer on an Arctic glacier”. In: *Geophysical Research Letters* 42.5, pp. 1418–1426.

Chu, Winnie, Dustin M Schroeder, and MR Siegfried (2018). “Retrieval of englacial firn aquifer thickness from ice-penetrating radar sounding in Southeastern Greenland”. In: *Geophysical Research Letters* 45.21, pp. 11–770.

Coble, Robert L (1970). “Diffusion models for hot pressing with surface energy and pressure effects as driving forces”. In: *Journal of applied physics* 41.12, pp. 4798–4807.

Corr, Hugh FJ et al. (2002). “Precise measurement of changes in ice-shelf thickness by phase-sensitive radar to determine basal melt rates”. In: *Geophysical Research Letters* 29.8, pp. 73–1.

Crary, AP and R Wilson Charles (1961). “Formation of “blue” glacier ice by horizontal compressive forces”. In: *Journal of Glaciology* 3.30, pp. 1045–1050.

CRESIS (2021a). *AR Data.* dataset. DOI: `10.7283/633E-1497`. URL: `https://data.cresis.ku.edu/`.

CRESIS (2021b). *RDS Data*. dataset. DOI: `10.7283/633E-1497`. URL: `https://data.cresis.ku.edu/`.

Cuffey, Kurt M and William Stanley Bryce Paterson (2010). *The physics of glaciers*. Academic Press.

Culberg, Riley, Dustin M Schroeder, and Winnie Chu (2021). “Extreme melt season ice layers reduce firn permeability across Greenland”. In: *Nature communications* 12.1, pp. 1–9.

Dahl-Jensen, Dorthe et al. (1997). “A search in north Greenland for a new ice-core drill site”. In: *Journal of Glaciology* 43.144, pp. 300–306.

Das, Indrani et al. (2013). “Influence of persistent wind scour on the surface mass balance of Antarctica”. In: *Nature Geoscience* 6.5, pp. 367–371.

Depoorter, Mathieu A et al. (2013). “Calving fluxes and basal melt rates of Antarctic ice shelves”. In: *Nature* 502.7469, p. 89.

Dixon, Daniel et al. (2004). “A 200 year sub-annual record of sulfate in West Antarctica, from 16 ice cores”. In: *Annals of Glaciology* 39, pp. 545–556.

Duddu, Ravindra and Haim Waisman (2012). “A temperature dependent creep damage model for polycrystalline ice”. In: *Mechanics of Materials* 46, pp. 23–41.

Dütsch, Marina et al. (2023). “Response of water isotopes in precipitation to a collapse of the West Antarctic Ice Sheet in high-resolution simulations with the Weather Research and Forecasting Model”. In: *Journal of Climate*, pp. 1–30.

Fausto, Robert S et al. (2018). “A snow density dataset for improving surface boundary conditions in Greenland ice sheet firn modeling”. In: *Frontiers in Earth Science* 6, p. 51.

Fettweis, Xavier and Asa Rennermalm (2020a). “Model simulations from Modèle Atmosphérique Regionale (MAR) over Greenland, 1948-2016”. In: *Nature Geoscience*.

— (2020b). *Model simulations from Modèle Atmosphérique Regionale (MAR) over Greenland, 1948-2016*. dataset. DOI: `doi:10.18739/A2H12V80V`. URL: `https://arcticdata.io/catalog/view/doi%3A10.18739%2FA2TM72225`.

Field et al. (2012). “Managing the Risks of Extreme Events and Disasters to Advance Climate Change Adaptation: Special Report of the Intergovernmental Panel on Climate Change”. In.

Forster, Richard R et al. (2014). “Extensive liquid meltwater storage in firn within the Greenland ice sheet”. In: *Nature Geoscience* 7.2, pp. 95–98.

Fountain, Andrew G (1989). “The storage of water in, and hydraulic characteristics of, the firn of South Cascade Glacier, Washington State, USA”. In: *Annals of Glaciology* 13, pp. 69–75.

Fountain, Andrew G and Joseph S Walder (1998). “Water flow through temperate glaciers”. In: *Reviews of Geophysics* 36.3, pp. 299–328.

Fox-Kemper B., Hewitt H.T. et al. (2021). “Ocean, Cryosphere and Sea Level Change”. In: *Climate Change 2021: The Physical Science Basis. Contribution of Working Group I to the Sixth Assessment Report of the Intergovernmental Panel on Climate Change*, 1211–1362.

Fudge, TJ et al. (2016). “Variable relationship between accumulation and temperature in West Antarctica for the past 31,000 years”. In: *Geophysical Research Letters* 43.8, pp. 3795–3803.

Fudge, TJ et al. (2022). “A site for deep ice coring at West Hercules Dome: results from ground-based geophysics and modeling”. In: *Journal of Glaciology*, pp. 1–13.

Fujita, S et al. (2011). “Spatial and temporal variability of snow accumulation rate on the East Antarctic ice divide between Dome Fuji and EPICA DML”. In: *The Cryosphere* 5.4, pp. 1057–1081.

Fujita, Shuji et al. (2002). “Scattering of VHF radio waves from within the top 700 m of the Antarctic ice sheet and its relation to the depositional environment: a case-study along the Syowa–Mizuho–Dome Fuji traverse”. In: *Annals of Glaciology* 34, pp. 157–164.

Gagliardini, Olivier and Jacques Meyssonnier (1997). “Flow simulation of a firn-covered cold glacier”. In: *Annals of Glaciology* 24, pp. 242–248.

Gardner, Alex S et al. (2013). “A reconciled estimate of glacier contributions to sea level rise: 2003 to 2009”. In: *science* 340.6134, pp. 852–857.

Gascon, Gabrielle et al. (2013). “Changes in accumulation-area firn stratigraphy and meltwater flow during a period of climate warming: Devon Ice Cap, Nunavut, Canada”. In: *Journal of Geophysical Research: Earth Surface* 118.4, pp. 2380–2391.

Gow, Anthony J (1968). “Bubbles and bubble pressures in Antarctic glacier ice”. In: *Journal of Glaciology* 7.50, pp. 167–182.

— (1969). “On the rates of growth of grains and crystals in South Polar firn”. In: *Journal of Glaciology* 8.53, pp. 241–252.

Gregory, SA, MR Albert, and I Baker (2014). “Impact of physical properties and accumulation rate on pore close-off in layered firn”. In: *The Cryosphere* 8, pp. 91–105.

Gutmann, Ethan D et al. (2012). “Snow measurement by GPS interferometric reflectometry: an evaluation at Niwot Ridge, Colorado”. In: *Hydrological Processes* 26.19, pp. 2951–2961.

Hamilton, Gordon S (2002). “Mass balance and accumulation rate across Siple Dome, West Antarctica”. In: *Annals of Glaciology* 35, pp. 102–106.

Herron, Michael M and Chester C Langway (1980). “Firn densification: an empirical model”. In: *Journal of Glaciology* 25.93, pp. 373–385.

Hindmarsh, RGA (1996). “Stochastic perturbation of divide position”. In: *Annals of Glaciology* 23, pp. 94–104.

Hoffman, A., N. Holschuh, and 16 others (in review). “Scars of tectonic extension promote ice-sheet nucleation from Hercules Dome into West Antarctica”. In: *Nature Geoscience*.

Howat I., A. Negrete and B. Smith (2015). *MEaSUREs Greenland Ice Mapping Project (GIMP) Digital Elevation Model, Version 1*. dataset. DOI: `https://nsidc.org/data/nsidc-0645/versions/1`. URL: `https://arcticdata.io/catalog/view/doi%3A10.18739%2FA2TM72225`.

Howat, Ian M et al. (2019). “The Reference Elevation Model of Antarctica”. In: *Cryosphere* 13.2.

Humphrey, Neil F, Joel T Harper, and Toby W Meierbachtol (2021). “Physical limits to meltwater penetration in firn”. In: *Journal of Glaciology* 67.265, pp. 952–960.

Jacobel, Robert W et al. (2005). “Glaciological and climatic significance of Hercules Dome, Antarctica: An optimal site for deep ice core drilling”. In: *Journal of Geophysical Research: Earth Surface* 110.F1.

Jansson, Peter, Regine Hock, and Thomas Schneider (2003). “The concept of glacier storage: a review”. In: *Journal of Hydrology* 282.1-4, pp. 116–129.

Jenkins, Adrian et al. (2006). “Interactions between ice and ocean observed with phase-sensitive radar near an Antarctic ice-shelf grounding line”. In: *Journal of Glaciology* 52.178, pp. 325–346.

Joughin, Ian, Benjamin E Smith, and Brooke Medley (2014). “Marine ice sheet collapse potentially under way for the Thwaites Glacier Basin, West Antarctica”. In: *Science* 344.6185, pp. 735–738.

Joughin, Ian et al. (2012). “Seasonal to decadal scale variations in the surface velocity of Jakobshavn Isbrae, Greenland: Observation and model-based analysis”. In: *Journal of Geophysical Research: Earth Surface* 117.F2.

Karlsson, Nanna B et al. (2020). “Surface accumulation in Northern Central Greenland during the last 300 years”. In: *Annals of Glaciology* 61.81, pp. 214–224.

Kaspari, Susan et al. (2004). “Climate variability in West Antarctica derived from annual accumulation-rate records from ITASE firn/ice cores”. In: *Annals of Glaciology* 39, pp. 585–594.

Keegan, KM et al. (2019). “Climate Effects on Firn Permeability Are Preserved Within a Firn Column”. In: *Journal of Geophysical Research: Earth Surface* 124.3, pp. 830–837.

Killick, Rebecca, Paul Fearnhead, and Idris A Eckley (2012). “Optimal detection of changepoints with a linear computational cost”. In: *Journal of the American Statistical Association* 107.500, pp. 1590–1598.

Killingbeck, SF et al. (2020). “Integrated borehole, radar, and seismic velocity analysis reveals dynamic spatial variations within a firn aquifer in southeast Greenland”. In: *Geophysical Research Letters* 47.18, e2020GL089335.

Kirchner, Joseph F, Charles R Bentley, and James D Robertson (1979). “Lateral density differences from seismic measurements at a site on the Ross Ice Shelf, Antarctica”. In: *Journal of Glaciology* 24.90, pp. 309–312.

Koenig, Lora S et al. (2014). “Initial in situ measurements of perennial meltwater storage in the Greenland firn aquifer”. In: *Geophysical Research Letters* 41.1, pp. 81–85.

Kuipers Munneke, P et al. (2015). “Elevation change of the Greenland Ice Sheet due to surface mass balance and firn processes, 1960-2014”. In: *The Cryosphere* 9.6, pp. 2009–2025.

Larson, Kristine M et al. (2009). “Can we measure snow depth with GPS receivers?” In: *Geophysical Research Letters* 36.17.

Lavielle, Marc (2005). “Using penalized contrasts for the change-point problem”. In: *Signal processing* 85.8, pp. 1501–1510.

Legchenko, Anatoly et al. (2018). “Estimating water volume stored in the south-eastern Greenland firn aquifer using magnetic-resonance soundings”. In: *Journal of Applied Geophysics* 150, pp. 11–20.

Leuschen, C et al. (2014). “UAS-based radar sounding of the polar ice sheets”. In: *IEEE Geoscience and Remote Sensing Magazine* 2.1, pp. 8–17.

Li, Jun and H Jay Zwally (2011). “Modeling of firn compaction for estimating ice-sheet mass change from observed ice-sheet elevation change”. In: *Annals of Glaciology* 52.59, pp. 1–7.

— (2015). “Response times of ice-sheet surface heights to changes in the rate of Antarctic firn compaction caused by accumulation and temperature variations”. In: *Journal of Glaciology* 61.230, pp. 1037–1047.

Ligtenberg, SRM, MM Helsen, and MR Van den Broeke (2011). “An improved semi-empirical model for the densification of Antarctic firn”. In: *The Cryosphere* 5, pp. 809–819.

Lilien, David A et al. (2020). “ImpDAR: an open-source impulse radar processor”. In: *Annals of Glaciology* 61.81, pp. 114–123.

Lundin, Jessica MD et al. (2017). “Firn Model Intercomparison Experiment (FirnMICE)”. In: *Journal of Glaciology* 63.239, pp. 401–422.

Lüthi, M and M Funk (2000). “Dating ice cores from a high Alpine glacier with a flow model for cold firn”. In: *Annals of Glaciology* 31, pp. 69–79.

Machguth, Horst et al. (2016). “Greenland meltwater storage in firn limited by near-surface ice formation”. In: *Nature Climate Change* 6.4, pp. 390–393.

Maeno, Norikazu and Takao Ebinuma (1983). “Pressure sintering of ice and its implication to the densification of snow at polar glaciers and ice sheets”. In: *The Journal of Physical Chemistry* 87.21, pp. 4103–4110.

McMillan, Malcolm et al. (2016). “A high-resolution record of Greenland mass balance”. In: *Geophysical Research Letters* 43.13, pp. 7002–7010.

Medley, Brooke et al. (2013). “Airborne-radar and ice-core observations of annual snow accumulation over Thwaites Glacier, West Antarctica confirm the spatiotemporal variability of global and regional atmospheric models”. In: *Geophysical Research Letters* 40.14, pp. 3649–3654.

Miege, Clement et al. (2013). “Southeast Greenland high accumulation rates derived from firn cores and ground-penetrating radar”. In: *Annals of Glaciology* 54.63, pp. 322–332.

Miège, Clément et al. (2016). “Spatial extent and temporal variability of Greenland firn aquifers detected by ground and airborne radars”. In: *Journal of Geophysical Research: Earth Surface* 121.12, pp. 2381–2398.

Miller, Olivia et al. (2020). “Hydrology of a perennial firn aquifer in Southeast Greenland: an overview driven by field data”. In: *Water Resources Research* 56.8, e2019WR026348.

Miège, Clément (2018). *Spatial extent of Greenland firn aquifer detected by airborne radars, 2010-2017*. dataset. DOI: `10.18739/A2TM72225`. URL: `https://arcticdata.io/catalog/view/doi%3A10.18739%2FA2TM72225`.

Montgomery, Lynn et al. (2020). “Hydrologic properties of a highly permeable firn aquifer in the Wilkins Ice Shelf, Antarctica”. In: *Geophysical Research Letters* 47.22, e2020GL089552.

Morris, EM and DJ Wingham (2014). “Densification of polar snow: Measurements, modeling, and implications for altimetry”. In: *Journal of Geophysical Research: Earth Surface* 119.2, pp. 349–365.

Morris, EM et al. (2017). “Snow densification and recent accumulation along the iSTAR traverse, Pine Island Glacier, Antarctica”. In: *Journal of Geophysical Research: Earth Surface* 122.12, pp. 2284–2301.

Mouginot, J, E Rignot, and B Scheuchl (2014). “Sustained increase in ice discharge from the Amundsen Sea Embayment, West Antarctica, from 1973 to 2013”. In: *Geophysical Research Letters* 41.5, pp. 1576–1584.

— (2019a). “Continent-Wide, Interferometric SAR Phase, Mapping of Antarctic Ice Velocity”. In: *Geophysical Research Letters* 46.16, pp. 9710–9718.

Mouginot, Jeremie et al. (2017). “Comprehensive annual ice sheet velocity mapping using Landsat-8, Sentinel-1, and RADARSAT-2 data”. In: *Remote Sensing* 9.4, p. 364.

Mouginot, Jérémie et al. (2019b). “Forty-six years of Greenland Ice Sheet mass balance from 1972 to 2018”. In: *Proceedings of the national academy of sciences* 116.19, pp. 9239–9244.

Müller, Karsten et al. (2010). “An 860 km surface mass-balance profile on the East Antarctic plateau derived by GPR”. In: *Annals of Glaciology* 51.55, pp. 1–8.

Munneke, P Kuipers et al. (2014). “Explaining the presence of perennial liquid water bodies in the firn of the Greenland Ice Sheet”. In: *Geophysical Research Letters* 41.2, pp. 476–483.

Munneke, Peter Kuipers et al. (2015). “A model study of the response of dry and wet firn to climate change”. In: *Annals of Glaciology* 56.70, pp. 1–8.

Muñoz-Sabater (2019a). “ERA5-Land hourly data from 1950 to present.” In: *Copernicus Climate Change Service (C3S)* 13.9, pp. 4349–4383.

— (2019b). “ERA5-Land monthly averaged data from 1950 to present”. In: *Copernicus Climate Change Service (C3S)* 13.9, pp. 4349–4383.

Nghiem, SV et al. (2012). “The extreme melt across the Greenland ice sheet in 2012”. In: *Geophysical Research Letters* 39.20.

Nicholls, Keith W et al. (2015). “A ground-based radar for measuring vertical strain rates and time-varying basal melt rates in ice sheets and shelves”. In: *Journal of Glaciology* 61.230, pp. 1079–1087.

Ochwat, Naomi E et al. (2021). “Evolution of the firn pack of Kaskawulsh Glacier, Yukon: meltwater effects, densification, and the development of a perennial firn aquifer”. In: *The Cryosphere* 15.4.

Oerter, Hans and W Rauert (1982). “Core drilling on Vernagtferner (Oetztal Alps, Austria) in 1979: tritium contents”. In: *Zeitschrift für Gletscherkunde und Glazialgeologie* 1, pp. 13–22.

Poinar, Kristin, Christine F Dow, and Lauren C Andrews (2019). “Long-term support of an active subglacial hydrologic system in Southeast Greenland by firn aquifers”. In: *Geophysical Research Letters* 46.9, pp. 4772–4781.

Poinar, Kristin et al. (2017). “Drainage of Southeast Greenland firn aquifer water through crevasses to the bed”. In: *Frontiers in Earth Science* 5, p. 5.

Reeh, Niels et al. (2005). “An empirical firn-densification model comprising ice lenses”. In: *Annals of Glaciology* 42, pp. 101–106.

Richardson, Cecilia et al. (1997). “Spatial distribution of snow in western Dronning Maud Land, East Antarctica, mapped by a ground-based snow radar”. In: *Journal of Geophysical Research: Solid Earth* 102.B9, pp. 20343–20353.

Rignot, Eric et al. (2014). “Widespread, rapid grounding line retreat of Pine Island, Thwaites, Smith, and Kohler glaciers, West Antarctica, from 1992 to 2011”. In: *Geophysical Research Letters* 41.10, pp. 3502–3509.

Riverman, KL et al. (2019). “Enhanced Firn Densification in High-Accumulation Shear Margins of the NE Greenland Ice Stream”. In: *Journal of Geophysical Research: Earth Surface* 124.2, pp. 365–382.

Robin, G d Q (1958). “Seismic shooting and related investigations, Glaciology III”. In: *Norwegian-British-Swedish Antarctic Expedition, 1949–52, scientific results*, p. 5.

Rodriguez-Morales, Fernando et al. (2013). “Advanced multifrequency radar instrumentation for polar research”. In: *IEEE Transactions on Geoscience and Remote Sensing* 52.5, pp. 2824–2842.

Roe, Gerard H (2005). “Orographic precipitation”. In: *Annu. Rev. Earth Planet. Sci.* 33, pp. 645–671.

Samimi, Samira et al. (2021). “Time-Domain Reflectometry Measurements and Modeling of Firn Meltwater Infiltration at DYE-2, Greenland”. In: *Journal of Geophysical Research: Earth Surface* 126.10, e2021JF006295.

Schneider, Thomas (1999). “Water movement in the firn of Storglaciären, Sweden”. In: *Journal of Glaciology* 45.150, pp. 286–294.

Schröder, Ludwig et al. (2019). “Four decades of Antarctic surface elevation changes from multi-mission satellite altimetry”. In: *The Cryosphere* 13.2, pp. 427–449.

Shang, Xinyi et al. (2022). “Decadal Changes in Greenland Ice Sheet Firn Aquifers from Radar Scatterometer”. In: *Remote Sensing* 14.9, p. 2134.

Shepherd, Andrew et al. (2012). “A reconciled estimate of ice-sheet mass balance”. In: *Science* 338.6111, pp. 1183–1189.

Shepherd, Andrew et al. (2019). “Trends in Antarctic Ice Sheet elevation and mass”. In: *Geophysical Research Letters* 46.14, pp. 8174–8183.

Shepherd, Andrew et al. (2020). “Mass balance of the Greenland Ice Sheet from 1992 to 2018”. In: *Nature* 579.7798, pp. 233–239.

Smith, Ben et al. (2020). “Pervasive ice sheet mass loss reflects competing ocean and atmosphere processes”. In: *Science.*

Steger, Christian R et al. (2017). “Firn meltwater retention on the Greenland ice sheet: A model comparison”. In: *Frontiers in earth science* 5, p. 3.

Steig, Eric J et al. (2005). “High-resolution ice cores from US ITASE (West Antarctica): development and validation of chronologies and determination of precision and accuracy”. In: *Annals of Glaciology* 41, pp. 77–84.

Steig, Eric J et al. (2015). “Influence of West Antarctic ice sheet collapse on Antarctic surface climate”. In: *Geophysical Research Letters* 42.12, pp. 4862–4868.

Stenni, Barbara et al. (1999). “200 years of isotope and chemical records in a firn core from Hercules Neve, northern Victoria Land, Antarctica”. In: *Annals of Glaciology* 29, pp. 106–112.

Stenni, Barbara et al. (2002). “Eight centuries of volcanic signal and climate change at Talos Dome (East Antarctica)”. In: *Journal of Geophysical Research: Atmospheres* 107.D9, ACL–3.

Stevens, C Max et al. (2020). “The Community Firn Model (CFM) v1. 0”. In: *Geoscientific Model Development Discussions*, pp. 1–37.

Thomas, Elizabeth R, Gareth J Marshall, and Joseph R McConnell (2008). “A doubling in snow accumulation in the western Antarctic Peninsula since 1850”. In: *Geophysical research letters* 35.1.

Turner, John et al. (2014). “Antarctic climate change and the environment: an update”. In: *Polar record* 50.3, pp. 237–259.

Urbini, Stefano et al. (2008). “Historical behaviour of Dome C and Talos Dome (East Antarctica) as investigated by snow accumulation and ice velocity measurements”. In: *Global and Planetary Change* 60.3-4, pp. 576–588.

Vallelonga, P et al. (2014). “Initial results from geophysical surveys and shallow coring of the Northeast Greenland Ice Stream (NEGIS)”. In: *The Cryosphere* 8.4, pp. 1275–1287.

Van Liefferinge, Brice et al. (2021). “Surface Mass Balance Controlled by Local Surface Slope in Inland Antarctica: Implications for Ice-Sheet Mass Balance and Oldest Ice Delineation in Dome Fuji”. In: *Geophysical research letters* 48.24, e2021GL094966.

Van Wessem, Jan Melchior et al. (2018). “Modelling the climate and surface mass balance of polar ice sheets using RACMO2: Part 2: Antarctica (1979-2016)”. In: *Cryosphere* 12.4, pp. 1479–1498.

Van Wessem, JM et al. (2016). “The modelled surface mass balance of the Antarctic Peninsula at 5.5 km horizontal resolution”. In: *The Cryosphere* 10.1, pp. 271–285.

Vandecrux, Baptiste et al. (2020). “The firn meltwater Retention Model Intercomparison Project (RetMIP): evaluation of nine firn models at four weather station sites on the Greenland ice sheet”. In: *The Cryosphere* 14.11, pp. 3785–3810.

Wessem, J Melchior van et al. (2021). “An exploratory modelling study of perennial firn aquifers in the Antarctic Peninsula for the period 1979–2016”. In: *The Cryosphere* 15.2, pp. 695–714.

Wingham, Duncan J et al. (1998). “Antarctic elevation change from 1992 to 1996”. In: *Science* 282.5388, pp. 456–458.

Yasoichi ENDO, Kenzo et al. (1973). “Characteristics of the snow cover in East Antarctica along the route of the JARE South Pole traverse and factors controlling such characteristics”. In: *JARE scientific reports. Ser. C, Earth sciences* 7, pp. 1–38.

Zumberge, JH (1960). “Deformation of the Ross Ice Shelf near the Bay of Whales, Antarctica”. In: *IGY Glaciological Report Series (New York, IGY World Data Center A, Glaciology, American Geographical Society*, p. 3.

APPENDIX A. SUPPLEMENTARY MATERIALS TO CHAPTER 2

A.1 The Community Firn Model and the layer-thinning scheme in detail

The Community Firn Model (CFM; Stevens and others, 2020) simulates the evolution of firn properties in a modular one-dimensional Lagrangian framework. Users specify the surface-boundary conditions (accumulation rate, temperature, and/or surface-snow density), firn-densification physics, time step, and thickness of the model domain to use. The CFM runs by first spinning up the specified model to steady state to create an initial condition for the primary model run. The spin-up must have sufficient duration to evolve the firn-column properties to reset the entire domain. The Lagrangian domain consists of a fixed number of parcels representing layers of firn. Parcels are added at the ice-sheet surface and removed at depth once the parcels reach ice density. After spinning up, the CFM evolves the firn column in response to the varying boundary conditions.

The Lagrangian vertical strain rate $\dot{\varepsilon}_{zz}$ in the firn is generally related to the Lagrangian densification rate through:

$$\dot{\varepsilon}_{zz} = -\frac{1}{\rho}\frac{D\rho}{Dt} \tag{S1}$$

where ρ is the firn density, t is time, and z is the depth. Most firn-compaction models employ a form of the compaction equation that solves for the Lagrangian rate of change of density $\frac{D\rho}{Dt}$:

$$\frac{D\rho}{Dt} = c(\rho_i - \rho) \tag{S2}$$

where t is time and c is a coefficient that is usually calibrated to fit the model results to depth-density profiles, which are assumed to be in steady-state. These coefficients are broadly speaking representative of physical firn-densification mechanisms (Lundin and others, 2017; Stevens and others, 2020). In a steady-state firn column, the model form of Equation S2 is compatible with the suggestion by Robin (1958) that the fractional change in porosity with depth, and therefore change of density with depth, is proportional to the increment of additional overburden load. This was originally expressed as:

$$\frac{D\rho}{Dz} = \beta g \rho(\rho_i - \rho) \tag{S3}$$

where β is a constant and g is gravity. The CFM solves density evolution $\frac{d\rho}{dt}$ explicitly (Equation 2 in Stevens and others (2020)) through:

$$\rho_{new} = \rho_{old} + \left(\frac{d\rho}{dt}\right) dt. \tag{S4}$$

We next show how firn-parcel thickness λ relates to firn density ρ. We can express changes in λ due to the vertical strain rate (i.e., due to a traditional firn-compaction model) as:

$$\lambda_{part1} = \lambda_{old}(1 + \dot{\varepsilon}_{zz}\Delta t). \tag{S4}$$

Alternatively, this can be expressed in terms of density changes and the derivative $\frac{D\rho}{Dt}$ that most firn-compaction models solve for:

$$\lambda_{part1} = \lambda_{old}\left(1 - \left(\frac{1}{\rho}\frac{D\rho}{Dt}\right)\Delta t\right) \tag{S5}$$

which can then be expressed using Equation S2:

$$\lambda_{part1} = \lambda_{old} - \lambda_{old}c\Delta t(\rho_i - \rho). \tag{S6}$$

In the layer-thinning scheme, the firn parcels are further thinned due to stretching from a prescribed rate of horizontal divergence $\dot{\varepsilon}_h$:

$$\lambda_{part2} = \lambda_{part1}(1 + \dot{\varepsilon}_h\Delta t). \tag{S7}$$

The resulting thinned parcel thickness λ_{total} of the firn parcels during a single time step using the layer-thinning scheme can be expressed as:

$$\lambda_{total} = \lambda_{old} - \lambda_{old}c\Delta t(\rho_i - \rho)(1 + \dot{\varepsilon}_h\Delta t) = \lambda_{old} - (\lambda_{old}c(\rho_i - \rho) + \lambda_{old}c\dot{\varepsilon}_h\Delta t)\Delta t \tag{S8}$$

where the selected firn-compaction model (e.g., Herron and Langway (1980); Ligtenberg and others, 2011) solves for the vertical strain rate given by the general form $c\left(\frac{\rho_i - \rho}{\rho}\right)$, and the rate of horizontal divergence $\dot{\varepsilon}_h$is a specified condition in the CFM. Equation S8 implements a continuity assumption, i.e., $\dot{\varepsilon}_h = \dot{\varepsilon}_{zz}$.

A.2 Notes on Morris and others (2017) approach to thinning

Morris and others (2017) consider horizontal divergence in their estimation of the density-corrected vertical strain rate F_Z, by subtracting a correction to the density-corrected volumetric strain rate without horizontal divergence $F(\rho)$ in terms of the mean density ρ_m over time Δt, ice density ρ_i, and horizontal divergence $\dot{\varepsilon}_h$ (Equation 19 of Morris and others (2017)):

$$F_Z(\rho) \approx F(\rho) - \left(\frac{\rho_m}{\rho_i - \rho_m}\right)\dot{\varepsilon}_h \tag{S9}$$

where horizontal divergence is estimated from neutron probe firn data determined through (Equation 18 of Morris and others (2017)):

$$q_i(i) \approx (1 + \dot{\varepsilon}_H\Delta t)q_2(i) \tag{S10}$$

where $q_i(i)$ is the initial water-equivalent height in the firn column, which moves to water-equivalent height $q_2(i)$ after time step Δt. Equation S10 is equivalent to Equation S7, where q represents water-equivalent height instead of thickness λ of the firn parcel.

A.3 Differences between the Herron and Langway (1980) and Ligtenberg and others (2011) firn-compaction models

The Herron and Langway (1980) firn-compaction model (HL) assumes that firn compaction is dependent on two commonly measured variables: mean annual accumulation rate, and mean annual surface temperature. HL used Sorge's Law (Bader, 1954) and depth-density profiles from seven sites in Greenland and ten sites in Antarctica to derive their model. Sorge's Law is the steady-state relation:

$$v(z) = \frac{\dot{b}}{\rho(z)} \qquad \text{(S11)}$$

where $v(z)$ is the vertical velocity of a parcel of firn and $\dot{b}$ is the accumulation rate. Equation S11 can be differentiated with respect to depth to allow the vertical strain rate to be estimated from a depth-density profile:

$$\dot{\varepsilon}_{zz} = \frac{\partial v}{\partial z} \approx \frac{\partial \rho}{\partial z}\frac{\dot{b}}{\rho^2} \qquad \text{(S12)}$$

HL empirical solution for stages 1 and 2 of the firn column, respectively, is:

$$\frac{D\rho}{Dt} = k_0 A^a(\rho_i - \rho), \qquad \rho < 550\ kg\ m^{-3} \qquad \text{(S13)}$$

$$\frac{D\rho}{Dt} = k_1 A^b(\rho_i - \rho), \qquad 550\ kg\ m^{-3} < \rho < 800\ kg\ m^{-3} \qquad \text{(S14)}$$

where A is the accumulation rate; the accumulation constants $a = 1.1 \pm 0.2$ and $b = 0.5 \pm 0.2$; and the Arrhenius-type rate constants are:

$$k_0 = 11exp\left[-\frac{10160}{RT}\right] \qquad \text{(S15)}$$

$$k_1 = 575exp\left[-\frac{21400}{RT}\right]. \qquad \text{(S16)}$$

The Ligtenberg and others (2011) firn-compaction model (LIG) is based on the steady-state version of the Arthern and others (2010) model (ART-S). ART-S is based on the form of HL, but uses vertical strain rate data from three sites in Antarctica, instead of depth-density data and Sorge's Law, to derive its coefficients. LIG added a tuning coefficient to adjust the accumulation dependence in ART-S to expand applicability to more sites on the ice sheets. LIG solves the equations:

$$\frac{D\rho}{Dt} = M_0 C_0 F \dot{b} g(\rho_i - \rho), \qquad \rho < 550\ kg\ m^{-3} \qquad \text{(S17)}$$

$$\frac{D\rho}{Dt} = M_1 C_1 F \dot{b} g(\rho_i - \rho), \qquad 550\ kg\ m^{-3} < \rho < 800\ kg\ m^{-3} \qquad \text{(S18)}$$

where g is gravitation acceleration, $\dot{b}$ is the average annual accumulation rate, $M_0 = 1.435 - 0.151ln(\dot{b})$ and $M_1 = 2.366 - 0.293ln(\dot{b})$; the constants are $C_0 = 0.03$ and $C_1 = 0.07$; and the Arrhenius-type rate constants are:

$$F = exp\left[-\frac{E_C}{RT} + \frac{E_g}{RT}\right] \qquad \text{(S19)}$$

where R is the ideal gas constant, T is temperature, $E_C = 60\ kJ\ mol^{-1}$, and $E_g = 42.4\ kJ\ mol^{-1}$.

A.4 Estimates of firn-air content in mass-change estimates

FAC changes in time (ΔFAC) are important for altimetry studies of ice-sheet mass balance in order to determine changes in mass Δm from observed changes ice-sheet surface elevation Δh_{obs}. Model estimates of ΔFAC can be subtracted from the time series of total surface-elevation change h to produce a time series of ice-equivalent thickness change (Shepherd and others, 2012; Depoorter and others, 2013; Shepherd and others, 2019). The mass of the ice column can be described in terms of observed column volume (thickness h_{obs}, area A, FAC, and density ρ_i):

$$m = h_{obs} - (FAC)\rho_i A. \tag{S20}$$

We are interested in Δm, which is defined as the difference between the mass evaluated at the current time m^k and the mass evaluated at a previous time m^{k-1}:

$$\Delta m = m^k - m^{k-1}. \tag{S21}$$

Similarly, ΔFAC is the difference between the FAC evaluated at a more current time $FAC^{\,k}$ and the FAC evaluated at a previous time FAC^{k-1}. Then, the change in mass can be expressed in terms of the ΔFAC:

$$m^k - m^{k-1} = \left(h_{obs}^k - (FAC^k)\right)\rho_i A - \left(h_{obs}^{k-1} - (FAC^{k-1})\right)\rho_i A \tag{S22}$$

$$\Delta m = (\Delta h - \Delta FAC)\rho_i A. \tag{S23}$$

As we determine the impact of horizontal divergence on FAC, Equation S23 allows us to assess its impact on the calculated change in mass from a change in elevation.

A.5 Herron and Langway (1980) results

Figures 5-7 in the main text show the results of LIG. Below, we show the results from the same runs using HL.

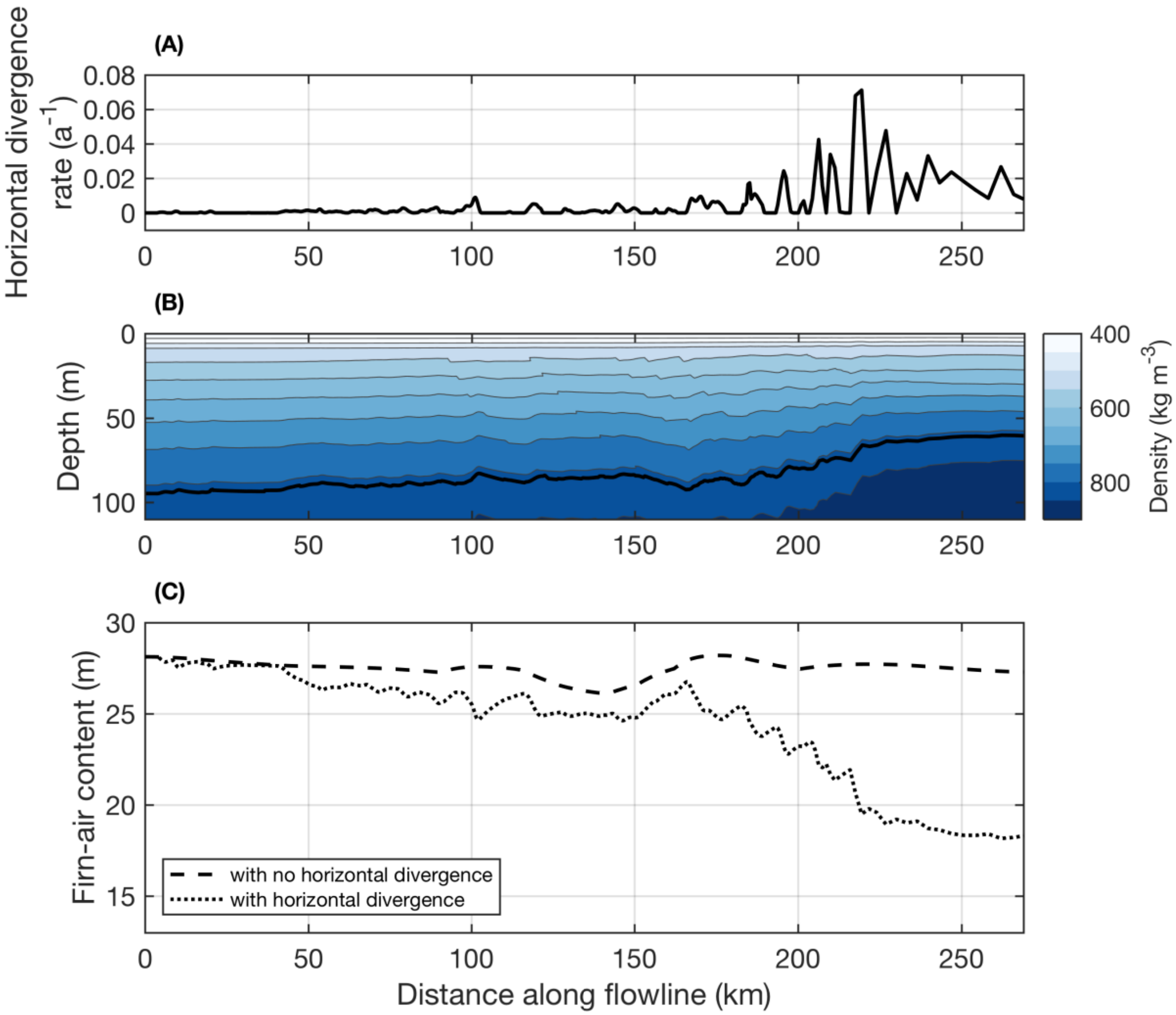

Figure A1. Results from the layer-thinning scheme for the flowline on Thwaites Glacier using the Herron and Langway (1980) firn-compaction model (Experiment 2). (A) Horizontal divergence rates for the flowline. Horizontal divergence rates were derived from Mouginot and others (2019) following the approach of Alley and others (2018), and exclude compression. (B) The firn depth-density profiles along the flowline for the model that accounts for horizontal divergence. Black line indicates bubble close-off (BCO) depth (i.e., density of 830 kg m^{-3}). Contour interval is 50 kg m^{-3}. (C) FAC results from model runs including the horizontal divergence rates shown in (A) (dotted line) and from a model without the horizontal divergence rates (dashed line).

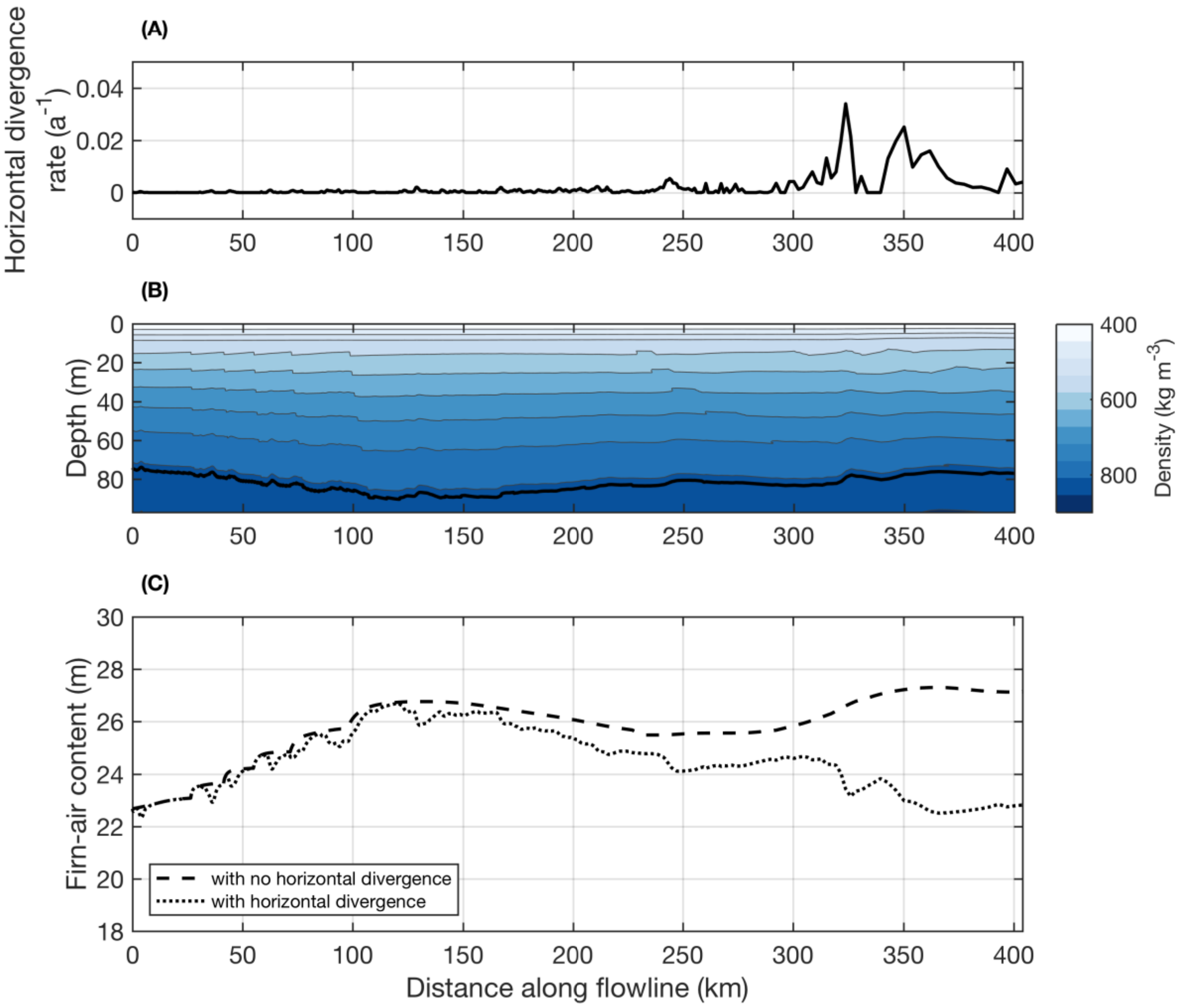

Figure A2. Results from the layer-thinning scheme for a flowline on Pine Island Glacier using the Herron and Langway (1980) firn-compaction model (Experiment 3). (A) Horizontal divergence rates for the flowline. Horizontal divergence rates were derived from Mouginot and others (2019) following the approach of Alley and others (2018), and exclude compression. (B) The firn depth-density profiles along the flowline for the model that accounts for horizontal divergence. Black line indicates bubble close-off (BCO) depth (i.e., density of 830 kg m^{-3}). Contour interval is 50 kg m^{-3}. (C) FAC results from model runs with the horizontal divergence rates shown in (A) (dotted line) and from a model without horizontal divergence rates (dashed line).

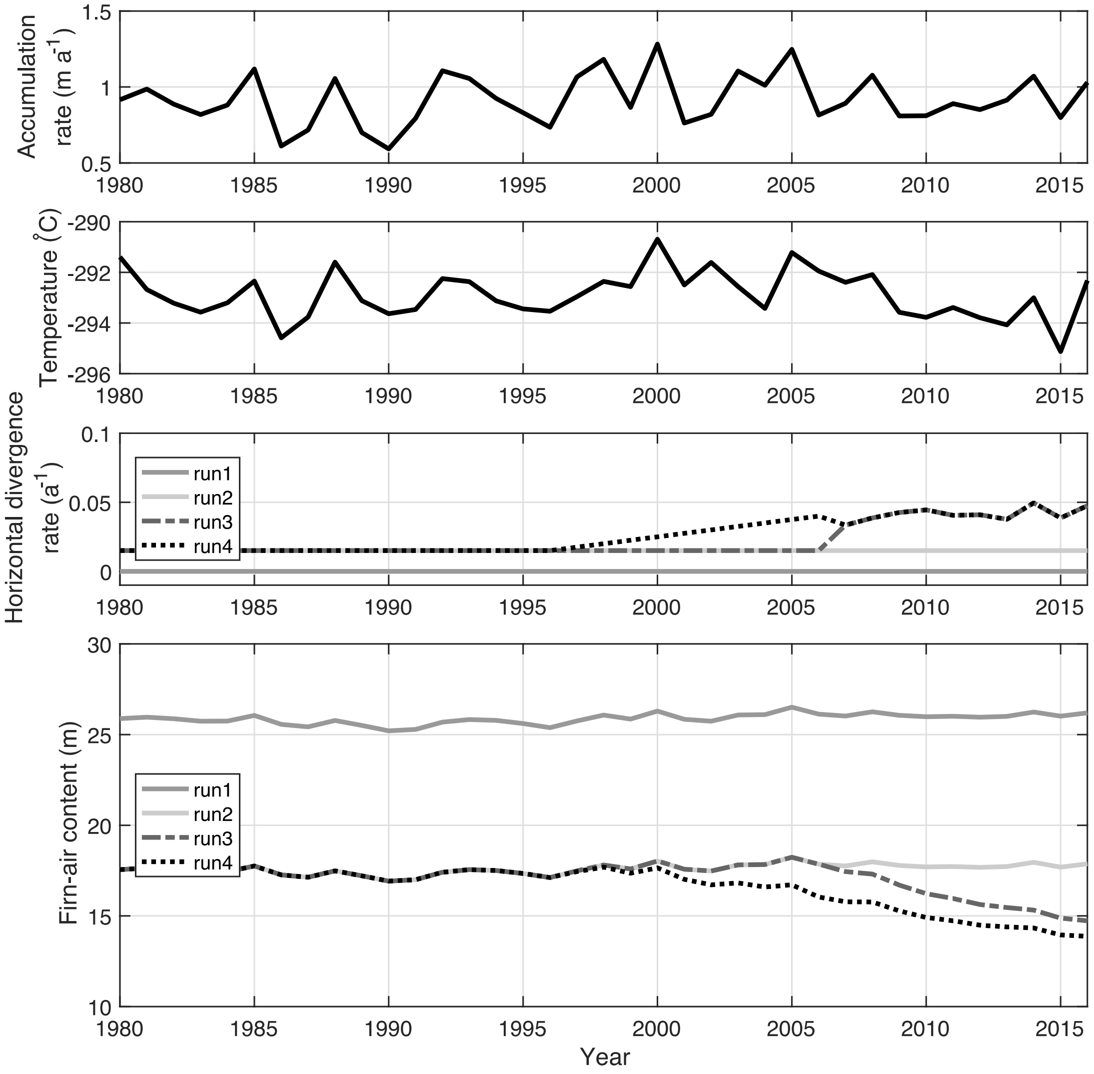

Figure A3. Surface boundary conditions, horizontal divergence rates, and estimated FAC using the layer-thinning scheme with the Herron and Langway (1980) firn-compaction model for a location on lower Thwaites Glacier (Experiment 4). A portion of the model spin up is shown from 1980 to 2007. Run 1 represents a conventional firn-compaction model run with no horizontal divergence. A constant horizontal divergence rate of 0.015 a^{-1} is used in run 2. For runs 3 and 4, after spin up with a constant divergence rate of 0.015 a^{-1}, the model is run from 2007 to 2016 with temporally variable horizontal divergence rates derived from the Mouginot and others (2017) velocity time series. Run 4 includes a linear ramp between horizontal divergence rates from the 1997 to 2007 values.

APPENDIX B. SUPPLEMENTARY MATERIALS TO CHAPTER 3

Contents of This File

(1) Text S1 to S7

(2) Figures B1 to B9

B1. Introduction

This supporting information provides additional details on the radar methods and on the climate reanalysis time series analyzed for the four firn aquifer sites presented in the main manuscript. Sections B1-B4 provide more details on the radar methods and analysis of the firn aquifers via the CReSIS radar depth sounder data. Section B5 shows the repeat flight lines at each firn aquifer. Section B6 provides details on the change point calculation used on the climate reanalysis data. Section B7 shows analysis of parameters from MAR reanalysis data that are not shown in the main manuscript.

B2. Examples of RDS profiles with a contemporaneous AR profile

We first show two examples of contemporaneous CReSIS radar depth sounder (RDS) and accumulation radar (AR) profiles along a repeat flight line to illustrate the appearance of the firn aquifer in both data (Figures B1 and B2). The water table of the firn aquifer is the bright continuous reflector in the AR profiles which correlates with the disappearance of the bed reflector in the RDS profiles.

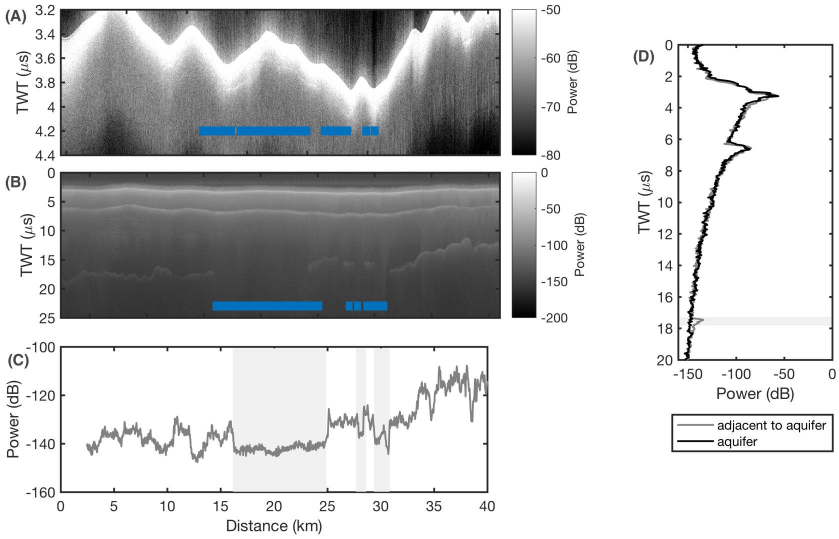

Figure B1. (A) AR data for Helheim 1 in 2013. (B) RDS data for Helheim 1 in 2013. (C) Power along the bed in the RDS data. (D) Traces selected within and outside of the aquifer region showing the lack of bed return in the aquifer in the RDS data. We choose to show this example to show the generally excellent agreement between the identification of the aquifer in the AR and RDS data.

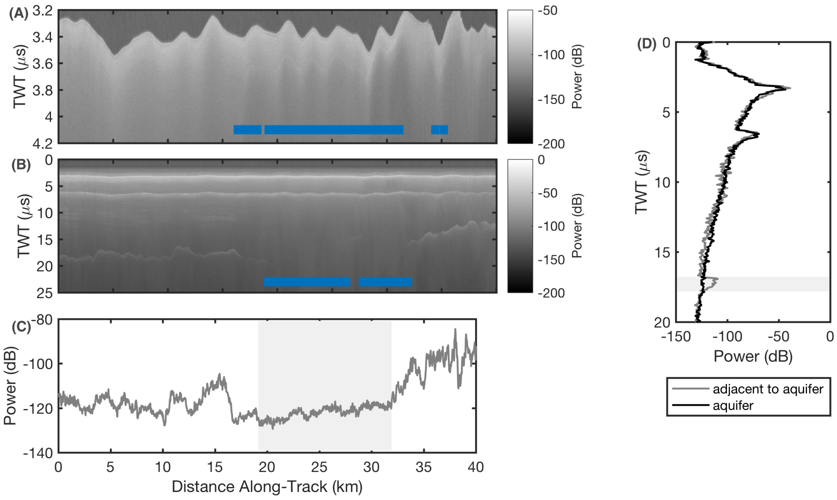

Figure B2. (A) AR data for Helheim 1 in 2012. (B) RDS data for Helheim 1 in 2012. (C) Power along the bed in the RDS data. (D) Traces selected within and outside of the aquifer region showing the lack of bed return in the aquifer in the RDS data. We choose this example to show that some slight disagreement between identification of the aquifer in the RDS and AR radar data is possible at the edges of the aquifer.

The power at the bed drops considerably (up to approximately 10 to 20 dB) at the main portion of the aquifer for a sustained distance (Figures B1C-D, B2C-D). There is not a distinct transition in and out of the main aquifer because, in reality, the distinction between the firn aquifer itself and surrounding dry firn is likely to be gradual and not spatially instantaneous (see section B4). Most disagreement between the different radar data occurs at the edges of the aquifer for this reason. We analyze individual traces (e.g., Figures B3-B6) to determine the location of the bed disappearance in the RDS profiles. While this disagreement is relatively low in all profiles, the aquifer identification within RDS data appears to underestimate the firn aquifer extent relative to the AR data when there is disagreement.

B3. Examples RDS profiles without a contemporaneous AR profile

Here, we show selected RDS profiles and highlight several repeat flight lines that do not have contemporaneous AR profiles (Figures B3-B6). We show two sets of profiles that illustrate the first appearance of the firn aquifers:(1) from H1, which distinctly shows a continuous bed reflector in 1993 and the appearance of the aquifer in 1998 (Figures B3-B4); and (2) from H4, which distinctly shows a continuous bed reflector in 1998 and shows the appearance of the firn aquifer in 2001 (Figures B5-B6).

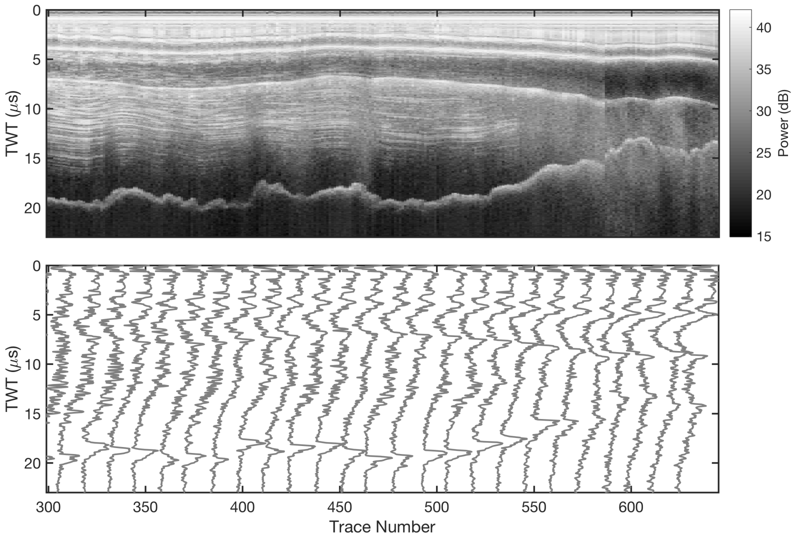

Figure B3. RDS profile at H1 in 1993. While the bed power can vary, the bed reflector is present through the entire profile, as distinctly shown by the single traces.

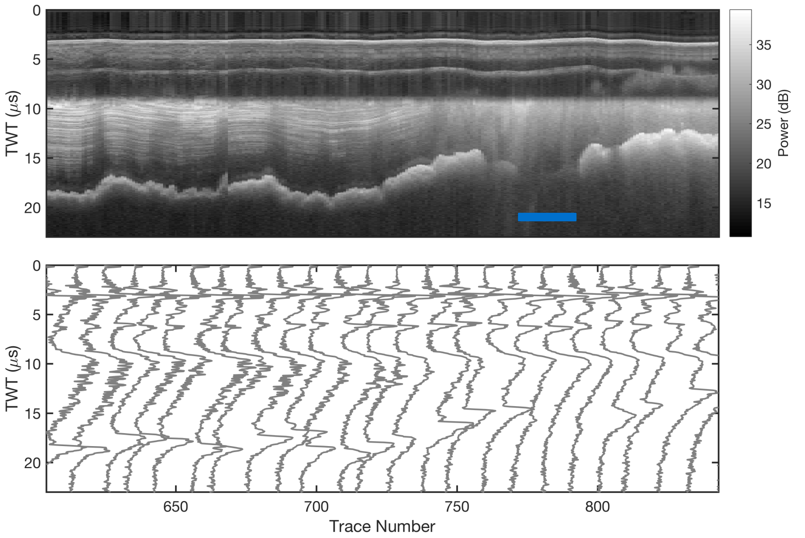

Figure B4. RDS profile at H1 in 1998. The bed reflector vanishes just after trace number 760 and corresponds to the aquifer pick shown.

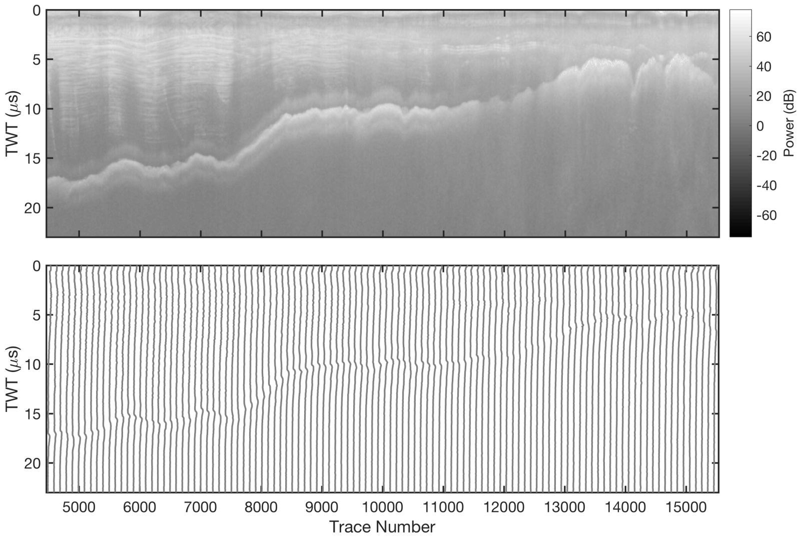

Figure B5. RDS profile at H4 in 1998. The single traces are plotted at small interval to show the features more clearly. While the bed power can vary, the bed reflector is present through the entire profile, as distinctly shown by the single traces.

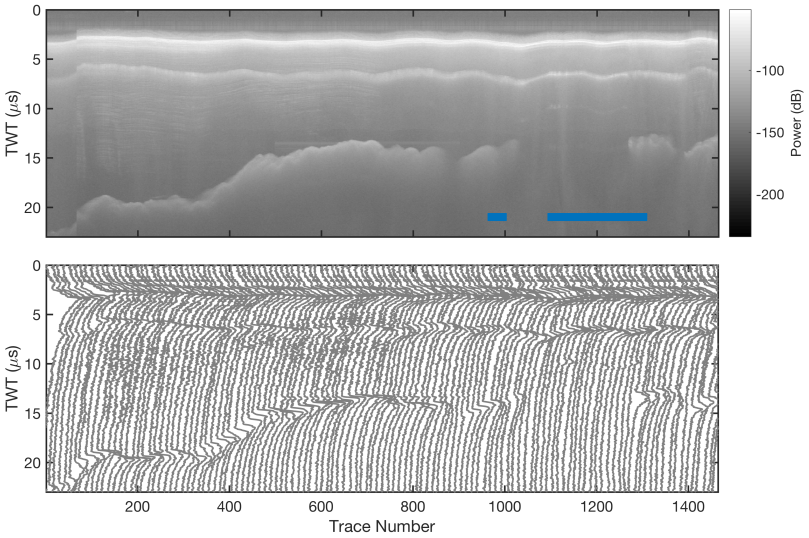

Figure B6. RDS profile at H4 in 2001. The bed reflector vanishes just after trace number 1000 and corresponds to the aquifer pick shown.

B4. Magnetic Resonance Data

Low water volumes from magnetic resonance soundings at H1 (Legchenko et al., 2018) correlate well with the bed reflector observed in the RDS data (Figure S 8). Previous analysis also showed agreement between the water volumes and ground-penetrating radar data (Legchenko et al., 2018). Relatively low water volumes (<500 kg m^{-2}) from 25-27 km and 29-30 km along the flight line correlate with the reappearance of the bed reflector, whereas relatively high water volumes (>500 kg m^{-2}) correlate well with the aquifer.

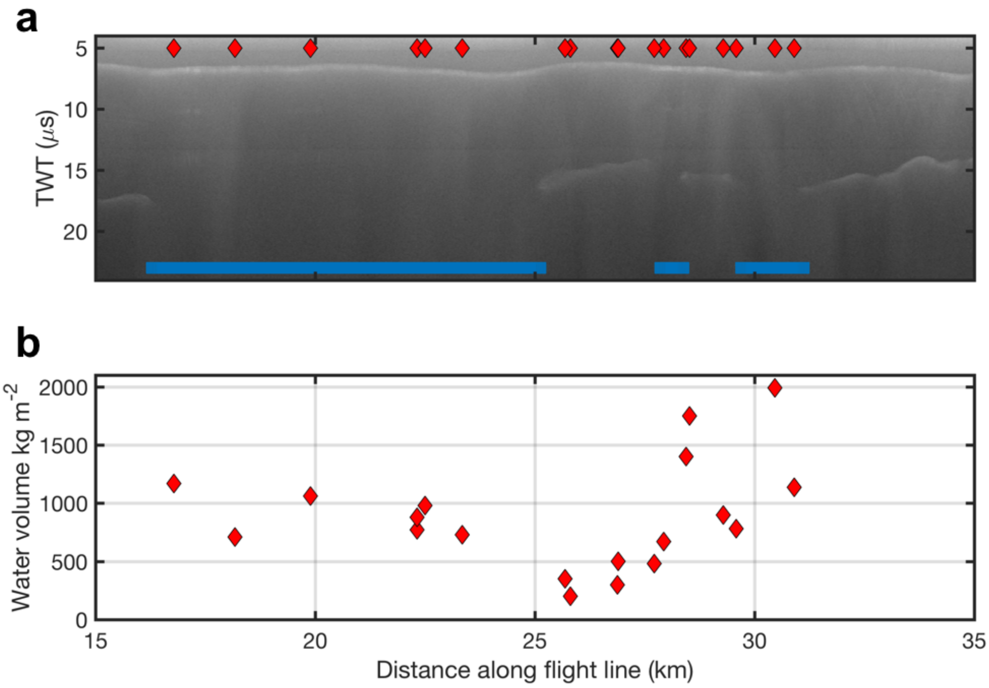

Figure B7. a) RDS profile at H1 in 2014 showing the extent of the firn aquifer (blue) and the location of the magnetic resonance measurements (red). b) Water volumes derived from the magnetic resonance measurements, taken in 2015 and 2016. Note that the nearest RDS profile in time is in 2014.

B5. Repeat Flight Lines at Each Aquifer Site

The repeat flight lines extend approximately over the same location each year, however, there are minor deviations. As such, we project the aquifer extent along the flight line to a common linear trajectory (Figure S8).

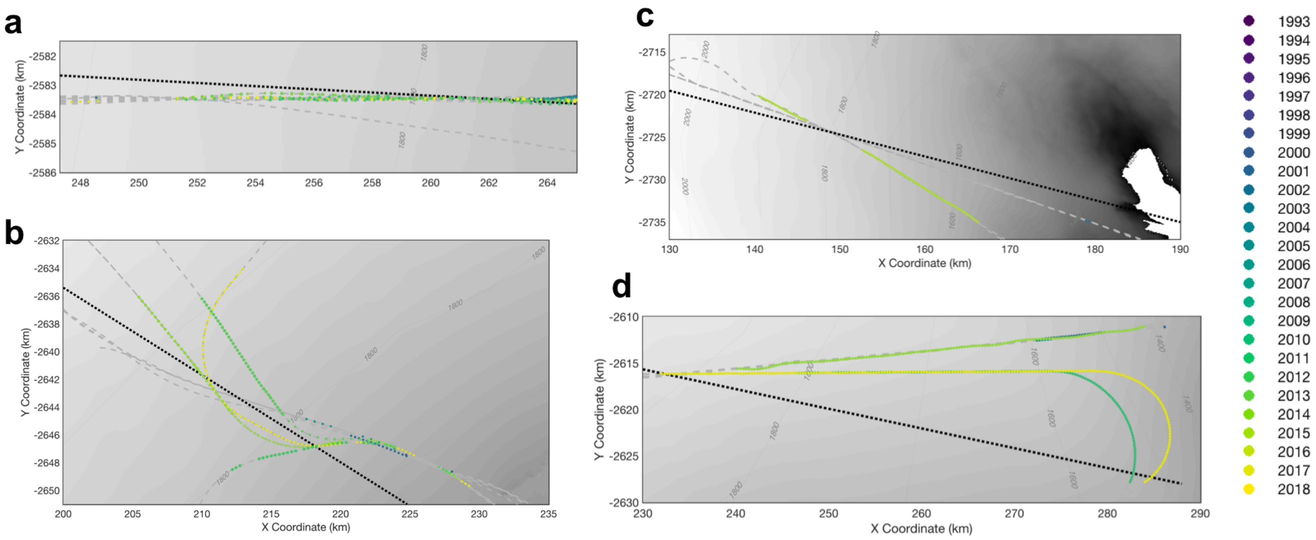

Figure B8. Repeat flight lines and aquifer detections for a) Helheim 1, b) Ikertivaq N1, c) Køge Bugt S1, and d) Helheim 4.

B6. Change Point Calculation of a Time Series

By definition, a change point is a time instant at which a defined statistical property, usually the mean, of a time series changes abruptly. We employ a parametric global method which selects a point to divide the time series into two sections, calculates an empiricial estimate of the mean for each section, computes the deviation of the time series from the empirical estimate of the mean, finds the total residual error, and varies the location of the point for which to divide the time series until the total residual error reaches a minimum. Given a time series x_1, x_2, ..., x_n, the method finds the point k such that the residual error r is the smallest:

$$r = \sum_{i=1}^{k-1} (x_i - \mu_{k-1})^2 + \sum_{i=k}^{N} (x_i - \mu_N)^2 - (k-1)V_{k-1} - (N-k+1)V_N. \tag{1}$$

where the mean for each section is defined as:

$$\mu_{k-1} = \frac{1}{k-1} \sum_{i=1}^{k-1} x_i \text{ and } \mu_N = \frac{1}{N-k+1} \sum_{i=k}^{N} x_i. \tag{2}$$

and the variance for each section is defined as:

$$V_{k-1} = \frac{1}{N-1} \sum_{i=1}^{k-1} x_i |A_i - \mu_{k-1}|^2 \text{ and } V_N = \frac{1}{N-1} \sum_{i=k}^{N} |A_i - \mu_N|^2. \tag{3}$$

B7. Additional Analysis of MAR Climate Reanalysis at Aquifer Sites

From the MAR Modèle Atmosphérique Régional MAR 3.5.2 (Fettweis and others, 2017) reanalysis, we analyze long-term trends in the climate variables noted in the main text. We take the average of these climate parameters for the closest MAR cells to the upstream edge of the aquifer sites because MAR's resolution is relatively coarse (20 km) for application to a single aquifer.

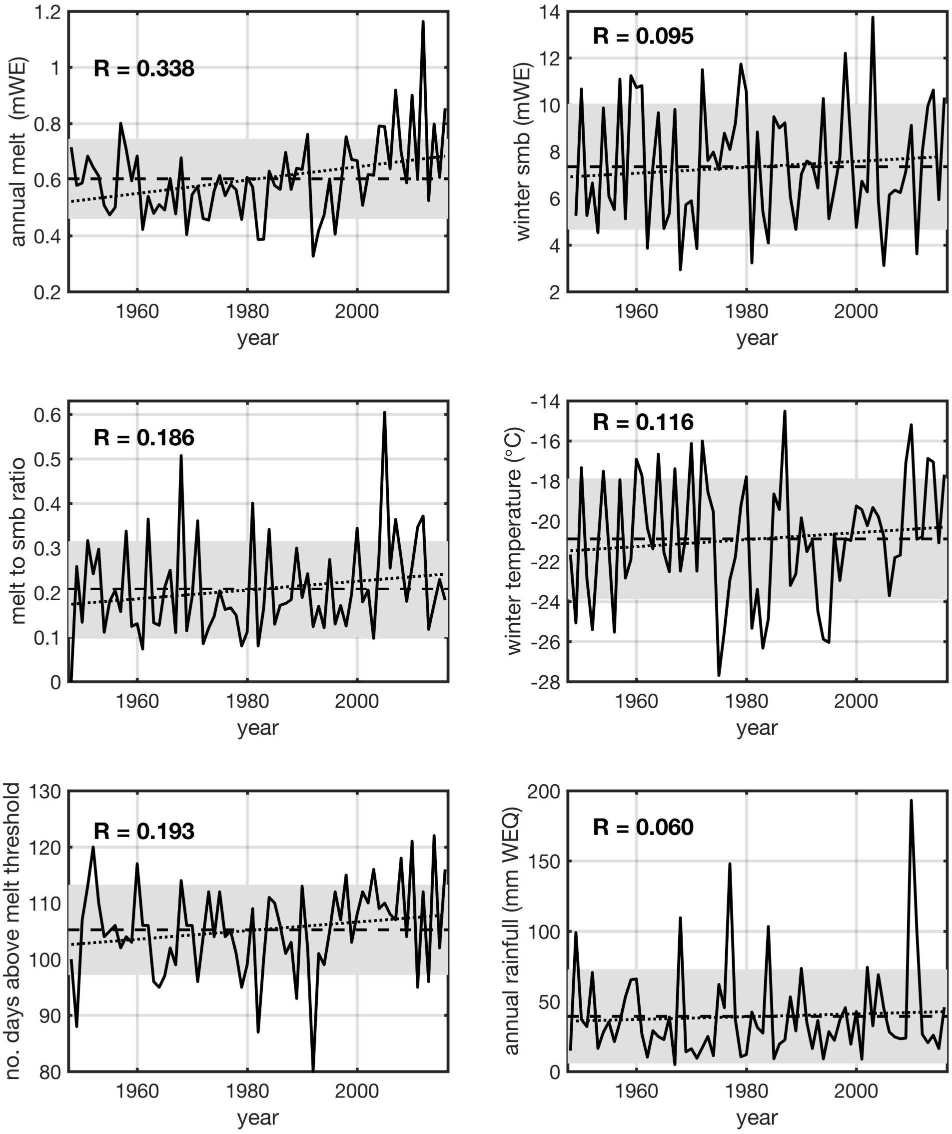

Figure B9. MAR output at the aquifer sites. (a) annual melt, (b) winter surface-mass-balance, (c) melt-to-surface-mass-balance ratio, (d) winter temperature, (e) number of days above the melt threshold, and (f) annual rainfall.

References

Brangers, I., Lievens, H., Miège, C., Demuzere, M., Brucker, L., & De Lannoy, G. (2020). Sentinel-1 detects firn aquifers in the greenland ice sheet. *Geophysical Research Letters*, *47*(3), e2019GL085192.

Bromwich, D. H., Nicolas, J. P., Hines, K. M., Kay, J. E., Key, E. L., Lazzara, M. A., ... others (2012). Tropospheric clouds in antarctica. *Reviews of Geophysics*, *50*(1).

Christianson, K., Kohler, J., Alley, R. B., Nuth, C., & Van Pelt, W. J. (2015). Dynamic perennial firn aquifer on an arctic glacier. *Geophysical Research Letters*, *42*(5), 1418–1426.

Chu, W., Schroeder, D. M., & Siegfried, M. (2018). Retrieval of englacial firn aquifer thickness from ice-penetrating radar sounding in southeastern greenland. *Geophysical Research Letters*, *45*(21), 11–770.

Culberg, R., Schroeder, D. M., & Chu, W. (2021). Extreme melt season ice layers reduce firn permeability across greenland. *Nature communications*, *12*(1), 1–9.

Fettweis, X., & Rennermalm, A. (2020). Model simulations from modèle atmosphérique regionale (mar) over greenland, 1948-2016. *Nature Geoscience*.

Field, V, B., T, S., & Q, D. (2012). Managing the risks of extreme events and disasters to advance climate change adaptation: Special report of the intergovernmental panel on climate change.

Forster, R. R., Box, J. E., Van Den Broeke, M. R., Miège, C., Burgess, E. W., Van Angelen, J. H., ... others (2014). Extensive liquid meltwater storage in firn within the greenland ice sheet. *Nature Geoscience*, *7*(2), 95–98.

Fountain, A. G. (1989). The storage of water in, and hydraulic characteristics of, the firn of south cascade glacier, washington state, usa. *Annals of Glaciology*, *13*, 69–75.

Fountain, A. G., & Walder, J. S. (1998). Water flow through temperate glaciers. *Reviews of Geophysics*, *36*(3), 299–328.

Gascon, G., Sharp, M., Burgess, D., Bezeau, P., & Bush, A. B. (2013). Changes in accumulation-area firn stratigraphy and meltwater flow during a period of climate warming: Devon ice cap, nunavut, canada. *Journal of Geophysical Research: Earth Surface*, *118*(4), 2380–2391.

Humphrey, N. F., Harper, J. T., & Meierbachtol, T. W. (2021). Physical limits to meltwater penetration in firn. *Journal of Glaciology*, *67*(265), 952–960.

Jansson, P., Hock, R., & Schneider, T. (2003). The concept of glacier storage: a review. *Journal of Hydrology*, *282*(1-4), 116–129.

Killick, R., Fearnhead, P., & Eckley, I. A. (2012). Optimal detection of changepoints with a linear computational cost. *Journal of the American Statistical Association*, *107*(500), 1590–1598.

Koenig, L. S., Miège, C., Forster, R. R., & Brucker, L. (2014). Initial in situ measurements of perennial meltwater storage in the greenland firn aquifer. *Geophysical Research Letters*, *41*(1), 81–85.

Lavielle, M. (2005). Using penalized contrasts for the change-point problem. *Signal processing*, *85*(8), 1501–1510.

Legchenko, A., Miège, C., Koenig, L. S., Forster, R. R., Miller, O., Solomon, D. K., ... Brucker, L. (2018). Estimating water volume stored in the south-eastern greenland firn aquifer using magnetic-resonance soundings. *Journal of Applied Geophysics*, *150*, 11–20.

Leuschen, C., Hale, R., Keshmiri, S., Yan, J., Rodriguez-Morales, F., Mahmood, A., & Gogineni, S. (2014). Uas-based radar sounding of the polar ice sheets. *IEEE Geoscience and Remote Sensing Magazine*, *2*(1), 8–17.

Lilien, D. A., Hills, B. H., Driscol, J., Jacobel, R., & Christianson, K. (2020). Impdar: an open-source impulse radar processor. *Annals of Glaciology*, *61*(81), 114–123.

Machguth, H., MacFerrin, M., van As, D., Box, J. E., Charalampidis, C., Colgan, W., … van de Wal, R. S. (2016). Greenland meltwater storage in firn limited by near-surface ice formation. *Nature Climate Change*, *6*(4), 390–393.

Miège, C., Forster, R. R., Brucker, L., Koenig, L. S., Solomon, D. K., Paden, J. D., … others (2016). Spatial extent and temporal variability of greenland firn aquifers detected by ground and airborne radars. *Journal of Geophysical Research: Earth Surface*, *121*(12), 2381–2398.

Miller, O., Solomon, D. K., Miège, C., Koenig, L., Forster, R., Schmerr, N., … others (2020). Hydrology of a perennial firn aquifer in southeast greenland: an overview driven by field data. *Water Resources Research*, *56*(8), e2019WR026348.

Montgomery, L., Miège, C., Miller, J., Scambos, T. A., Wallin, B., Miller, O., … Koenig, L. (2020). Hydrologic properties of a highly permeable firn aquifer in the wilkins ice shelf, antarctica. *Geophysical Research Letters*, *47*(22), e2020GL089552.

Mouginot, J., Rignot, E., Bjørk, A. A., Van den Broeke, M., Millan, R., Morlighem, M., … Wood, M. (2019). Forty-six years of greenland ice sheet mass balance from 1972 to 2018. *Proceedings of the national academy of sciences*, *116*(19), 9239–9244.

Munneke, P. K., Ligtenberg, S. R., Suder, E. A., & Van den Broeke, M. R. (2015). A model study of the response of dry and wet firn to climate change. *Annals of Glaciology*, *56*(70), 1–8.

Munneke, P. K., M. Ligtenberg, S., Van den Broeke, M., Van Angelen, J., & Forster, R. (2014). Explaining the presence of perennial liquid water bodies in the firn of the greenland ice sheet. *Geophysical Research Letters*, *41*(2), 476–483.

Nghiem, S., Hall, D., Mote, T., Tedesco, M., Albert, M., Keegan, K., … Neumann, G. (2012). The extreme melt across the greenland ice sheet in 2012. *Geophysical Research Letters*, *39*(20).

Ochwat, N. E., Marshall, S. J., Moorman, B. J., Criscitiello, A. S., & Copland, L. (2021). Evolution of the firn pack of kaskawulsh glacier, yukon: meltwater effects, densification, and the development of a perennial firn aquifer. *The Cryosphere*, *15*(4).

Oerter, H., & Rauert, W. (1982). Core drilling on vernagtferner (oetztal alps, austria) in 1979: tritium contents. *Zeitschrift für Gletscherkunde und Glazialgeologie*, *1*, 13–22.

Poinar, K., Dow, C. F., & Andrews, L. C. (2019). Long-term support of an active subglacial hydrologic system in southeast greenland by firn aquifers. *Geophysical Research Letters*, *46*(9), 4772–4781.

Poinar, K., Joughin, I., Lilien, D., Brucker, L., Kehrl, L., & Nowicki, S. (2017). Drainage of southeast greenland firn aquifer water through crevasses to the bed. *Frontiers in Earth Science*, *5*, 5.

Rodriguez-Morales, F., Gogineni, S., Leuschen, C. J., Paden, J. D., Li, J., Lewis, C. C., … others (2013). Advanced multifrequency radar instrumentation for polar research. *IEEE Transactions on Geoscience and Remote Sensing*, *52*(5), 2824–2842.

Samimi, S., Marshall, S. J., Vandecrux, B., & MacFerrin, M. (2021). Time-domain reflectometry measurements and modeling of firn meltwater infiltration at dye-2, greenland. *Journal of Geophysical Research: Earth Surface*, *126*(10), e2021JF006295.

Schneider, T. (1999). Water movement in the firn of storglaciären, sweden. *Journal of Glaciology*, *45*(150), 286–294.

Shepherd, A., Ivins, E., Rignot, E., Smith, B., Van Den Broeke, M., Velicogna, I., … others

(2020). Mass balance of the greenland ice sheet from 1992 to 2018. *Nature*, *579*(7798), 233–239.

Thomas, E. R., Marshall, G. J., & McConnell, J. R. (2008). A doubling in snow accumulation in the western antarctic peninsula since 1850. *Geophysical research letters*, *35*(1).

Vandecrux, B., Mottram, R., Langen, P. L., Fausto, R. S., Olesen, M., Stevens, C. M., … others (2020). The firn meltwater retention model intercomparison project (retmip): evaluation of nine firn models at four weather station sites on the greenland ice sheet. *The Cryosphere*, *14*(11), 3785–3810.

Van den Broeke, M. R., Enderlin, E. M., Howat, I. M., Kuipers Munneke, P., Noël, B. P., Van De Berg, W. J., … Wouters, B. (2016). On the recent contribution of the greenland ice sheet to sea level change. *The Cryosphere*, *10*(5), 1933–1946.

Van Wessem, J., Ligtenberg, S., Reijmer, C., Van De Berg, W., Van Den Broeke, M., Barrand, N., … others (2016). The modelled surface mass balance of the antarctic peninsula at 5.5 km horizontal resolution. *The Cryosphere*, *10*(1), 271–285.

van Wessem, J. M., Steger, C. R., Wever, N., & van den Broeke, M. R. (2021). An exploratory modelling study of perennial firn aquifers in the antarctic peninsula for the period 1979–2016. *The Cryosphere*, *15*(2), 695–714.

APPENDIX C. SUPPORTING INFORMATION FOR CHAPTER 4

Contents of this file

Text C1
Figures C1 to C6

Introduction

This supporting information provides additional details on the snow-accumulation rates derived from the ground-penetrating radar and on the climate products used to determine the storms and wind directions in the main manuscript. Text C1 provide a summary of the climate products used for this study. Figures C1and C2 show additional climate analysis, Figures C3 and C4 show snow-accumulation results for time periods T2 and T3, and Figures C5 and C6 show firn depth-density profiles and influence of varying depth-density calculations on calculations of internal layer depth.

Text C1. Climate Analysis

We choose ERA5 land daily reanalysis product for 1950-2023 (Muñoz-Sabater, 2019a), ERA5 land monthly reanalysis product for 1950-2023 (Muñoz-Sabater, 2019b), and CMIP6 GFDL-ESM4 historical product for 1850-2014 (Zhang et al., 2019) to calculate snow accumulation and wind speed, direction, and magnitude over Hercules Dome. We also compare our results to AMPS daily precipitation dataset. Below, we describe each product briefly and include some figures illustrating results referred to in the main text.

ERA5 is the fifth-generation European Centre for Medium-Range Weather Forecasts (ECMWF) reanalysis used for global climate and weather from 1940 onwards available at daily intervals. ERA5 provides hourly output for a variety of quantities related to atmospheric, ocean-wave, and land-surface variables; an uncertainty estimate at three-hour intervals through an underlying ten-member ensemble; and pre-calculated monthly-mean averages to facilitate a variety of climate applications. ERA5 is updated daily and has a latency of five days. The ERA5 land daily and monthly reanalysis products used in this study are regridded subsets of the full ERA5 dataset to a regular latitude-longitude grid at a resolution of 0.25° x 0.25°, with uncertainty estimates at 0.5° x 0.5°. We choose ERA5 because it is one of the most widely used climate products by the cryosphere community and has a relatively fine resolution over Hercules Dome.

CMIP6 is a collection of daily and monthly global climate projection and historical data from a large number of experiments, models, and time periods within the framework of the sixth phase of Coupled Model Intercomparison Project (CMIP) and is used for the IPCC 6th Assessment Report. CMIP was established by the World Climate Research Program in 1995 with the intent to provide a database of coupled global circulation model simulations; and it involves institutions from around the world running their models with specified input forcings that produce a standardized output. CMIP6 consists of 134 models from 53 modeling centers, and involves several novel aspects from its predecessor CMIP5, including several common experiments and historical simulations; common standards, infrastructure, and documentation that facilitates the distribution of output across different CMIP phases; and an ensemble of CMIP-endorsed Model

Intercomparison Projects to address many specific questions that were not addressed in previous CMIP phases. In this study, we choose the CMIP6 GFDL-ESM4 historical product from the U.S. NOAA Geophysical Fluid Dynamics Laboratory. The GFDL-ESM4 Model consists of AM4.0 atmosphere at approximately 1° resolution and 49 levels of interactive chemistry and aerosols; OM4 MOM6-based ocean at 0.5° resolution with 75 levels using hybrid pressure and isopycnal vertical coordinates; SIS2 sea ice with radiative transfer; LM4.1 land model; COBALTv2 ocean biogeochemical component; and fully interactive dust and iron cycling between land, atmosphere, and ocean.

The AMPS daily precipitation dataset was created by concatenating daily values for each day in the series. For the domain used here (d03), AMPS archives model variables hourly for 39 hours with forecast runs starting for each day at 00z and 12z. By default, AMPS archives precipitation as an accumulating value from the start of the forecasting run. Post-processing for the AMPS archive converts this data to the amount accumulated between archived files, i.e., hourly accumulated precipitation. This was our starting point. Standard practice when working with WRF is to allow 24 hours for model spinup before using any model variables. In theory, a daily value is then the sum of precipitation between forecast hours 25 and 48. In practice, because 48 hours of d03 data are not available in one forecast run, the daily value comes from both the 00z and 12z runs. Daily values were then summed to produce spatially resolved annual values. The average precipitation presented here is the average of these values for calendar years 2018-2022.

While the AMPS archive is indisputably valuable, there are shortcomings to the current WRF implementation. One specific to Hercules Dome is that the underlying topographic dataset (from RAMP2) does not reflect the actual topography as seen in the newer REMA DEM. Thus while AMPS domains begin to approach a spatial resolution relevant to the scale of meteorological processes in the region, the surface elevation remains in error. More generally, WRF, as configured for AMPS, shows a distinct cold bias in near-surface temperature as seen, for example, when compared to the Wisconsin AWS Theresa (84.6 °S, 115.85 °W, 184 km from West Dome) as well as at other West Antarctic sites (Hines et al 2019).

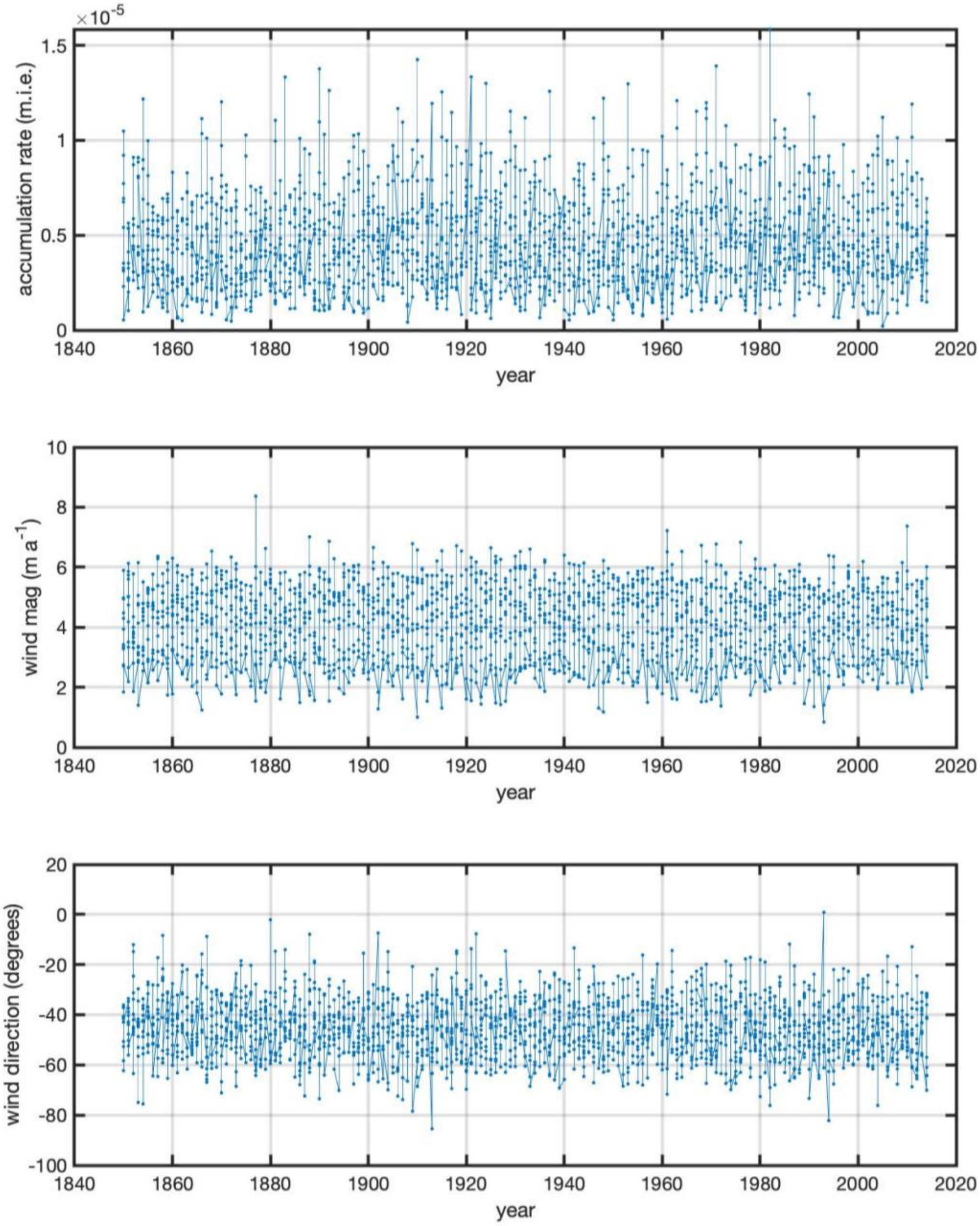

Figure C1. CMIP6 values averaged over monthly intervals between 1850-2014 for Hercules Dome.

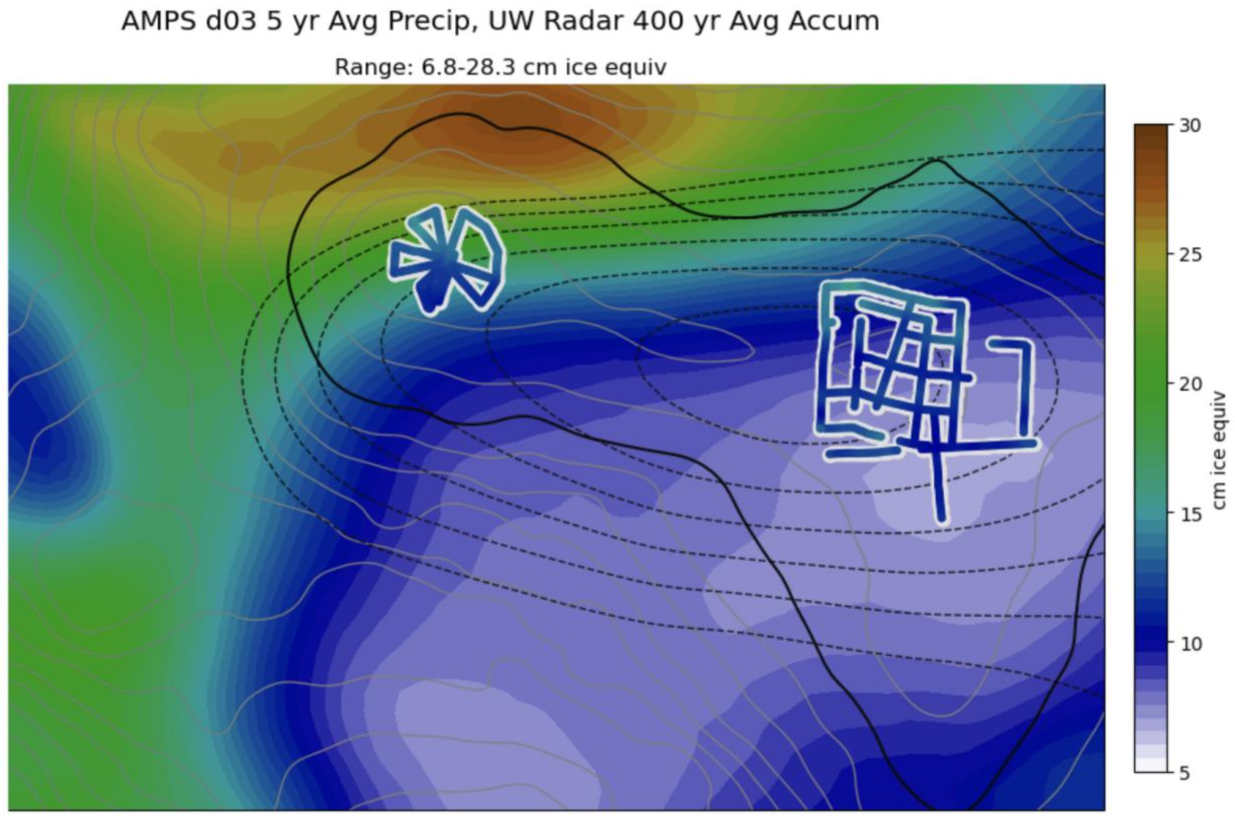

Figure C2. Interpolated AMPS output over Hercules Dome. Resolution is 2.76 km. Solid contours represent surface topography from REMA (bolded represents the 2550-m contour). Dashed contours represent the topography used in AMPS. Radar-derived snow-accumulation rates are shown from this study in the pale highlighted transects.

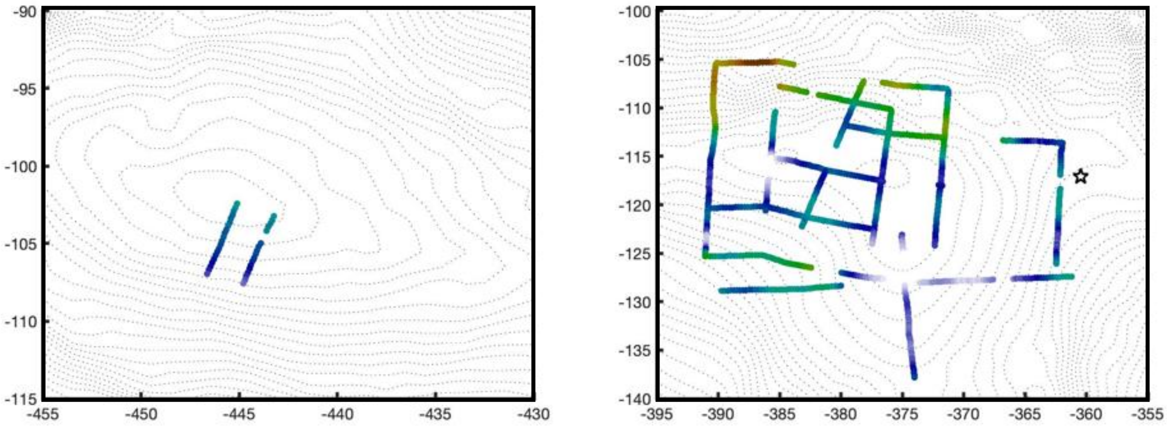

Figure C3. The 326-year time-averaged snow-accumulation rates across Hercules Dome.

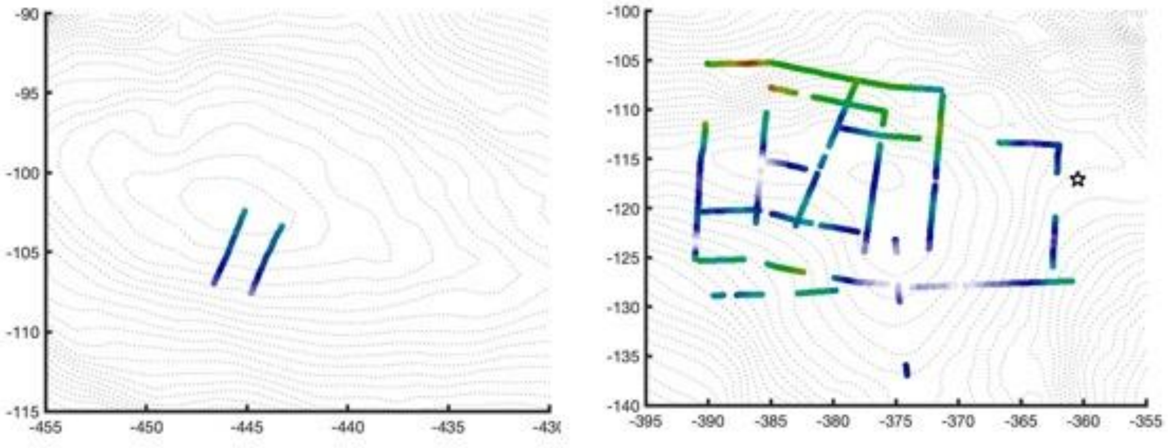

Figure C4. The 225-year time-averaged snow-accumulation rates across Hercules Dome.

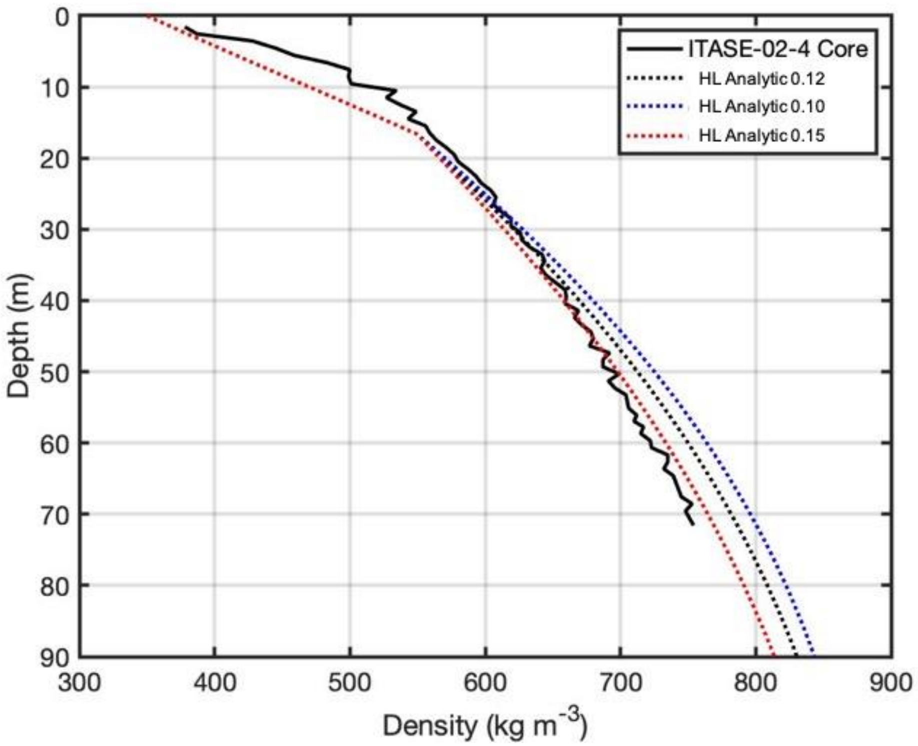

Figure C5. Firn depth-density profiles from Herron and Langway (1980) used in calculating the time-averaged snow-accumulation rates, compared to the ITASE-02-4 firn core depth-density profile.

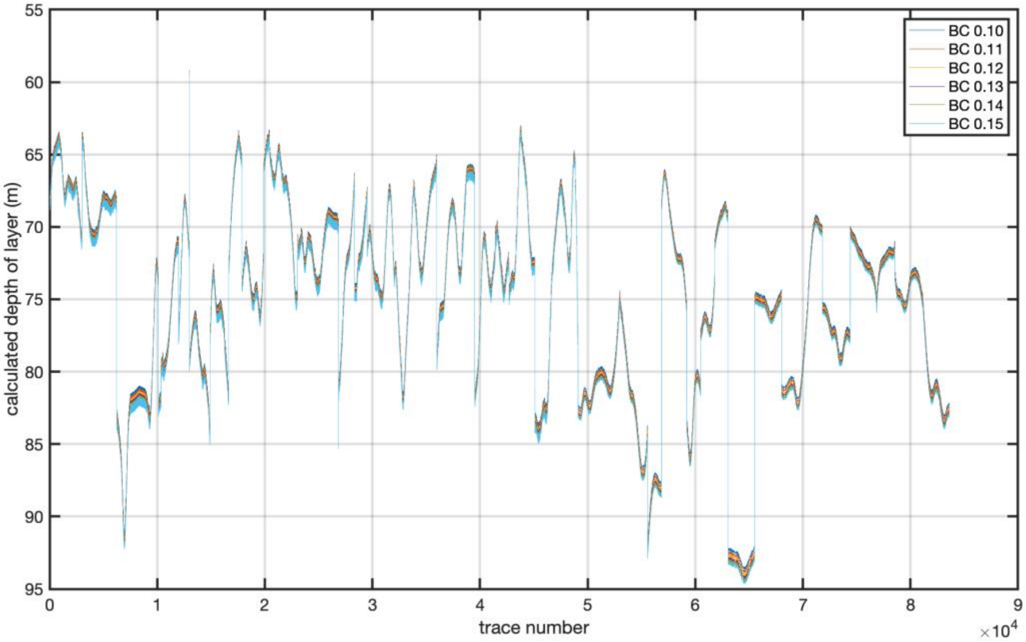

Figure C6. Calculated layer depths for the T1 time period for different surface accumulation boundary conditions to the firn model.

References

Hines, K.M., Bromwich, D.H., Wang, S.H., Silber, I., Verlinde, J. and Lubin, D., 2019. Microphysics of summer clouds in central West Antarctica simulated by the Polar Weather Research and Forecasting model (WRF) and the Antarctic Mesoscale Prediction System (AMPS). *Atmospheric Chemistry and Physics*, *19*(19), pp.12431-12454.

Herron, Michael M and Chester C Langway (1980). “Firn densification: an empirical model”. Journal of Glaciology 25.93, pp. 373–385

Muñoz-Sabater (2019a). “ERA5-Land hourly data from 1950 to present.” Copernicus Climate Change Service (C3S) 13.9, pp. 4349–4383.

Muñoz-Sabater (2019b). “ERA5-Land monthly averaged data from 1950 to present”. Copernicus Climate Change Service (C3S) 13.9, pp. 4349–4383.

Zhan, L.X., Xiao-Long, C.H.E.N. and Xiao-Ge, X.I.N. (2019). Short commentary on CMIP6 scenario model intercomparison project (ScenarioMIP). Advances in Climate Change Research, 15(5), p.519.